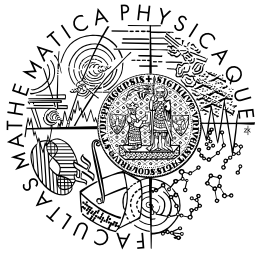

FACULTY
OF MATHEMATICS
AND PHYSICS
Charles University

MASTER THESIS

Lucia Bajtošová

Properties of thin films studied by in-situ TEM

Department of Physics of Materials

Supervisor of the master thesis: doc. RNDr. Miroslav Cieslar, CSc.

Study programme: Physics

Study branch: Physics of Condensed Matter and Materials

Prague 2021

I declare that I carried out this master thesis independently, and only with the cited sources, literature and other professional sources. It has not been used to obtain another or the same degree.

I understand that my work relates to the rights and obligations under the Act No. 121/2000 Sb., the Copyright Act, as amended, in particular the fact that the Charles University has the right to conclude a license agreement on the use of this work as a school work pursuant to Section 60 subsection 1 of the Copyright Act.

In Prague date 22.7.2021 Lucia Bajtošová

Author's signature

I would like to express my immense gratitude to all the people who offered their help with the creation of this thesis: my supervisor doc. RNDr. Miroslav Cieslar, CSc for constant stream of assistance and guidance, Mgr. Jan Fikar, Ph.D. for guidance with construction and corrections of MD code, RNDr. Petr Harcuba, Ph.D. for endless help with FIB cutting of the samples, Mgr. Jozef Veselý, Ph.D. for advice on TEM operation, Mgr. Jan Hanuš, Ph.D. for help with sputtering of the material, Mrs. Marta Čepová and Ing. Jana Kálalová for their help with a preparation of free standing samples, and Mgr. Barbora Křivská for introduction to result analysis programmes and help with LaTex difficulties.

Title: Properties of thin films studied by in-situ TEM

Author: Lucia Bajtošová

Department: Department of Physics of Materials

Supervisor: doc. RNDr. Miroslav Cieslar, CSc., Department of Physics of Materials

Abstract: Mechanical properties of widely applicable thin nanocrystalline films have been a subject of interest for some time due to deviation of their properties from the properties of bulk and micro sized grain materials. The deformation mechanisms in these materials are altered by restricted size of the material and high ratio of surface and grain boundary areas. Recent advances in transmission electron microscopy (TEM) allow direct observations of the deformation mechanisms during nanoindentation or tensile deformation of the specimen. Thin Al films prepared by DC magnetron sputtering were deformed in situ in TEM and bright field TEM. High resolution TEM and automated crystallographic orientation mapping (ASTAR) were implemented to observe the ongoing deformation mechanisms. Molecular dynamic simulation designed to approach the conditions of performed experiment were used to visualize the deformation mechanisms on atomic scale and the reliability of both methods was discussed.

Keywords: thin films, molecular dynamics, in situ TEM

Contents

Introduction

Thin metallic films have been and expansively continue to be crucial components in a variety of microelectronic and micro-electro-mechanical systems (MEMS). Since thin films in these devices (especially in MEMS) are often subjected to a mechanical exertion under diverse operating velocities and frequencies, an interest in prediction of thin film properties have been sparked. A wide range of experiments have been devised to measure the thin film characteristics such as thermal cycling [1] or nanoindentation techniques [2], as well as experiments focused on studies of the films separated from the substrate [3], presence of which can influence the measured properties.

The size dependency does not confine only to volume restrictions, aside from sample size, intrinsic size effects related to internal material structure e.g. grain size in polycrystalline materials also exist and have been thoroughly studied in bulk materials. A well-known Hall-Petch relation [4, 5] can be used to describe the dependence of mechanical strength on average grain size in polycrystals. However, since this model is based on assumptions of a formation of dislocation pileups in the vicinity of grain boundaries, the assumptions of this model are not met in the case of grains with sizes approaching the size of dislocations. On the contrary a decrease of the yield stress and hardness with the decrease of grain size have been reported by numerous experimental studies [6, 7] for sufficiently small grains. A possibility of obtaining more detailed information on materials microstructure development during straining was introduced with advances in in situ transmission electron microscopy techniques. A direct observation of the material during indentation with indenters of various shapes enabled to directly visualize deformation mechanisms such as emission of dislocations or grain boundary sliding [8, 9]. Furthermore, an implementation of MEMS device allowed a successful performance of tensile in situ TEM experiments [10] with a benefit of easier derivation of material properties from measured force-displacement functions.

The power of computers constantly growing over the past decades conditioned the use of computer simulations as a way of predicting the behaviour of various studied issues. More advanced methods and code interfaces were developed so that computational methods are now comparable to theoretical and experimental ones. Several approaches may be taken when simulating a specific process of interest. To model the interactions between atoms, empirical representations or ab initio quantum mechanical methods are most commonly used [11]. Both these approaches can be then used in tools employing models in individual applications such as lattice energy modelling, calculations of lattice dynamics, the molecular dynamics simulations method or the Monte Carlo simulation method.

Molecular dynamics (MD) is a simulation method based on a simple concept of using Newton's equation of motion to predict the time evolution of individual atoms [12]. In a given configuration of atoms, a force on each atom is computed by either empirical or quantum mechanical methods and is converted to acceleration. A numerical time step is used to predict the position of the atoms after the time step from the information on the current and previous atomic positions, velocities and accelerations. One of the benefits of this approach applied on a mechanical straining of thin films is the possibility to observe deformation mech-

anisms in atomistic details. Studies of size effects of different crystal structures [13], as well as orientations [14] and the role of grain boundary migration and grain rotation [15, 16] have been conducted using MD. However, certain constrains sprouting from the construction of MD algorithm are present, restricting the simulations of deformation to sufficiently small dimensions and deformation rates higher than the ones used in experiments.
In this work an in situ TEM deformation of polycrystalline thin FCC films have been carried out in order to determine the effect of small grains and restricted volumes on material properties and deformation mechanisms. The experimental results were then used to construct a molecular dynamics simulation conditions resembling the ones used in the experiment and effects of changes of individual simulation parameters were examined with consideration of detected experimental outcomes.

1. Review of thin metallic films studies: experimental

1.1 Metallic thin films

Generally, there are two definitions where a metallic film is considered thin. In the case of films deposited on substrates, the decisive factor is the ratio of the film and substrate thickness. Thin usually means that the film is significantly thinner than the substrate to which it is bound [17]. The second way to regard a film as thin is when its dimension approaches microstructural film dimensions such as grain size and dislocation spacing.
The interest in mechanical properties of thin films was caused by expanding application of thin-film structures in microelectronic, magnetic, thermal and optical devices. Despite of essentially functional, non-structural, applications of these devices, significant stresses can be established during the fabrication and the operation of the films. For instance, the interconnections in field effect transistors [18], an essential part of a microprocessor, are usually made from pure metals with high electrical conductivity and the strains imposed in them are controlled by thermal expansion differences. The evolution of stresses in these interconnections (often distributed inhomogeneously) is usually controlled by plasticity. Therefore any thermal cycling can lead to the concentration of stresses and strains and localized failure. Therefore, to ensure the reliability of functional materials, knowledge of the mechanical properties of thin films is required. In addition, thin films are now widely used in micro- and nano-electro-mechanical-systems (MEMS and NEMS) wherein thin film structures are created to produce devices such as thermal sensors, accelerometers and actuators. Here the mechanical properties are of primary importance.

1.2 Testing methods

Dimensional constraints and the microstructure developed during the thin film growth are causes for a difference of their behavior when compared to materials in bulk forms [19]. Various techniques have been developed to study mechanical properties in small dimensions. Most common approaches for the characterization of thin films on substrates include thermal cycling [1], bulge testing [20], microtensile testing [21] or nanoindentation [2] techniques.
The thermal cycling method is based on different thermal expansion coefficients of the film and the substrate. The film/substrate composite is subjected to a thermal cycle and the stress is monitored by measuring the substrate curvature or by X-rays. However, the details of measured curves are difficult to interpret because the strain and temperature cannot be varied independently in these experiments. A study of strengthening mechanisms of thin Cu films by this method [1] showed a linear increase of tensile stresses at room temperature with reciprocal film thickness and the general discrepancy of mechanical properties of a thin film and bulk material of the same composition was reconfirmed.

In bulge testing [20], a freestanding film membrane is clamped to a circular ring and pressurized from one side, thus deforming the film by bulging (fig. 1.1a). The modulus, yield, fracture strength and residual stress of the film can be determined from measuring the applied pressure along with the height of the bulge. Sub-micron aluminum films studied by bulge testing [20] yielded values of Young's modulus in agreement with published data for bulk aluminum. The ductility of thin films is substantially lower, and the stress level is higher in the films than in the bulk material.

Tensile testing, a popular method used in macroscopic samples where a dog-bone shaped specimen is loaded in tension (fig. 1.1b), has not been commonly used for thin film testing due to problems with the specimen shaping, manipulation, gripping and measurements. Despite of disadvantages, a possibility of direct extraction of material properties from the measured data with no calibration model necessary along with the applicability to both free-standing films and films on substrate provide enough benefits to realize tensile experiments [22].

Few methods of tensile testing of films on substrates have been used. One of the first approaches was developed by Ruud et al. [23]. Free standing 5 µm thick films were sandwiched between aluminum grippers and elongated by a computer controlled motor driven micrometer attached to one side. The force was measured by load cell in series while for the displacement measurements laser diffraction spots from a grating applied on the film surface by photo-lithography were used. Cu, Ag and Ni thin films with a strong {111} texture were tested with measured Young moduli 120 GPa (Cu), 84 GPa (Ag) and 201 GPa (Ni). A similar technique where a dog-bone shaped specimen of film supported by a silicon frame was made and the frame was cut before testing was used on multilayer Al-Ti-Al 2 µm thick film [21]. Yield strength between 90 and 120 MPa and ultimate strength between 145 and 200 MPa were measured while no acceptable values of Young modulus were produced. Moreover, free standing gold films were tested by Emery and Povirk [24] with measured elastic modulus 88±11 GPa during loading and 84±9 GPa in unloading. Values of yield strength ranged between 90 and 340 MPa depending on the film thickness. Several films were tested at strain rates that varied over two orders of magnitude ($5 \cdot 10^{-4}$ s^{-1} to $5 \cdot 10^{-6}$ s^{-1}), however no significant effect of strain rates on mechanical properties was observed.

Another method dealing with inconveniences linked to a manipulation of free standing thin films was the use of substrates that can be either elastically or plastically deformed [25]. In the second case, the force displacement curves of specimen without the film should be measured to separate the portion of the force required for the deformation of the film. Aluminum films from 60 to 480 nm thick were tested and the tensile strength increased from 196 to 408 MPa. Effect of grain size on tensile strength obeyed the Hall-Petch relation.

A useful technique for studying deformation of thin films on substrates is nanoindentation where a sharp diamond indenter is forced into the surface of a film (fig. 1.2) while load – displacement curve is being measured. The deformation response on loading is both plastic and elastic while on unloading primarily elastic deformation occurs. However, the strength of substrate bounded films is significantly influenced by the film/substrate interface and it is difficult to derive the properties of the free-standing film from the above mentioned technique. For example, the flow stress of an aluminum film measured by tensile tests at room

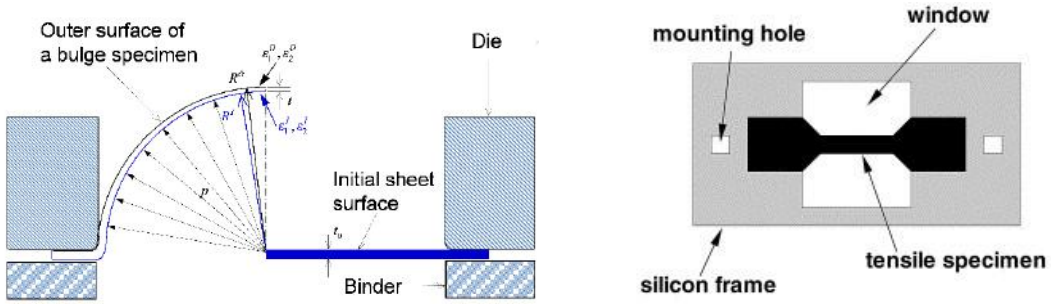

(a) (b)

Figure 1.1: (a) example of bulge test [3] (b) tension test geometry [24]

temperature gives value 102 MPa for thickness 2 µm or 126-184 MPa for thickness 1 µm with varying grain size [26]. The bulge test gives values of 10-30 MPa for the flow stress of 1 µm thick film [27], however sensitivity of the bulge test to the initial stress state of the film may lead to large systematic errors.

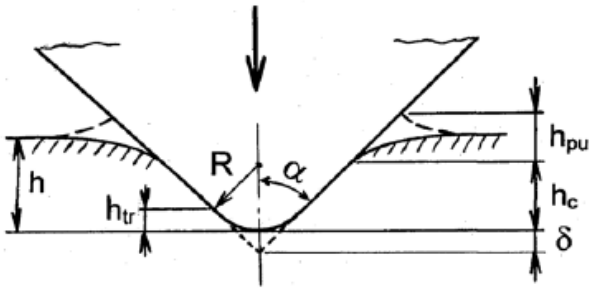

Figure 1.2: Illustration of an interaction of nanoindenter with a sample [28]

Nanoindentation technique applied on Al film on Si substrate revealed a surprisingly high value of 170 MPa in the limit of zero indentation depth [29] suggesting a local source hardening. A comparison of the flow stress of free-standing Al films to the stress of Al films on Si substrate measured by the same method [30] yielded considerably smaller values for free-standing films with strong relation to grain size and temperature. This clearly demonstrates the necessity of different experimental methods in order to measure properties of thin films without the influence of the substrate. The separation of material properties free from the substrate allows direct observation of the influence of the sample size - the size effect. Although a variety of different properties such as thermal and electrical conductivity or optical properties depend on the sample size, in the case of crystalline metals one of the main aims of material science is their strength enhancement. The size effects related to Young's modulus, material strength or diffusion processes in crystalline metals are usually a result of a combination of intrinsic and extrinsic contributions. Intrinsic size effects include microstructural properties such as grain size, the average distance of second phase particles or precipitates, and dislocations mean free path. Finally, the external sample geometrical properties such as the film thickness or pillar diameter may lead to size effects.

1.3 Microcompression testing

A successful experimental method enabling direct measurement of properties of micro-sized materials was found in microcompression testing. It is an analogy of compression experiments commonly performed on macroscopic samples where a sample in a shape of micro-sized pillars attached to the rest of the bulk material is deformed by compression with a flat-punch indenter tip with the bulk acting as a lower compression plate. The first micropillar compression experiments were conducted by Uchic et al. [31, 32] on pillars prepared by focused ion beam (FIB) (fig. 1.3) micromilling from pure Ni and $Ni_3(Al, Hf)$ monocrystal samples. The dependence of material strength on pillar size has been explored, revealing a considerable increase of strength with the decrease of the sample size. Pillars in size range from several µm down to 500 nm were used in the experiment.

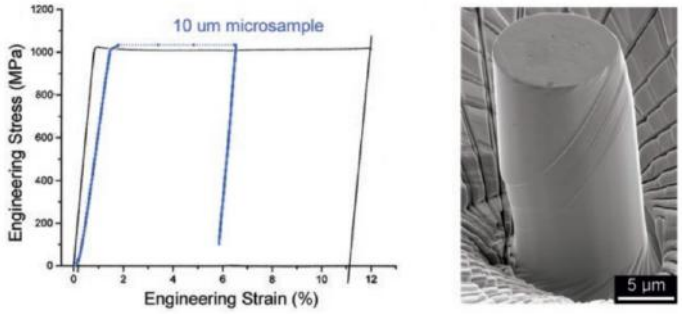

Figure 1.3: Illustration of a single crystal micropillar used in a compression experiment [32].

A detailed review of pillar compression experiment procedures, results and possible governing mechanisms has been composed by Uchic et al. [33] and two other groups of authors [34, 35]. Most of the micropillar compression studies have been focused mainly on FCC metals because of the extensive knowledge of deformation processes and structures in bulk FCC samples. The most addressed feature of studies of pure Ni [36, 37], Au [38], Al [39, 40] is the above mentioned strong dependence of yield stress on sample size for samples with diameter under tens of micrometers. This results in uncommonly high yield stresses for single crystals of diameter in submicrometer scale e.g. reaching up to 2 GPa for 200 nm wide Ni microcrystals [41]. The measured yield stress in the regime in which size dependent strengthening occurs follows power law dependency of pillar diameter D:

$$\sigma = A \cdot D^{-n}, \tag{1.1}$$

where A is a constant and n is the power law exponent. This relationship hold for diameters from hundreds of nanometers to tens of micrometers. The power law exponent for FCC metals varies, but does not exceed range 0.5 – 1.

1.4 Theoretical models of size effects

Several theoretical models attempting to interpret the size related experimental observations have been suggested, mostly regarding dislocation motion and

creation in restricted dimensions. Among them, the source truncation, source exhaustion hardening, and weakest link theory are the three underlying mechanisms mostly addressed by the researchers [42]. The source truncation refers to a transformation of double-ended dislocation sources into single-ended ones in confined volumes due to a dislocation interaction with free surfaces. The number of new dislocation sources decreases with the sample size, thus a higher strength was observed in smaller samples [43]. The source exhaustion mechanism is connected to the loss of mobile dislocations due to their escape from free surfaces or because of the lack of dislocation sources. The mobile dislocation density is then too low to sustain applied plastic flow and a larger stress should be applied. This is termed as the exhaustion hardening [44]. A special case of the source exhaustion mechanism is dislocation starvation [45] based on a fact that the dislocation must travel a certain distance before multiplication. If the sample size is smaller than this distance, the length of dislocations escaping from the free surface exceeds the length of dislocations created by their multiplication.

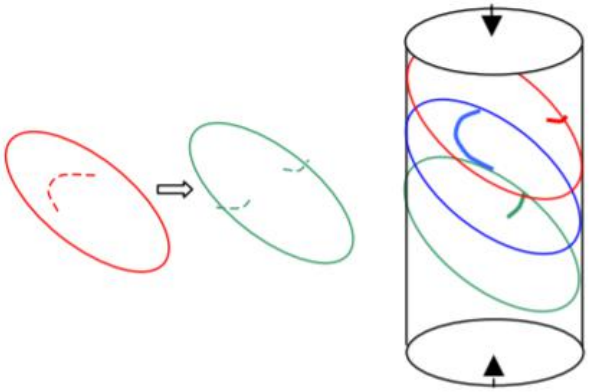

Figure 1.4: Sketch of double-pinned Frank–Read sources becoming single-ended sources in finite dimensions [43].

The weakest link theory [46] describes sample strengthening in confined volumes such as pillars. It states that there is a mean-field limit for any crystal, for which the dislocation ensemble of larger samples behave according to the conventional forest hardening mechanism. However, for samples smaller than the mean-field limit, the effective length of dislocation sources breaks down. In these small samples, the longest and the weakest dislocation sources do not exist, resulting in an enhanced contribution of the forest-hardening mechanism [42].
Along with the extrinsic size effects extensively studied by microcompression testing, microstructural properties, particularly grain size, play a significant role in dislocation nucleation and motion. Traditionally, the effect of yield stress σ_y on average grain size d is modeled by the Hall-Petch relation [4, 5]:

$$\sigma_y = \sigma_0 + k_y\sqrt{d}, \tag{1.2}$$

where σ_0 is a materials constant and k_y is the strengthening coefficient. The model is based on the interference of dislocation motion by grain boundaries. The generated dislocations move inside the grains until encountering a grain boundary,

where they form a dislocation pile up. Each dislocation in the pile up generates a repulsive stress field acting on other dislocations. As more dislocations stack at the boundary, the repulsive force applied on the grain boundary adjacent dislocation increases and reduces the energetic barrier for inter-boundary dislocation diffusion. By decreasing the grain size, less dislocations can pile up at the boundary and a higher stress is necessary to force the dislocation to overcome the boundary [47].
The Hall-Petch model provides good approximation for reasonably large grains, but it loses its justification for the nanocrystalline materials when the size of dislocations begins to approach the size of grains. This behavior is typically expected to occur for grain sizes below 10 nm [48]. Experimental observations of many systems show reduced or negative strengthening coefficient in Hall-Petch slope, commonly named as inverse Hall-Petch effect [49, 50, 51]. Regardless of the prediction, transition to inverse Hall-Petch usually occurs at grain sizes above 10 nm, where the dislocation pile ups are still possible. Several models for inverse Hall-Petch behavior have been proposed, mostly based either on dislocation motion [52, 53], diffusion [54, 55], grain boundary shearing [56, 57] or two phase material assumptions [58, 59].
Dislocation based models take dislocations as the main contribution to the plastic deformation and examine the way the small crystalline sizes affect their behavior due to for example changes in dislocations energy, changes in operation of dislocations sources or absorption of dislocations by grain boundaries.
Diffusion-based models either assume diffusion processes in strain rate regimes and temperature ranges where they do not usually occur or combine the diffusion processes with different deformation mechanisms to explain the inversion in Hall-Petch slope. Grain boundary-shearing models assume the boundaries deforming by grain-boundary shear with a regularly behaving grain interior. The models are supported by observations in several molecular dynamics simulations.
Two phase models differentiate grain boundary and grain interior as two different phases. One model assumes grain boundary to be continuous material strengthened by nanocrystalline grains, another assigns a different yield strength to the individual phases. An approach based on a statistical absorption of dislocations by grain boundaries proposed by Carlton and Ferriera [60] explains experimental observations by a non negligible dislocation activity in nanocrystalline materials despite a low dislocation density.
A decrease of grain size necessarily results in an increased volume of grain boundaries and is often connected with a change of the deformation mechanism. While in coarse-grained metals, the plastic deformation is controlled by intragranular mechanisms, nanocrystalline grains can be deformed by grain boundary (GB)-mediated mechanisms. These mechanisms might include grain boundary sliding [61] (fig. 1.5a), dislocation nucleation from the grain boundary [62], mechanical twinning, grain boundary rotations (fig. 1.5b) or even grain boundary motion. Several mechanisms can potentially be active with dominant deformation modes depending on the material and details of the composition and microstructure.

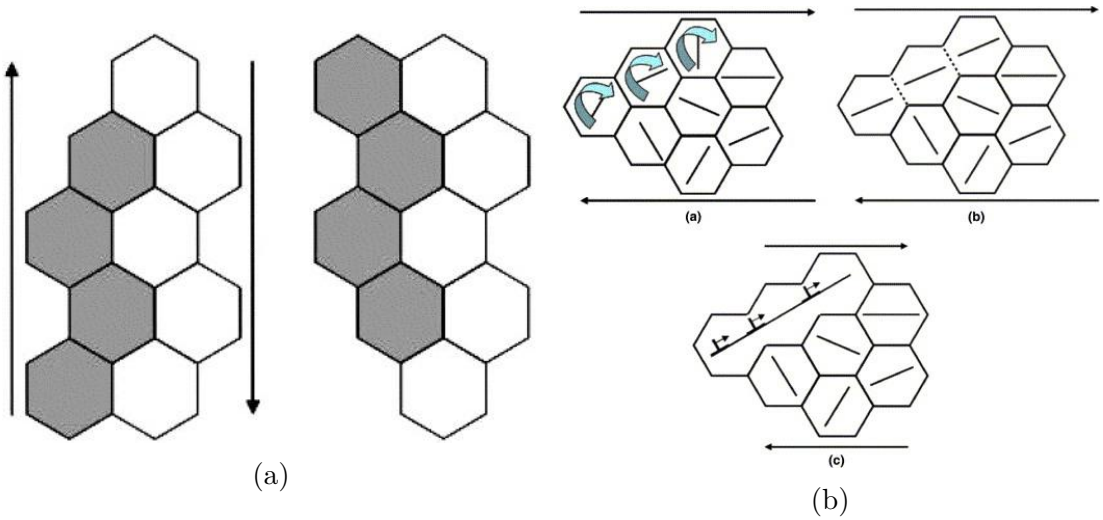

(a) (b)

Figure 1.5: (a) Grain boundary sliding model - position of grains before and after the left layer has slid upward. (b) Rotation of neighboring grains and formation of elongated grains by an annihilation of the boundary [47].

1.5 In situ TEM deformation

Advances in in situ transmission electron microscopy techniques brought a possibility of direct observations of the materials microstructure evolution by TEM during deformation by nanoindentation [63]. With this technique, a direct study of polycrystal ultrafine-grained materials became possible and the influence of grain boundaries along the reduced sample dimensions could be investigated. To do so, constraints linked to a low thickness of the sample (it should be electron transparent), its accessibility to the indenter in direction normal to the electron beam, and mechanical stability (indentation not bending the sample) should be resolved. A review by Nili et al. [64] provides an overview of in situ nanoindentation approaches and results. In situ nanoindentation measurements by Minor et al. [65] on polycrystalline Al films with the grain size significantly larger than the contact area of the indentation provided observation of dislocation nucleation, characterization of the dislocation distribution created by indentation, and the observation of indentation-induced grain boundary motion. The Al films were deposited on silicon substrates formed in the shape of a wedge, peaked with a plateau by evaporation. The indentation was made into the cap of film on the flat top of the wedge. Nucleation and increase of dislocation density with deformation was observed, however the motion of individual dislocations was too fast to be captured. It was shown that the evolution of plastic zone during indentation at shallow indentation depths into initially dislocation-free Al films depends more on the microstructure of the film than on the indentation depth. Additionally, significant grain boundary motion was observed during the indentation suggesting participation of grain boundaries in the deformation of the film.
Further study by these authors [8] was focused on values of the shear stress at the onset of plasticity. Again, a dislocation free polycrystalline Al film was indented by a Berkovich indenter while monitoring the force-displacement curves. The first dislocation nucleation accompanied by a local force build-up appeared at very small forces -1.5 µN and quickly faded with dislocations gliding and es-

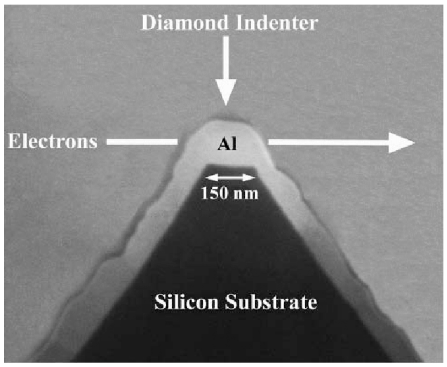

(a)

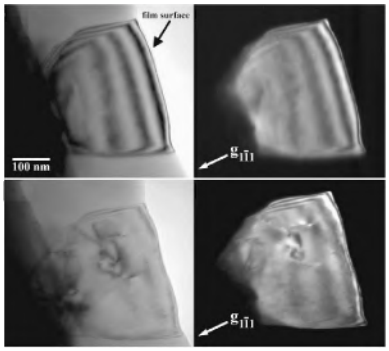

(b)

Figure 1.6: (a) Configuration of nanoindentation experiment of a thin film. (b) Images of the Al grain before and after the indentation in dark field and bright field [65].

caping through the surface. The order of corresponding shear stress -1.95 GPa matched the values from conventional nanoindentation experiments. Moreover, it was shown that a submicrometre aluminum grain with dislocation density of $\approx 10^{14}$ m^{-2} is also capable of supporting shear stresses close to the theoretical shear strength. The boundary mobility, a typical deformation mechanism in fine grained metals at elevated temperatures, was further studied by Winning et al. [66] on aluminum bicrystals by using X-ray diffraction to determine the grain position. Both low-angle and high-angle grain boundaries in pure Al were shown to move by an external shear stress at temperatures above 200 °C. Another phenomenon observed during compression tests of Al thin film during deformation at room temperature is grain growth by consumption of neighboring grains [9]. Disappearance of Al grains of sizes smaller than 150 nm and coarsening of the favorably oriented neighbors were observed as a result of the decrease of the free energy of the system. In situ nanoindentations at room temperature were performed by Jin et al. [67] on both ultrafine grained Al films with distribution of grain sizes between 100 and 500 nm and nanocrystalline films with grain size under 20 nm. Deformation-induced grain growth at the expense of surrounding smaller grains was observed when indenting the submicrometer grains. In the case of nanocrystalline films, the grains could not be observed directly but sudden contrast changes in different dark field modes suggest grain growth mechanisms, as well as grain rotation. Both grain growth and rotation occurred almost immediately upon indentation. Both materials were also indented by ex-situ nanoindentation and load-displacement curves showed multiple displacement bursts during indentations on the submicrometer-grained Al film while continuous load-displacement behavior with no discrete displacement bursts was observed when indenting the nanocrystalline films. A complementary study by Soer et al. [68] was focused on an effect of solute Mg on the grain bounary motion in Al-Mg films. Grain boundary motion in ultrafine-grained Al during nanoindentation was confirmed and it was found that solute Mg effectively pins high-angle boundaries while the mobility of low-angle boundaries remains unaffected.

Realization of tensile in situ TEM experiments have been successfully accom-

plished with the implementation of a MEMS device. Kumar et al. studied tensile properties of free standing nanocrystalline Ni films [10]. Sheets with thickness between 30 and 40 µm with average grain size 30 nm and sheets 100 µm thick with grain size around 40 nm were produced by electrodeposition, and TEM samples were prepared by twin-jet polishing technique. Authors report an emission of dislocations at grain boundaries along with an unaccommodated grain boundary sliding. Nucleation and growth of voids and a wedge crack along grain boundaries, as well as a formation of twins were observed during the deformation. Another tensile testing of free standing Ni thin film was performed by Hugo et al. [69] using a wedge-shaped straining specimen. Dislocations, identified by their abrupt and synchronous motion, were observed in larger grains (above 30 nm) while contrast changes observed in smaller grains (≈10 nm) were not identified and were assigned to either grain rotation, global tilting or dislocation nucleation. Altogether, intense dislocation activity inside grains was concluded as a prevalent deformation mechanism. On the other hand, tensile tests performed on Al thin films [70] showed limited dislocation activity inside grains. Partial dislocations bounding stacking faults were observed and dislocation activity in grain boundaries at higher stresses was reported. At about 680 MPa failure accompanied by a brittle crack occurred.

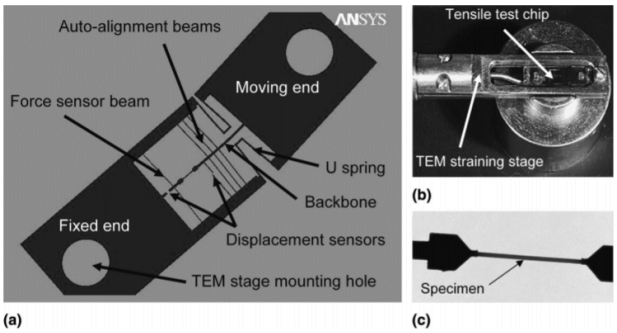

Figure 1.7: MEMS device used for in situ tensile deformations of thin films [70].

Similar results were obtained by Hattar et al. [71] when studying 200 nm thick Al films. No significant dislocation activity along with change of the contrast in several grains were observed at initial stages of the deformation. However, a dislocation activity was observed in the vicinity of the propagating crack. A study of 300 nm thick Al film with columnar grains with a mean size of 250 nm and (111) texture perpendicular to the film [72] reports dislocation glide inside grain boundaries for deformation below 2% and intragranular plasticity in larger grains along with grain boundary migration most likely triggered by GB dislocation activity for deformation above 2%. At larger deformations, the motion of intergranular dislocations led to GB sliding and eventually to cavitation. A grain boundary mobility sometimes correlated with the motion of GB dislocations was also observed during tensile deformation of an Al polycrystal with average grain size of 800 nm [73].
In situ bright field (BF) transmission electron microscopy nanomechanical tensile testing and in situ automated crystallographic orientation mapping in TEM (ACOM-TEM) were combined in work of Hosni et al. [74] in a study of ultrafine Al films with average grain size 300 nm with a strong (111) texture perpendicular

to the deformation direction. In BF TEM image, observation of bend contours was reported suggesting a change of local orientation of grains. Local distortion of the contrast of bend contours at higher strains and a quick disappearance of dislocation lines was assigned to the dislocation starvation mechanism. In-situ ACOM-TEM maps taken after deformation to strain $\epsilon \approx 0.01$ and unloading showed an average orientation change of 1.3° of the grains and no further orientation changes after deformation to higher strains. No grain growth or deformation twinning were observed. ACOM-TEM was also used to study thin Au film with (111) texture in direction perpendicular to the surface and average grain size of 37 nm [75]. An anomalous grain growth with small grains shrinking to the advantage of neighboring larger grains, local twinning and detwinning and crystal orientation changes due to grain rotation were observed with increasing strain. A significant global increase in grain size was observed at higher strains. Mompiou et al. [76] used ACOM-TEM on equiaxed grains with a strong (111) texture perpendicular to the film and mean grain size of about 250 nm. Again, grain growth and grain rotation mechanisms carried out by the nucleation and propagation of GB dislocations were observed.

2. Review of thin metallic films studies: molecular dynamics simulations

2.1 Introduction to molecular dynamics simulations

Molecular dynamics is a name for computer simulation method that predicts the time evolution of motions of individual atoms or molecules in models of solids, liquids, and gases. The calculation is based on numerical integration of Newton's equation of motion for known initial conditions of the atoms and their interatomic potentials [12]. Since its first introduction in 1950 studying the interaction of a hard sphere system [78], the method has vastly advanced and several different simulation approaches are now widely used. Examples of most common applications include study of motions of macromolecules, such as protein folding [79], or examining mechanical properties of nanotechnological devices [80].
An idealized model of the examined system is needed for any MD simulation [81]. This model is mathematically described by physical laws given initial and boundary conditions. The calculation of resulting algorithm is carried out numerically. Three sets of conditions are specified for each atom at the beginning of the simulation – its coordinates, velocity, and acceleration [77]. For crystal materials a simple choice of the coordinates is with atoms at sites of a correspondent lattice. The initial velocities depend on the temperature, their directions are randomly assigned and then adjusted to keep the center of mass stationary. Initial accelerations are usually set to zero.
Only a limited number of atoms can be used in MD in reasonably short computation time and memory. Since the simulation takes part in a container, rigid walls would distort the bulk properties of the material for standard number of atoms used in simulations [77]. By employing periodic boundary conditions, the properties of infinite bulk can be simulated with only a small number of particles. The unit computation cell is repeated in all directions so that it is surrounded by identical cells with particles which all behave identically (fig. 2.1). If a particle

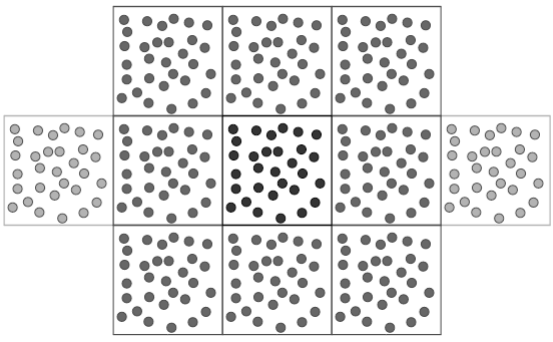

Figure 2.1: Periodic boundary conditions in 2D [77]

leaves the cell on one side, it reemerges on the opposite side of the cell keeping the total number of particles constant.
The most fundamental model for any substance uses spherical particles interacting with each other. Interactions occur, at the simplest level, between each pair of particles and can be described by interatomic potential functions. Most common model potential describing the nature of pair interactions is known as Lennard-Jones potential [81]. The potential energy can be written as

$$u(r_{ij}) = 4 \cdot \alpha[(\frac{\beta}{r_{ij}})^{12} - (\frac{\beta}{r_{ij}})^{6}], \tag{2.1}$$

where r_{ij} is a distance of two atoms and α, β parameters controlling the interaction strength and defining a length scale. It is customary to set the potential value to zero after distance r_{ij} exceeds some limit r_c. The force f corresponding to the potential u(r) is determined by its gradient

$$f = -\nabla u(r) \tag{2.2}$$

The particles obey Newtons equations of motion.

$$m_i \frac{d^2\vec{r_i}}{dt^2} = \sum_{j \neq i, j=1}^{N} f_{ij}, \tag{2.3}$$

where the sum is over all N atoms and m_i is the mass of i-th atom. By numerical integration of the equations, the particle positions as a function of time can be calculated.
However, a simple pairwise approach for modeling interatomic potential is not sufficient when describing directional covalent bonds [82]. Moreover, time executions of summations in the equation 2.3 over all N system particles scales as N^2 [81]. More advanced methods including many-body interactions and time reducing approximations need to be used.

Large-scale Atomic/Molecular Massively Parallel Simulator (LAMMPS) is a classical molecular dynamics code developed at Sandia National Laboratories [83]. It uses parallel algorithms suitable for MD models in order to optimize computation time of simulations [84]. The core of computations in MD lays in integration of Newtons equations

$$m_i \frac{d^2\vec{r_i}}{dt^2} = \sum_j F_2(\vec{r_i}, \vec{r_j}) + \sum_j \sum_k F_3(\vec{r_i}, \vec{r_j}, \vec{r_k}) + ..., \tag{2.4}$$

where m_i is the mass of i-th atom and r_i, v_i its position and velocity vectors and F_n is a force function of interatomic interactions (n=2 for pairwise, n=3 for three-body interactions, etc.) gained by equation 2.2 from terms of many body expansion of the total potential. The many body expansion is a scheme decomposing energy of system of N particles to N terms, the first term being the sum of the energies of individual particles, the second term sum of energies of all the particle pairs minus the energy of individual particles and so on. Several approximations of equation 2.4 are used to reduce the computational complexity of the problem. Firstly, only first, possibly first few, terms are kept and the force function F_2 is constructed to include also many-body and quantum effects.

Secondly, in the case of short-range interactions, only terms concerning a small region around each atom usually defined by a cutoff distance, are included in the computation. For this purpose, either a list of neighbors, which updates after every few timesteps, is kept for each atom or a binning of atoms into 3D cells with side length equal to the cutoff radius is made. The fastest MD algorithms combine both methods. Aside from the Newton equations approximations, parallelism of MD algorithms is implemented in order to reduce the computation time. The system is decomposed either to a fixed subset of atoms, fixed subset of inter-atomic forces or fixed spatial region. The benefits of the particular approaches depend on a geometry of a problem.

Force function in LAMMPS can be derived from a wide selection of interatomic potentials e.g. embedded atom method, Stillinger-Weber, Tersoff, REBO potentials [85], which encompass a variety of interactions including many-body effects. In this work, modified embedded atom method, a modification of embedded atom method, potentials are used.
Embedded atom method (EAM), an approach proposed by Daw and Baskes [86, 87], views total energy of the solid as a sum of energies of an atom when embedded into a local electron density and energies of electrostatic interactions between the atom cores. It can be written in the form:

$$E_{tot} = \sum_i E_i(\rho_{h,i}) + \frac{1}{2} \sum_{i,j_{i \neq j}} U_{i,j}(R_{i,j}), \tag{2.5}$$

where E_i is the embedding energy required to place atom i into the local electron density field, $\rho_{h,i}$ is spherically averaged atomic electron density around atom i, U_{ij} is and electrostatic two-atom interaction and R_{ij} distance between atoms i and j.
The electron density of a solid can be described as a linear superposition of atomic densities making energy a function of atom positions. A background density ρ_b of an atom is the superposition of tails from neighboring atoms:

$$\rho_{b,i}(R_i) = \sum_{j \neq i} \rho_{a,j}(R_{i,j}). \tag{2.6}$$

Where ρ_a is an electron density of an atom and R is its position. Since it is useful to define embedding energy as a function of a constant density as done in eq. 2.5, an average background density $\bar{\rho_b}$ equal to the sum of neighbor electron densities at the position of the core of the atom is used:

$$\bar{\rho_{b,i}} = \sum_{j \neq i} \rho_{a,j}(R_{i,j}). \tag{2.7}$$

R_{ij} stands for distance of atoms i and j. The summation is often reduced to a limited quantity of neighbors by a cutoff radius.
The embedding function for each element, a pair potential for each element pair and an electron density function for each element needs to be known for an alloy coherent energy computation [88]. For example, in the case of a binary alloy three pair-wise interactions, two embedding functions and two electron density contribution functions are necessary for a computation of EAM potential.

The main advantages of this approach are its simplicity compared to energy calculations from Schrodinger equation as well as its incorporation of many-atom interactions, which is not included in a simple pair interaction approximation. The inclusion of many-atom interactions originates from non-linearity of embedding energy function at higher electron densities and makes the method adequate for computations of chemically active elements. Due to its computational simplicity and inclusion of many-atom effects it is regularly used for calculations in close-packed metals and has been successfully applied to many problems such as phonons [89], liquid metals [90], alloys or grain boundary structure [91].
Modified embedded atom method (MEAM) follows the assumptions of EAM with a total energy given by eq. 2.4 while its main difference ensues in expression of local electron density [92]. Instead of a sum of atomic electron densities of surrounding atoms (eq. 2.6), the term is generalized to involve angular relation of the atom positions. Hence, the method could be applied to materials with covalent bonds [82] together with a range of different metal structures [93].
Temperature in MD can be controlled by different thermostatting algorithms. One of the most common approaches, Nose-Hoover thermostat, is in LAMMPS performed by a time integration of non-Hamiltonian equations of motion derived by Shinoda [94]. The position and velocity of atoms in the group are updated in each timestep. The time integration schemes closely follow the time-reversible measure-preserving Verlet and rRESPA integrators derived by Tuckerman et al [95].

2.2 MD of thin films: tensile and compression experiments

MD simulations of a micropillar compression enable to study deformation mechanisms of crystalline materials in full atomistic details, in particular role of free surfaces and exact deformation mechanisms. Restrictions of simulation scope is given mainly by a sample size and simulation time scale. For this reason, effects of strain rate and sample size on the simulation results have been largely investigated. Moreover, studies of the size effects of different crystal structures, orientations and other effects on deformation mechanisms have been conducted.
An effect of the size of a gold nanowire on its yield strength was investigated by Diao et al. [13]. In the case of very small wire diameters, the strength was shown to depend on the surface stress. One of the most comprehensive MD studies of micropillar comression has been performed by Sanzos [96] on copper pillars with diameter from 11 up to 70 nm. Samples with initial dislocation density were generated by annealing and quenching. The results showed a correlation of the strain necessary for a transition between dislocation exhaustion and source-limited activation with the pillar diameter. Other extensive study of size effect mechanisms of FCC pillars has been performed by Yaghoobi and Voyiadjis [97]. Six Ni pillars of diameters from 22.5 to 135 nm and heights from 30 to 75 nm were simulated along with a large pillar with 150 nm in diameter and a height of 300 nm. The pillars were compressed along an axis parallel to the [111] direction. By analysis of the stress after initial dislocation nucleation, the size effects were observed for 45 nm long pillars with diameter smaller than 90 nm. The dislocation density

evolution as a function of strain suggested a source-limited activation as a leading size effects mechanism for the pillar with diameter of 22.5 nm. In the case of source limited activation, the mobile dislocations are driven out of the sample during loading and the stress increases until a nucleation of a new dislocation. In the 45 nm high pillar with a diameter of 45 nm, the leading size effect mechanism has shown to be the exhaustion hardening where the loss of dislocation sources in small volumes leads to a decrease of the dislocation density with increasing stress.

Due to the restricted scale of MD simulations, the majority of compression cacculations are performed at strain rates higher than the ones used in experimental observation. The effect of strain rate on simulation results has been investigated by Yaghoobi and Voyiadjis [98] on two pillars sized 90x45x45 nm and 300x150x150 nm. The compression of pillars was performed under three different strain rates $6.66 \cdot 10^8$ s^{-1}, $3.33 \cdot 10^8$ s^{-1} and $1.66 \cdot 10^8$ s^{-1}. The investigation of sample strength and dislocation length in the pillars showed that smaller strain rate leads to larger size effects. Studies of yield strength of copper single crystals under different orientations [14] showed increase of yield strength with increasing strain rate. Strain rates between 10^8 and 10^{11} s^{-1} were used in the simulation.

Influence of orientations of copper single crystals on a strain rate has been studied for three different orientations by Dupont and Germann [14]. The largest strengthening with the increasing strain rate occurred along [110] direction, while [111] orientation showed the least dependency. No strengthening along [001] was explained by a rearrangement of atoms from FCC to BCC. A study of plastic deformation mechanisms of Al nanopillars under four different orientations was performed by Xu et al. [99]. Stacking faults bounded by partial dislocations prevailed in [001] oriented nanopillars while full dislocations played main role in deformation of [111], [112] and [265] oriented nanopillars. Compared to [112] and [265] oriented nanopillars, more slip systems nucleated in [001] and [111] oriented pillars, which leads to more frequent dislocation interactions and therefore less probable achievement of dislocation-starved condition and smaller fluctuations of flow stress.

Many different parameters of the compression simulation have been investigated including effect of selected boundary conditions [100], grain boundary effects [101], and temperature [14].

2.3 MD of thin films: deformation of polycrystals

Experimental observations of a grain rotation along with other processes such as grain coarsening and dislocation motion during plastic deformation in polycrystalline materials motivated the use of MD for simulations of grain boundary effects on deformation mechanisms.

Van Swygenhoven et al. [102] used atomistic approach to model plastic behavior of two FCC metals with different stacking fault energies, Ni and Cu. A transition from an intergrain to an intra-grain plasticity was observed under critical grain sizes with values depending on the stacking fault energy. At the smallest grain sizes the GB sliding prevailed as a dominant mechanism while at higher

grain sizes intrinsic stacking faults produced by a motion of Shockley partial dislocations were observed. The effect of grain size on deformation mechanisms of nanocrystalline FCC metals was further studied by Yamakov et al. [103, 104]. A nanocrystalline Al film with four grains oriented by rotations around [110] z-axis was deformed under constant tensile load at 300 K. An EAM potential modified for Al so that stacking-fault energy increased from 104 mJ/m^2 to 122 mJ/m^2 was used in the simulation. Results revealed extensive deformation twinning produced by both successive emission of Shockley partials from the grain boundaries onto neighboring slip planes and dynamical overlap of the stacking faults as well as dislocation-slip mechanism for large plastic strains (12%). Tensile deformation of 15 nm thick Al sample consisting of 15 grains with sizes of approximately 14 nm with grains created using by the Voronoi construction using random grain orientations was used to study the stress-driven grain boundary motion in nanocrystalline thin films [15]. The simulation showed stress-driven GB motion, grain growth and surface topography changes related to step heights at grain boundaries and grain rotations.

Considerable attention has been directed on the influence of GB on the indentation produced deformation mechanisms. GB acting as a dislocation sink and GB sliding when the indenter-substrate surface contact area becomes comparable to the grain size has been observed in 3D samples with mainly high-angle GBs and average grain sizes up to 20 nm [105, 106, 107]. Cooperative GB sliding via the formation of shear planes that extend over a number of grains has been observed in simulations of Ni with an average grain size of 6 nm [108]. Heterogeneous nucleation (which has a lower athermal threshold stress than that of homogeneous nucleation inside the perfect lattice) of partial dislocations has been observed on Cu samples with an average grain diameter of 10 nm [109]. Only partial dislocations nucleated at GBs propagating without trailing partial have been observed under compression or tension in grains with diameters under 50 nm [110, 107]. Two possible explanations were proposed, a relaxation of GB after the nucleation of the leading partial making the nucleation of trailing partial more difficult or simply the trailing partial does not nucleate in a short simulation time typical for MD. Full dislocations have been observed in Al with 2D-columnar grains of the size higher than 20 nm [111]. Yoon, Kim and Jang [112] observed lattice dislocation absorption induced GB migration. Hasnaoui et al. [113] report more complex interactions of lattice dislocations with GB in indentation simulations of nanocrystalline Au using an indenter smaller than the grain size, revealing that GB can emit, absorb and repel dislocations. Simulations of grain structure stability in Cu samples with a variety of boundary types under suitably high stress imposed by nanoindentation predict for nanocrystalline FCC metals with high-angle random boundaries a high probability of the grain size instability for grains with sizes below 50 nm at absolute zero or below 70 nm at room temperature [114]. The grain growth then leads to a decrease of strength characteristics. A stability of FCC materials under the same conditions was reached in samples with optimal nanotwined structures.

Interactions of dislocations with grain boundaries investigated using $\sum = 5$ (210) [001] grain boundary parallel to the indentation surface showed that the dislocation transmitted across the grain boundary leaves a step in the boundary plane [115]. For comparison, the indentation of the sample with a and without the

grain boundaries showed that the indentation was slower in the first case, which was ascribed to the interaction of dislocations with the GB.An effect of a single surface step was studied by Zimmerman et al. [116], showing that the load necessary for the heterogeneous nucleation of dislocations decreases significantly in the vicinity of the step.

3. Experimental methods

3.1 Material

Aluminum films with thicknesses of 50 and 150 nm were prepared by DC magnetron sputtering. A target with a diameter of 50 cm cut from a 1 mm thick sheet of Al3wt.%Mg alloy of a technical purity was used in the sputtering process. The film was sputtered in argon under 0.34 Pa working pressure onto a glass substrate partially covered by a polymer tape. Low working pressure was chosen to prevent the formation of alumina oxide Al_2O_3 and therefore ensure the purity of sputtered film. Current and voltage values during the deposition were $\approx$ 100 mA and $\approx$ 5 V, the deposition rate was $\approx$ 30 nm/min.

3.2 Sample preparation

To obtain a free standing sample for TEM observations, the tape with film was cut into pieces which were attached to a TEM copper grid with 3 mm diameter by a conductive glue and subsequently the polymer was dissolved by repeated rinsing in toluene and acetone.
The samples for in-situ tensile experiments were prepared in scanning electron microscope (SEM) Zeiss Auriga using focused ion beam (FIB). Dog-bone shape was cut from the film and secured onto Hysitron Push-to-Pull (PTP) device (fig. 3.1) with stiffness 150 N/m by a layer of platinum deposited by gas injection system (GIS).

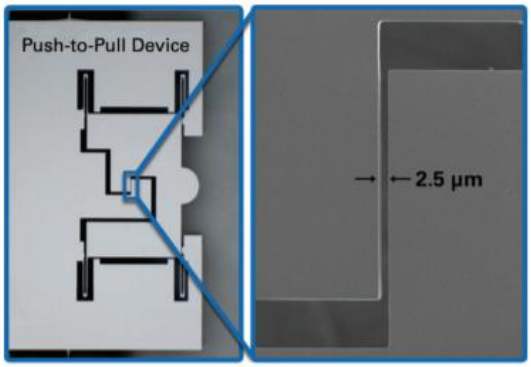

Figure 3.1: Push-to-pull testing device from Bruker [117]

3.3 Transmission electron microscopy

The material was characterized by conventional TEM in BF, scanning transmission electron microscopy (STEM) and automated crystal orientation phase at TEM JEOL 2200FS operated at 200 kV equipped with "Spinnig Star" electron precession from NanoMEGAS with an ASTAR software package.
In automated crystal orientation mapping, a precessing electron beam is scanned over the sample while collecting electron diffraction patterns from different spots

of the scanned area (fig. 3.2a). The collected patterns are than compared with the software generated patterns of the chosen lattice structure (fig. 3.2b).

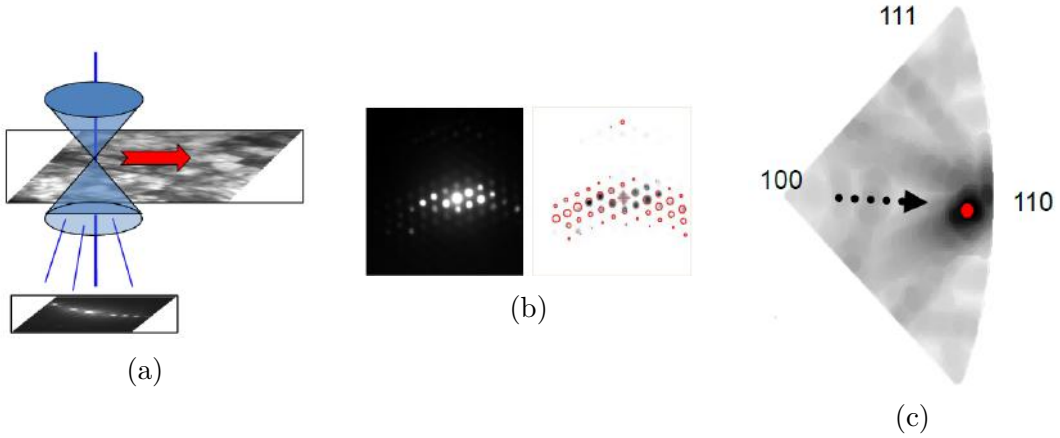

(a) (b) (c)

Figure 3.2: (a) Schematic images of a precessing beam scanning along the sample, (b) illustration of diffraction pattern matching, (c) correlation indices plotted in a stereographic triangle [118].

The beam precession reduces dynamical effects of the electron diffraction so that kinematical diffraction theory is used to compute the template diffraction patterns. In the template, each reflexion is characterized by the position of the diffraction spot (x and y) and by its intensity. The best match between the template and the experimental diffraction patterns automatically determined as a value with the highest correlation index defined as

$$Q_i = \frac{\sum_{j=1}^{n} P(x_j, y_j) T(x_j, y_j)}{\sqrt{\sum_{j=1}^{n} P^2(x_j, y_j)} \sqrt{\sum_{j=1}^{n} T_i^2(x_j, y_j)}} \tag{3.1}$$

is used [119]. In this equation, the intensity function P(x,y) represents the diffraction pattern and the function T_i(x,y) ranges through the diffraction spots in each template. The most probable crystal orientation along with its reliability can be visualised by plotting calculated correlation indices to a standard stereographic triangle (fig. 3.2c) where darker color implies a higher correlation index. The most probable crystal orientation shows as a black dot for the highest reliability orientation, several dots for more orientations with a similar correlation index or a dark line if only one direction is unambiguously determined. The orientations maps were captured at camera length 20 cm. Steps (1-3 nm) were selected in order to optimize capture time and image resolution.

3.4 In-situ TEM deformation testing

The deformation was realized by Hysitron PI 95 TEM PicoIndenter equipped with a Berkovich indenter for direct indentation or flat punch for nanopillar compression and for the PTP device pushing (fig. 3.3).In addition to a three-axis coarse positioner and a 3D piezoelectric actuator for fine positioning, the Hysitron PI 95 is equipped with a transducer for electrostatic actuation and capacitive displacement sensing which provides highly accurate depth-sensing capability.

The samples were deformed at strain rate 10^{-4} s^{-1} and the force and displacement of the indenter were captured every 5 ms.

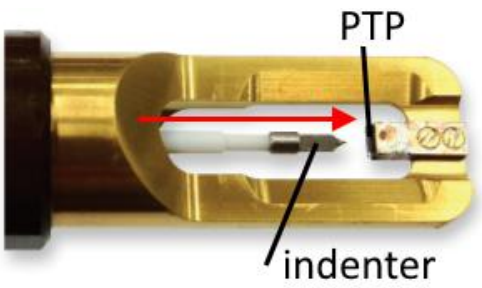

(a)

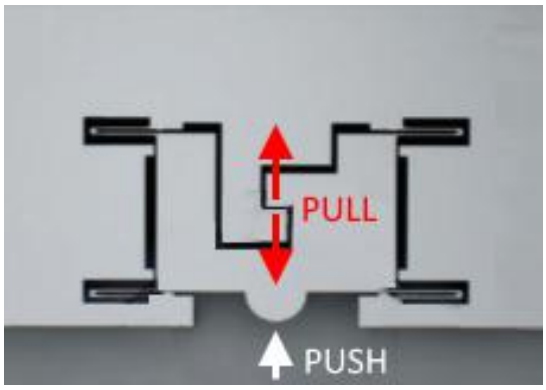

(b)

Figure 3.3: (a) Hysitron PI 95 TEM PicoIndenter [120], (b) direction of indenter pushing and pulling of the sample in PTP device [117].

3.5 MD simulation methods

Large-Scale Atomic/Molecular Massively Parallel Simulator [121] was used for MD computing. A code for deformation of a predefined block of material was constructed. At first, the energy of the whole system is minimized at zero temperature, following by a calculation of the distribution of velocities of atoms at defined temperatures. The system is then left still for 5 ps with the temperature controlled by Nose-Hoover thermostat from isothermal-isobaric ensemble. Again, the energy minimization is performed and the block is then deformed at given strain rate at temperature 300 K controlled by Nose-Hoover thermostat from the canonical ensemble. Timestep used in the integration is 10^{-15} s. Each 1000 integration steps, computed atom positions and energies along with a total energy of the system, its stress, strain, volume and temperature were recorded.
Polycrystal blocks of atoms used for deformation were created by Atomsk [122]. Atomsk uses a Voronoi tesselation (fig. 3.4) to construct polycrystals, the atomic seeds were placed so that four hexagonal grains parallel in z direction were created inside the box (Fig. 3.5).
Open Visualization Tool (OVITO) with the common neighbor analysis and dislocation analysis was employed for the visualization analysis of atomic structures [123].

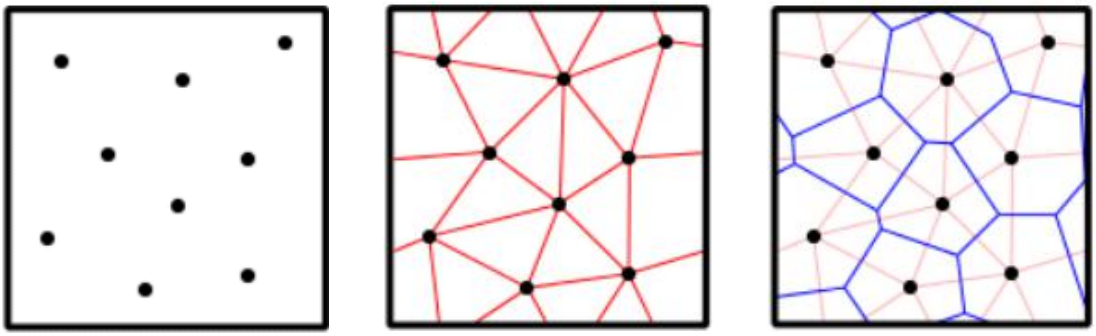

(a) (b) (c)

Figure 3.4: Construction of 2D polycrystals by Voronoi tesselation (a) introduction of nodes at given positions, (b) linking of neighboring nodes, (c) normals to the linking lines define future grain boundaries.

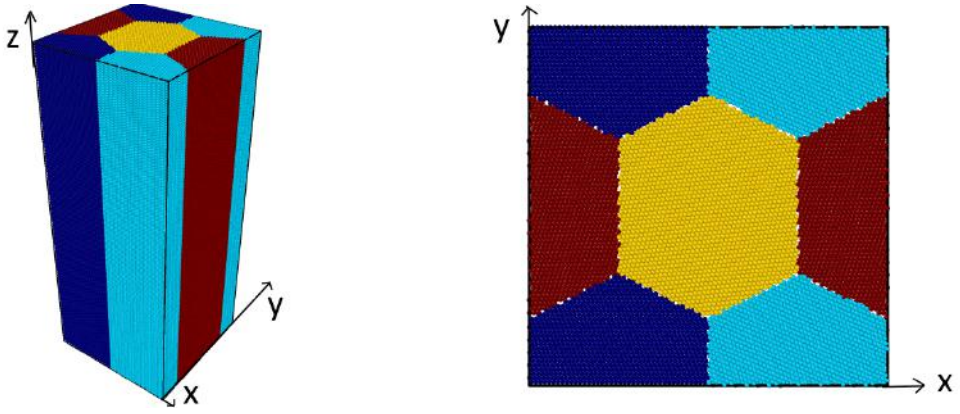

Figure 3.5: Block of atoms with hexagonal grains created by Atomsk.

4. Results A

4.1 Material characterization

Bright field TEM images (fig. 4.1) reveal polyhedral grains with evenly distributed sizes in both film thicknesses. The grain size in the 50 nm thick film ranges from 10 to 40 nm whereas in the 150 nm thick film, the sizes vary between 10 and 60 nm. A moderate overlap between several neighboring grains can be observed in both images.

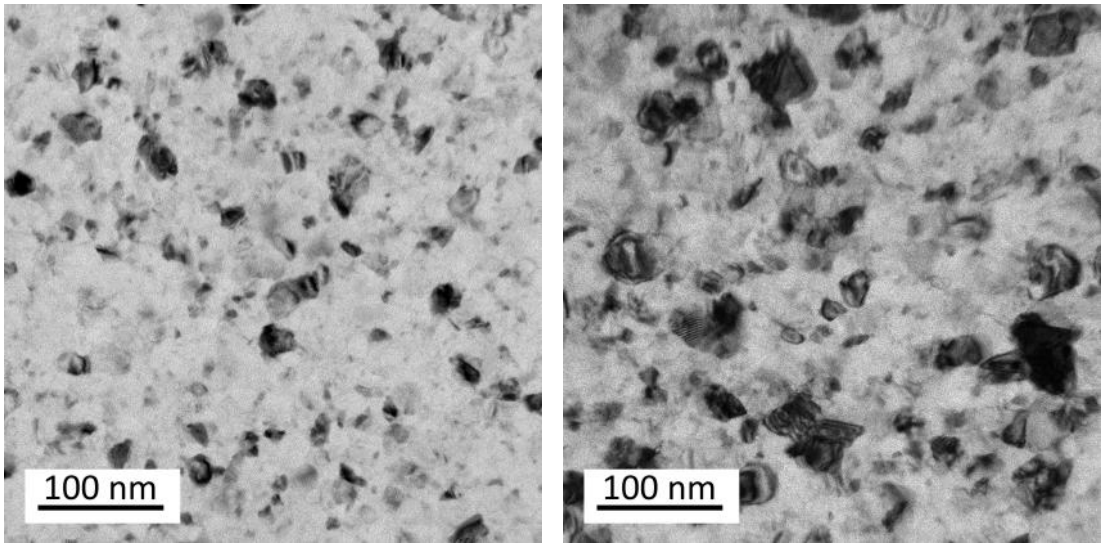

(a) (b)

Figure 4.1: TEM BF plane-view of a) 50 nm b) 150 nm thick sputtered film.

The grain structure of both 50 nm and 150 nm thick as sputtered films was characterized by conventional TEM and ASTAR orientation mapping. The called columnar growth of the grains is characteristic for films prepared by sputtering deposition [124]. The individual grains start their growth at preferential sites and rise in the direction perpendicular to the surface in a form of expanding columns as the sputtering proceeds. The expansion of columns nucleated with crystallographic orientation with enhanced growth ((110) direction in Al [125]) is faster and their larger area captures more and more incoming sputtered material. With a preferential growth of the highest columns, screening of their lower neighbors occurs, which results in a formation of a characteristic columnar structure. Higher thickness of the deposited films should therefore lead to an increase in an average grain size.
Both overlapping and an increase of the size of largest grains with increasing thickness affirm the assumed structure constructed by columnar grain growth. The presumed columnar structure of the grains was further confirmed by tilting the specimen from the axis of the columnar growth with respect to the direction of the incident electron beam. STEM images of untilted and tilted specimens show clear elongation of grains in the crystal growth direction.

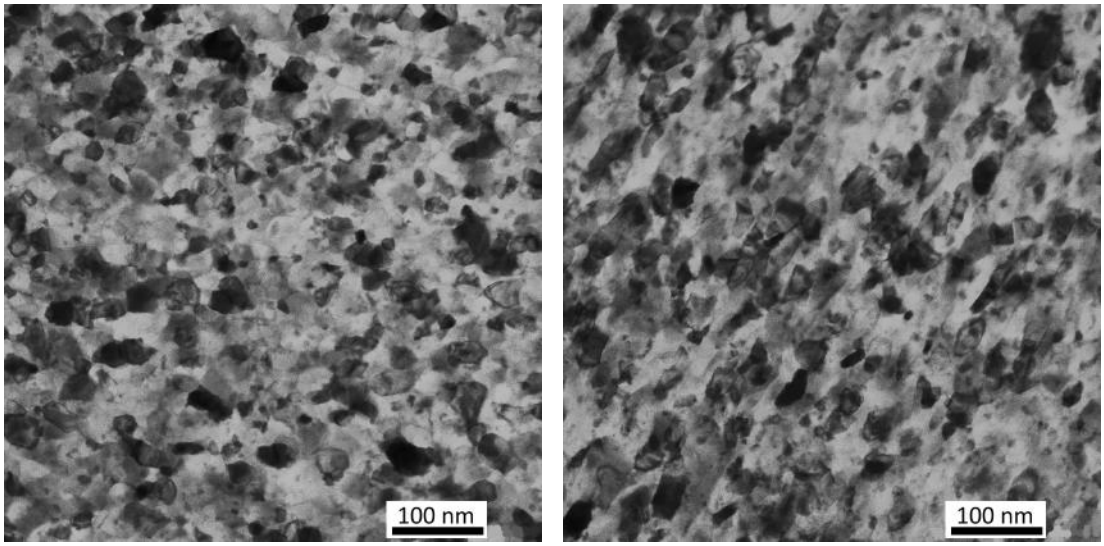

(a) (b)

Figure 4.2: STEM BF images of 150 nm thick film a) no tilt, b) tilted by 20°around the goniometer axis.

The orientation distribution of grains was examined by automatic phase and orientation mapping in TEM. Orientations maps shown in Fig. 4.3 reveal a random character of grain orientation distribution in axes (x,y) parallel with the sample surface (fig. 4.3a, 4.3b, 4.3d, 4.3e) whereas in the axis (z) perpendicular to the sample surface (fig. 4.3c, 4.3f), a preferential Al-[101] orientation is clearly visible for both film thicknesses. Reliability of the orientation fit is shown in fig. 4.3g, where the reliability value is computed as a difference between two highest correlation indexes, higher index value being assigned to the orientations with the better match with the substrate. The areas with lower reliability are filled with darker colors. The captured maps show relatively high values of reliability in most of the grain interiors and predictable low values around grain boundaries. The main factors causing this ambiguity in orientation determination are the overlap of grains as well as general orientation of specific grains with weak and scarce diffraction spots. In this case, the diffraction spots from the previous scanning step may still be visible on the camera screen due to its relatively long relaxation time interfering with the captured diffraction spots. In some cases, grains in the orientation maps appear larger than the maximum grain sizes observed in BF TEM. The reason is either clustering of several grains with similar orientations and/or the above mentioned overriding of weak diffraction spots by a strong pattern from the previous scanning step. The images were taken from an area 500x500 nm^2 with scanning step 2x2 nm^2, which is at the limit of maximum resolution achievable by ASTAR.

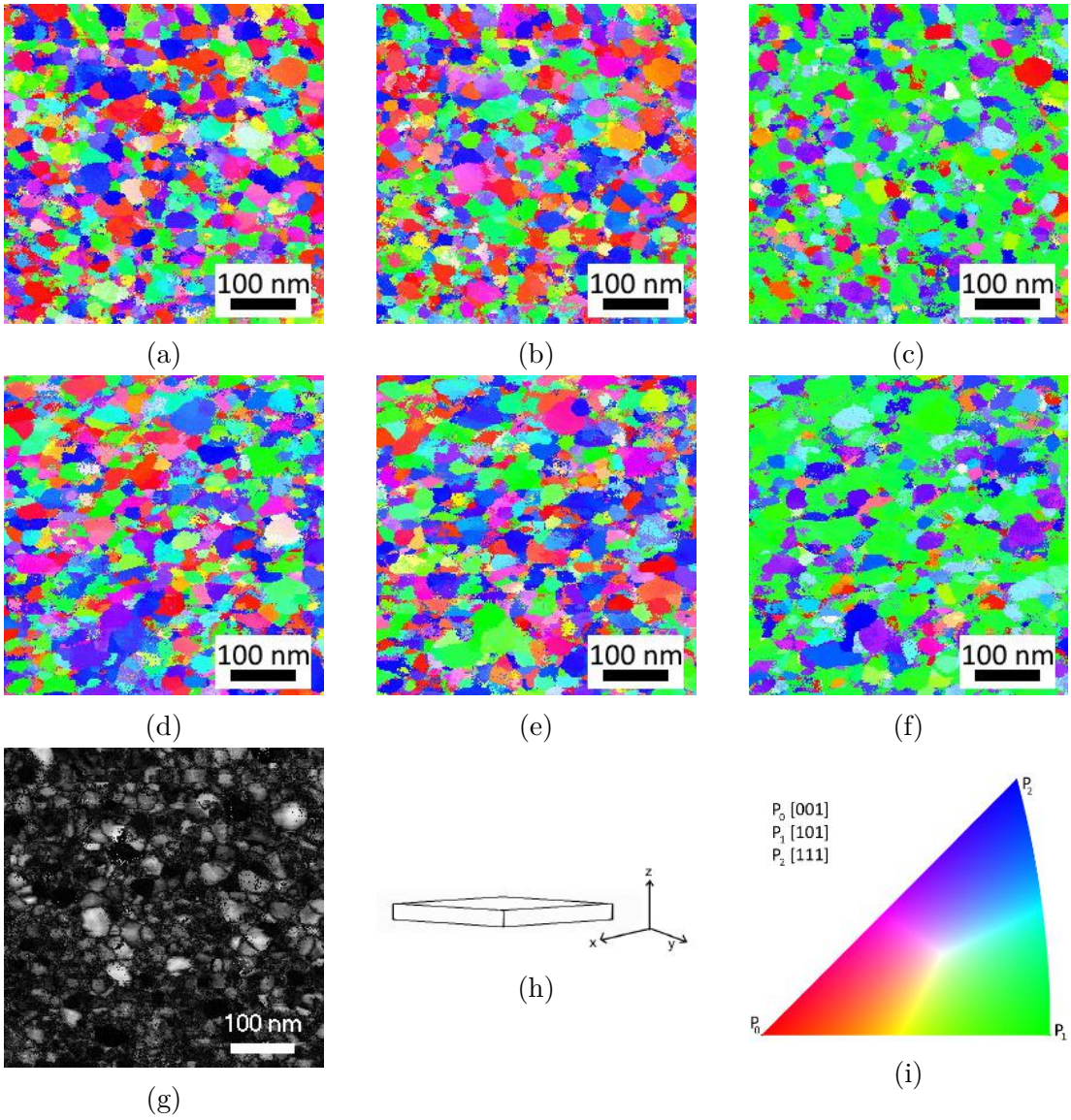

Figure 4.3: ASTAR orientation maps of 50 nm (a-c) and 150 nm (d-f) thick sputtered films for three respective directions x,y,z shown in h), g) reliability map of 50 nm thick film, e) orientation triangle

4.2 Annealing

Annealings of samples were necessary in order to get rid of internal stresses originating from the method of the film production causing difficulties with the sample operation in SEM. The films were annealed in situ in TEM for 40 min at 450 °C and the comparison of as-deposited and annealed films are shown in fig. 4.4.
In both cases, abnormal growth of several grains at the expense of their energetically less favourable neighbors was observed. In the aftermath structure, the size of the smallest grains remained around 20 nm. In the annealed structure size of the majority of grains ranges up to 80 nm while diameters of some of the largest grains evenly distributed in the sample exceed 200 nm in both films. Sharp clear line contrast changes indicating a formation of annealing twins were detected in both films along with extensive growth of certain grains (fig. 4.5a, 4.5b). The

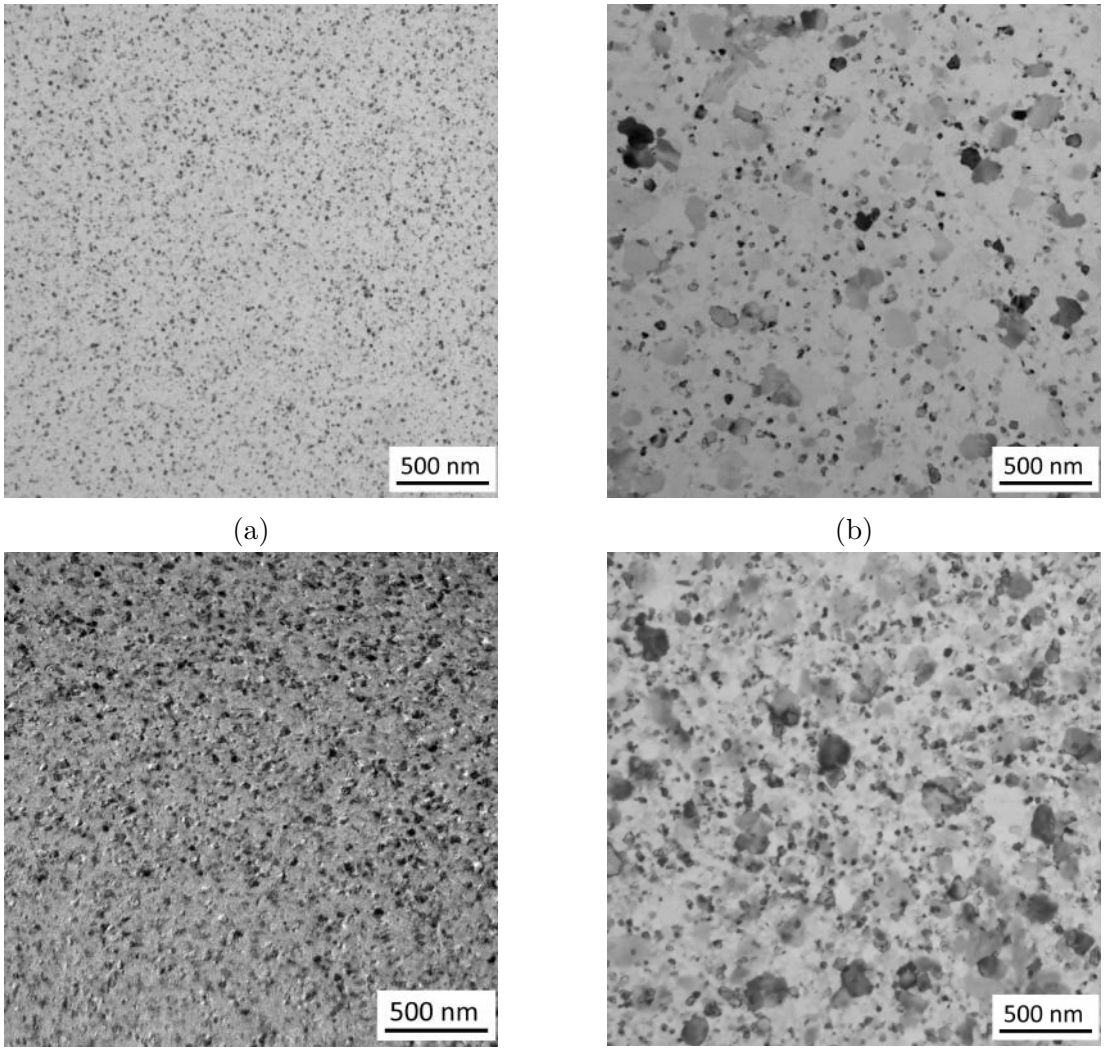

(a) (b)

(c) (d)

Figure 4.4: TEM BF images of 50 nm (a,b) and 150 nm (c,d) thick films before (a,c) and after (b,d) annealing up to 450 °C.

boundaries were further investigated by HRTEM and indeed, a mirror symmetric axes of neighboring atomic planes along the twin boundary were found (fig. 4.7c). ASTAR orientation maps of annealed samples (fig. 4.6) show aside from an obvious grain growth a partial suppression of the texture, however the [110] direction oriented perpendicularly to the film surfaces still prevails (fig. 4.6c, 4.6f). Also the presence of annealing twins was confirmed by ASTAR (white circles in fig. 4.6b, 4.6c).

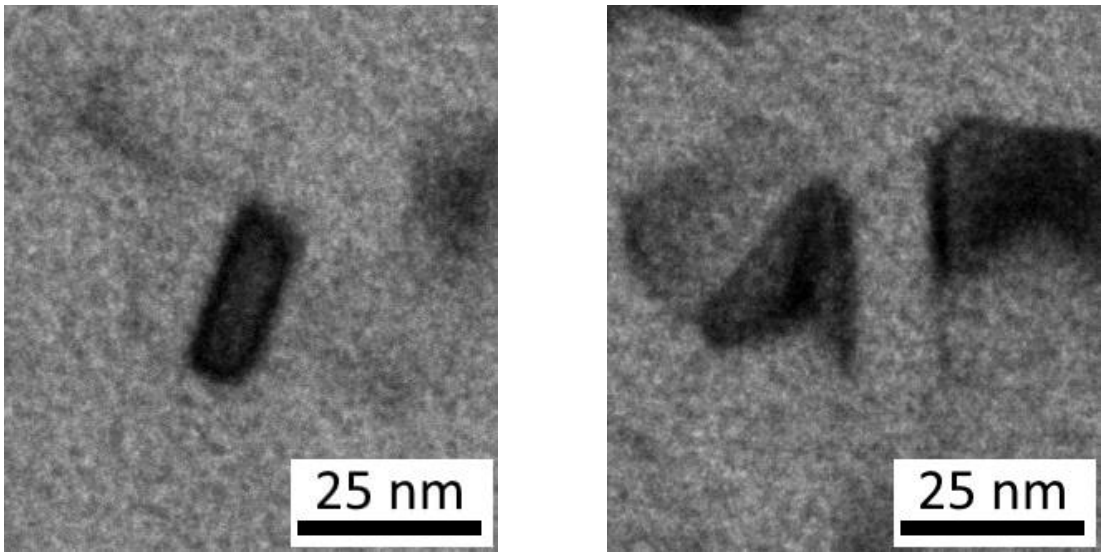

(a) (b)

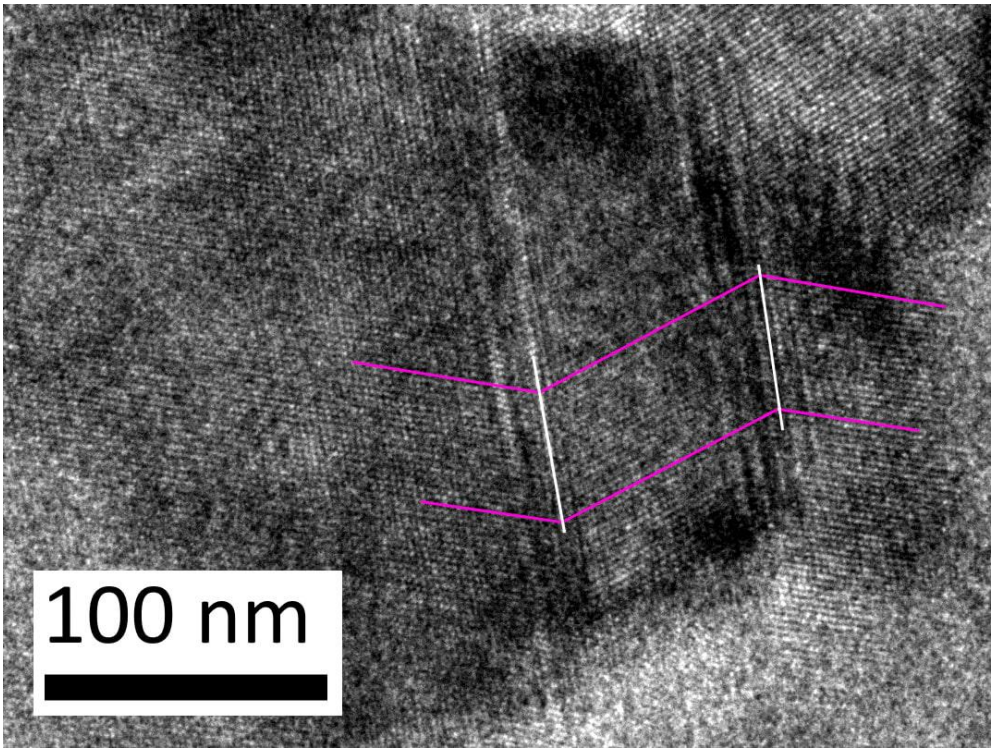

(c)

Figure 4.5: Images of annealing twins a), b) BF, c) HRTEM.

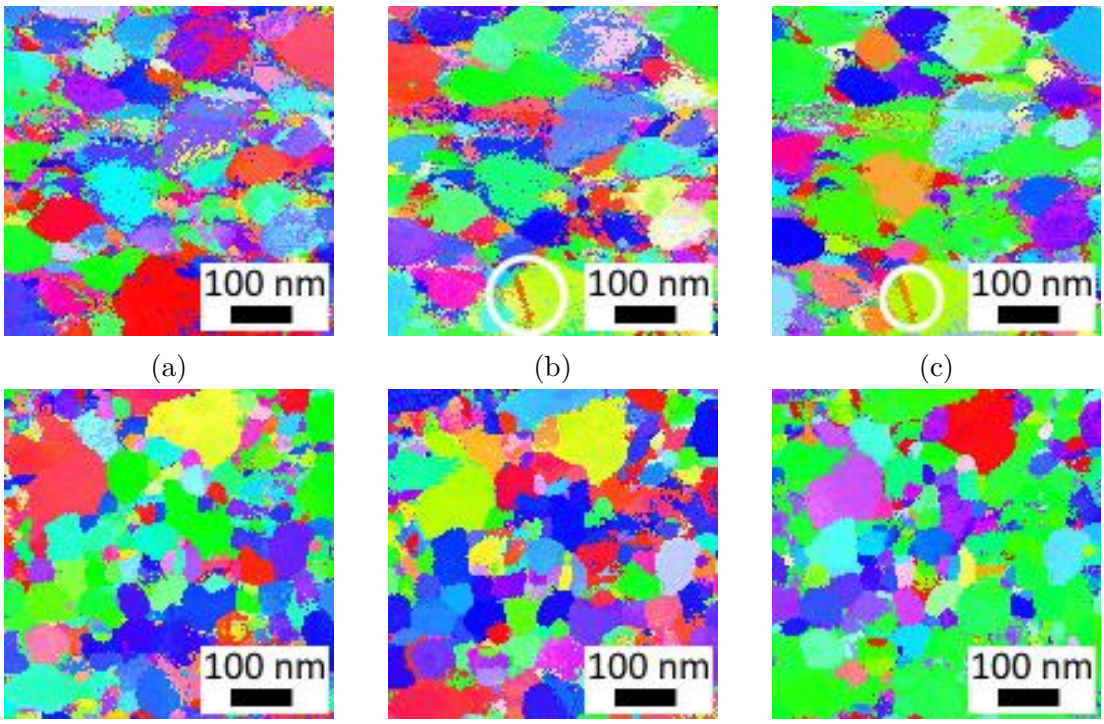

(a) (b) (c)

(d) (e) (f)

Figure 4.6: ASTAR orientation maps of 50 nm (a-c) and 150 nm (d-f) thick annealed films, the directions and orientation triangle remain the same as in fig. 4.3

.

4.3 Tensile experiments

Fig. 4.7 represents an overview of the microstructure evolutions in both annealed films during in-situ straining. In order to obtain relevant information about the sample elongation during straining, the entire active region was captured in either series of pictures with regular time intervals or on a video with capture rate 2000 frames per second. The benefit of the first method lies in a better resolution of acquired images, while the video is able to record rapid ongoing processes. Although a slightly better resolution was attained in the 50 nm thick film, grains suitably oriented for a good TEM contrast could be formed in both cases.
Extensive contrast changes in the BF images appear during straining. Aside from general contrast changes propagating through the whole area, rapid ones of individual grains were observed. While the first case results from global changes in the orientation between the sample and incident beam due to the motion of the whole deformed sample and MEMS, the second case can be attributed to elastic accommodation processes and local orientation deviations rooting from either grain rotations or a deformation of the film via lattice or grain boundary dislocations. Although no extensive presence of inside grain lattice dislocations was detected during the straining, a rapid propagation of low density dislocations through the grains and their consecutive annihilation at opposite grain boundary cannot be excluded.

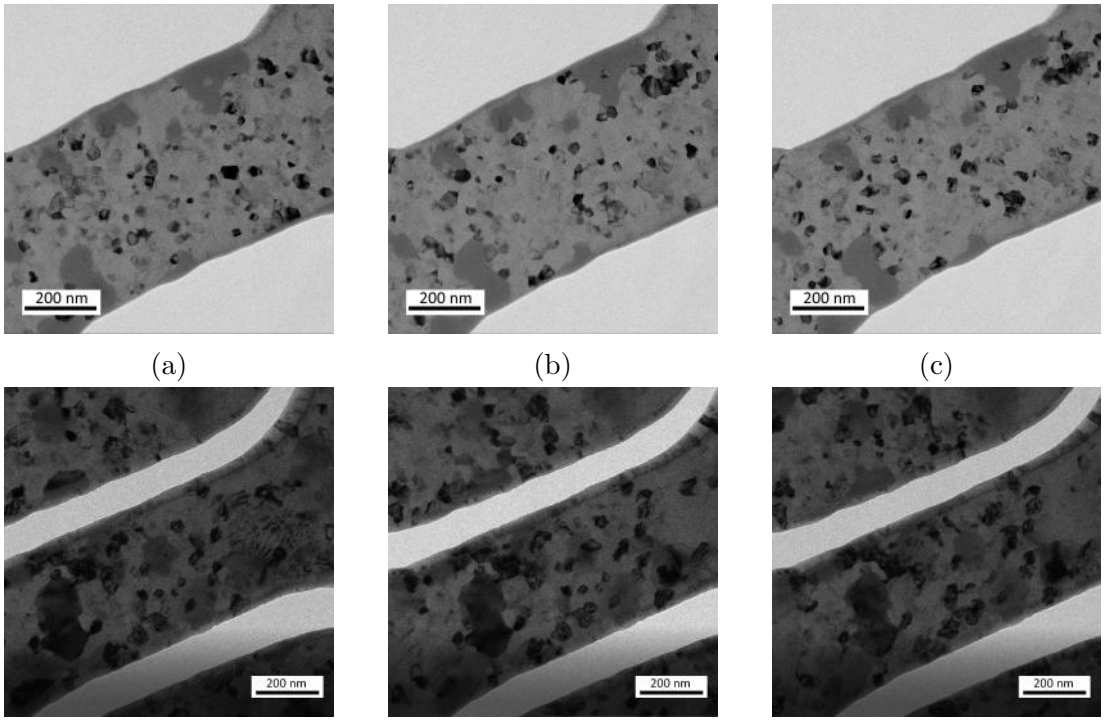

Figure 4.7: Active area during deformation a-c) 50 nm, d-f) 150 nm, strain: a,d) 0 %, b,e) 3%, c,f) 7%.

In a typical nanoindentation experiment, the force on the indenter is measured as well as its position as a function of time. When using the indenter to push into the MEMS device, these raw data, especially information about displacement become

unreliable since the position of the indenter, does not match the real elongation of the deformed area transferred by the MEMS PTP device. For this reason, real deformation as a function of time was measured directly from the images captured during the deformation and coupled with corresponding force values. The conversion to stress-strain curves was done again by using the measured length and width of the sample at the beginning of the deformation and assuming that the initial sample thicknesses do not deviate far from predicted values of 50 nm and 150 nm. Examples of the resulting stress-strain curves together with raw data received from the indenter position are shown in fig. 4.8.

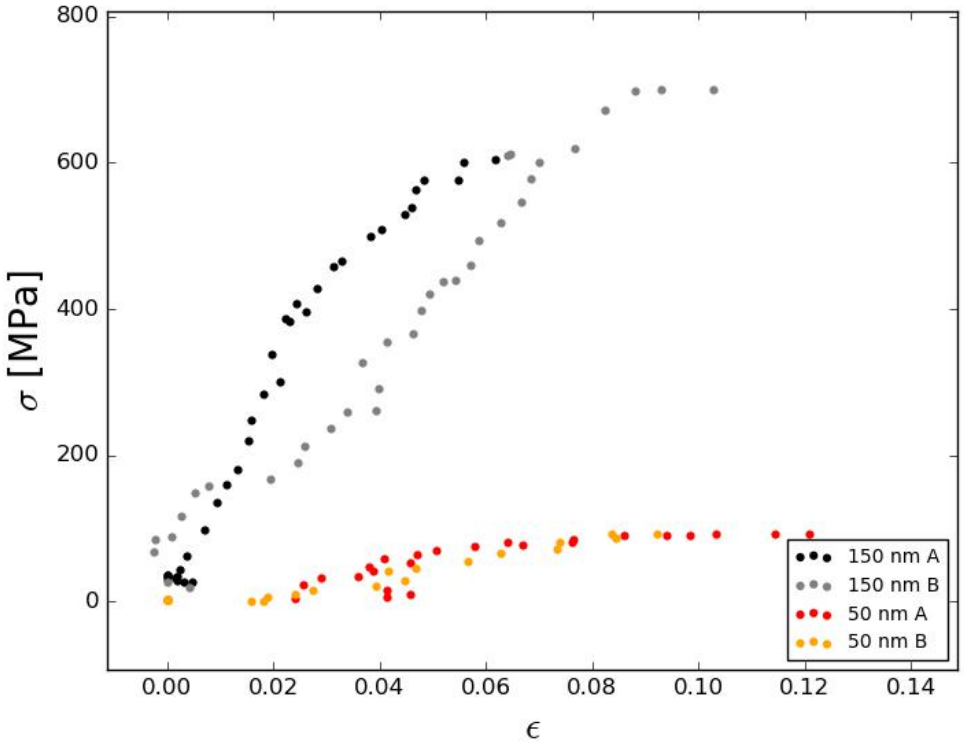

Figure 4.8: Stress-strain curves of the tensile deformation of two 50 nm and two 150 nm thick annealed films.

The first evident result is a markedly lower strength of the 50 nm thick film opposed to 150 nm thick film. Although the diameters of the grain projections after annealing of both samples and described earlier do not significantly differ, the volumes at single grains are still considerably larger in 150 nm thick film. Therefore, the measured strength increases with the average grain size which is a result compliant with the already observed inverse Hall-Petch relationship [49]. In spite of large difference in strength, the fraction of both films occur at relatively similar total strains (ductility around 10% in 150 nm thick films and slightly larger in the thinner film ≈12%). Significant decrease of the slope around 2% strain before the failure evident mainly on curves of 150 nm thick films can be ascribed to onsets of cracks formation and their further propagation through the sample. Even though the deformation under these values of strain is seemingly essentially linear, a residual plastic deformation indicating the plastic nature of the deformation was measured by comparing the distance of precisely defined

points before and after the deformation. Values of 9% and 7% were obtained respectively for 50 nm and 150 nm thick films.
Detailed monitoring of individual grains in the course of deformation revealed gradual changes of grain shapes. The shapes of three different grains in 50 nm thick film during the deformation (total strains $< 5\%$, fig. 4.9a, 4.9d, 4.9g) and right before the failure (total strength 12%, fig. 4.9b, 4.9e, 4.9h) together with overlap of the boundaries of the final grain shapes outlined in pink and the initial grain shape (fig. 4.9c, 4.9f, 4.9i) show a general trend of grain elongation along the deformation axis in the range of units of nm as well as their contraction in the perpendicular direction.

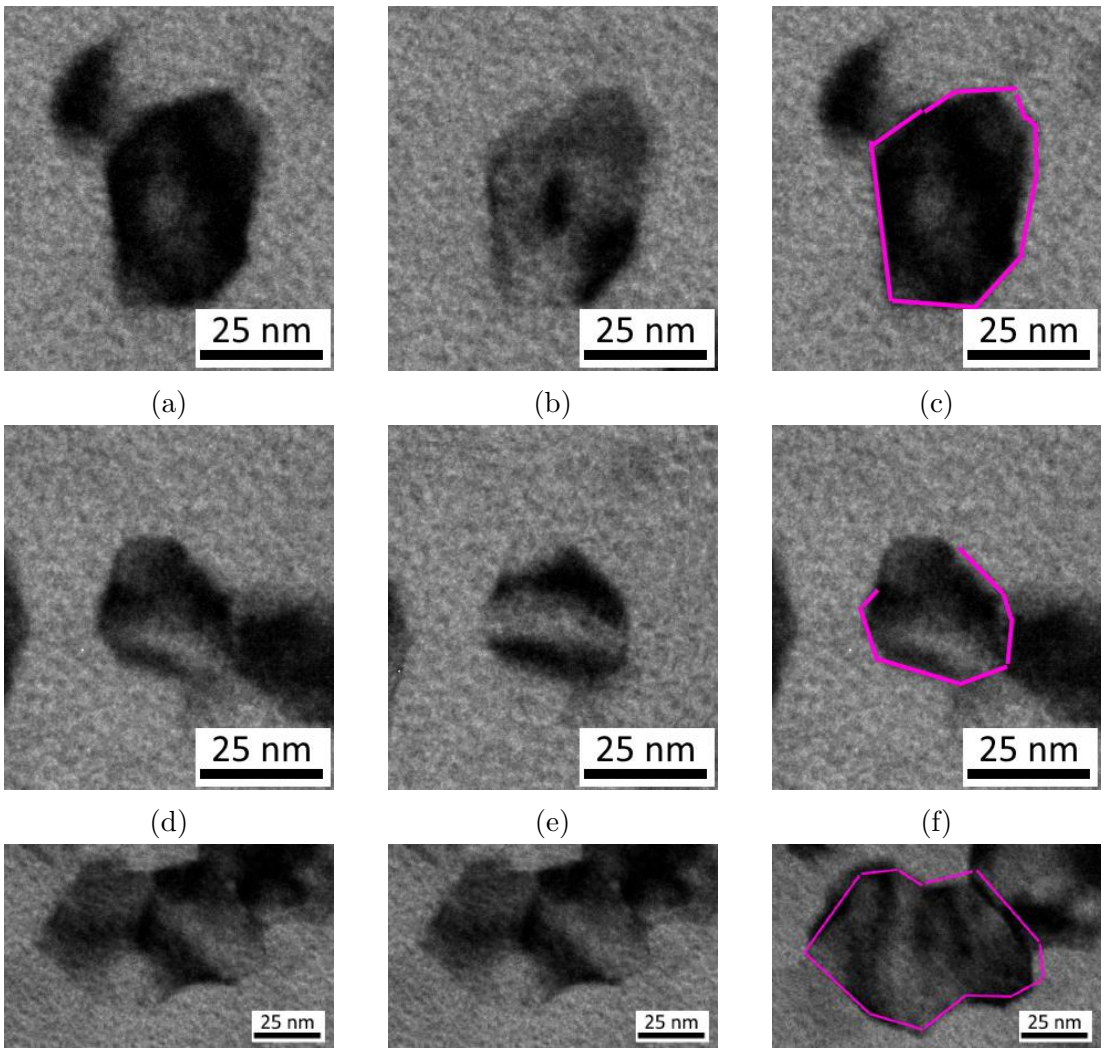

Figure 4.9: Details of grains at $\approx 5\%$ total strain (a,d,g) and $\approx 12\%$ total strain (b,e,h). c,f,i) Projections of final grain boundaries (pink line) from b,e,h) images on grains from a,d,g) images respectively.

Even thought several different grains were checked, majority of them could not be analysed at all stages of deformation due to the already mentioned contrast loss at later stages of deformation. The analysis of a grain containing a twin boundaries oriented roughly perpendicular to the tensile axis (fig. 4.10) demonstrate an evident shift of twin boundaries during the tensile test.

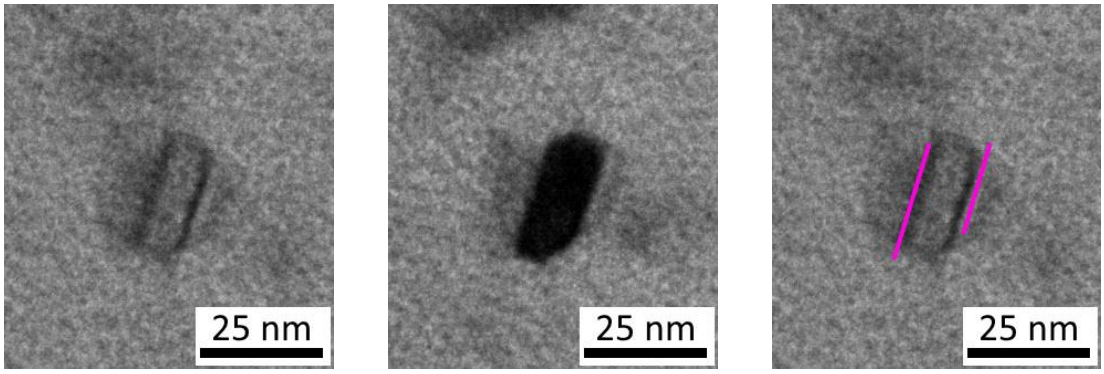

(a) (b) (c)

Figure 4.10: Twin boundaries in a particular grain at ≈ 5% (a) and ≈ 12% (b) total strain. c) Projection of twin boundaries from b) (pink lines) to a).

4.4 Fracture

As already mentioned, no extensive dislocation motion or dislocation interactions with each other or grain boundaries throughout the whole deformed area were observed in either of the film thicknesses. However, solitary dislocation propagating in several grains were captured on video. Fig. 4.11 shows emissions, motion and annihilation of two dislocations in the 150 nm thick film at ≈ 12% strain close the failure of the specimen.

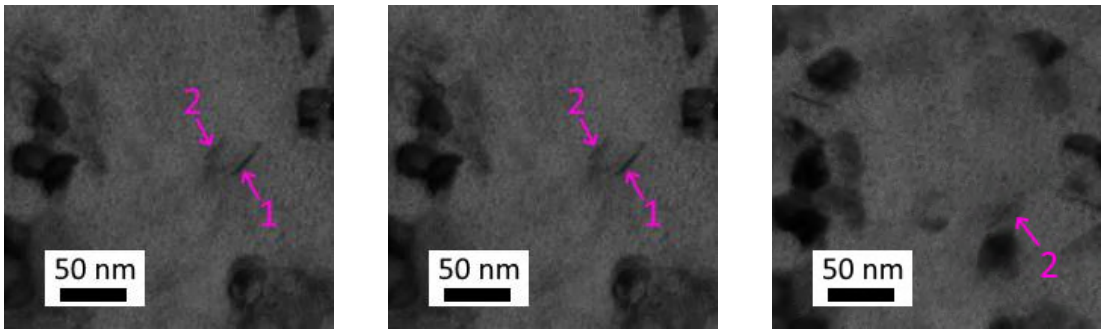

(a) (b) (c)

Figure 4.11: BF images of dislocations near the area of crack formation a) emission of dislocation 2, b) dislocations 1,2 traversing the grain, c) dislocation 1 annihilates is the grain boundary.

Also HRTEM analysis did not reveal the presence of dislocations in strained thin films. Fig. 4.12 shows examples of HTREM images of the 50 nm thick film after the failure. However, it is worth to mention, that the number of analysed grains is statistically very low.
ASTAR images of grain distribution before deformation and after the failure are shown if fig. 4.13.
Corresponding grains in both images were paired and are marked by the same letter in the same color. A change in grain shape is apparent as well in this comparison, while some grains are almost unrecognisable, other remained fundamentally the same or only slightly squished and elongated parallel to the tensile

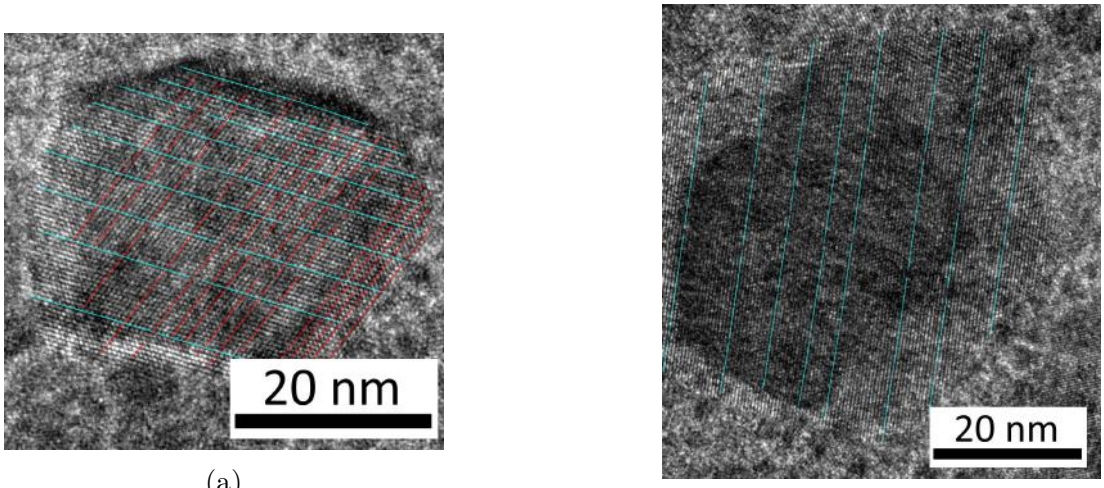

(a) (b)

Figure 4.12: HRTEM images of unperturbed grains near [110] crystal orientation after the failure. Color lines confirm the unperturbed crystal structure.

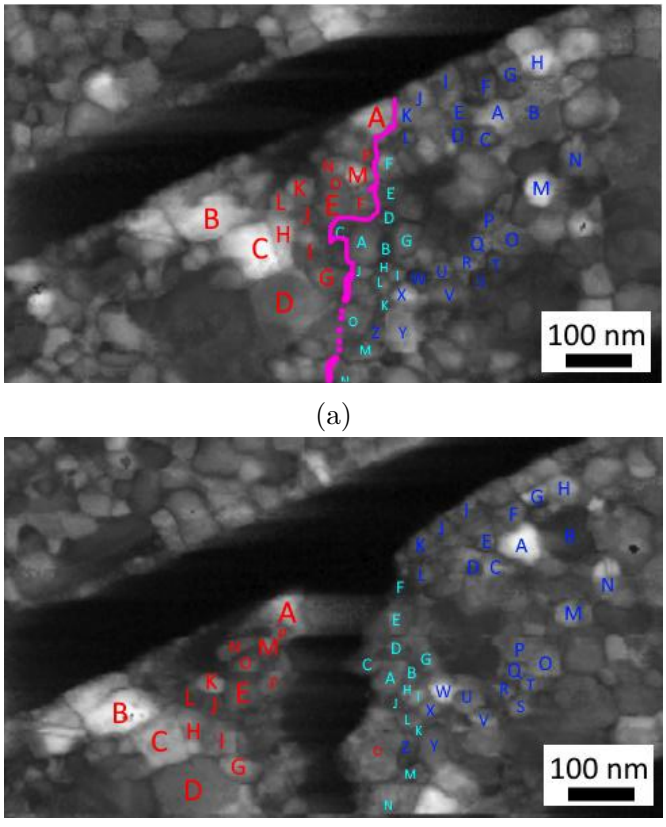

(a)

(b)

Figure 4.13: ASTAR confidence index map of grain distribution a) initial state, b) after the failure.

axis. The images reveal intergranular character of the crack propagation, even though in one area around the grain denoted as red/light blue O it is unclear and it seems like either overlapping grains tore along the boundary and separated or the crack propagated transgranularly and tore the grain in two parts.

4.5 Orientation changes

HRTEM images before and after the deformation were taken from the corresponding areas. Two of notable images are shown in fig. 4.14. The initial twin structure (fig. 4.14a) is distorted (the sequencing of the visible lattice planes in both pictures is highlighted in pink) - the mirror symmetry could be no longer recognised even though the orientation of the lattice planes between the two boundaries remains the same (fig. 4.14b). The left part of the grain apparently underwent a subtle rotation.

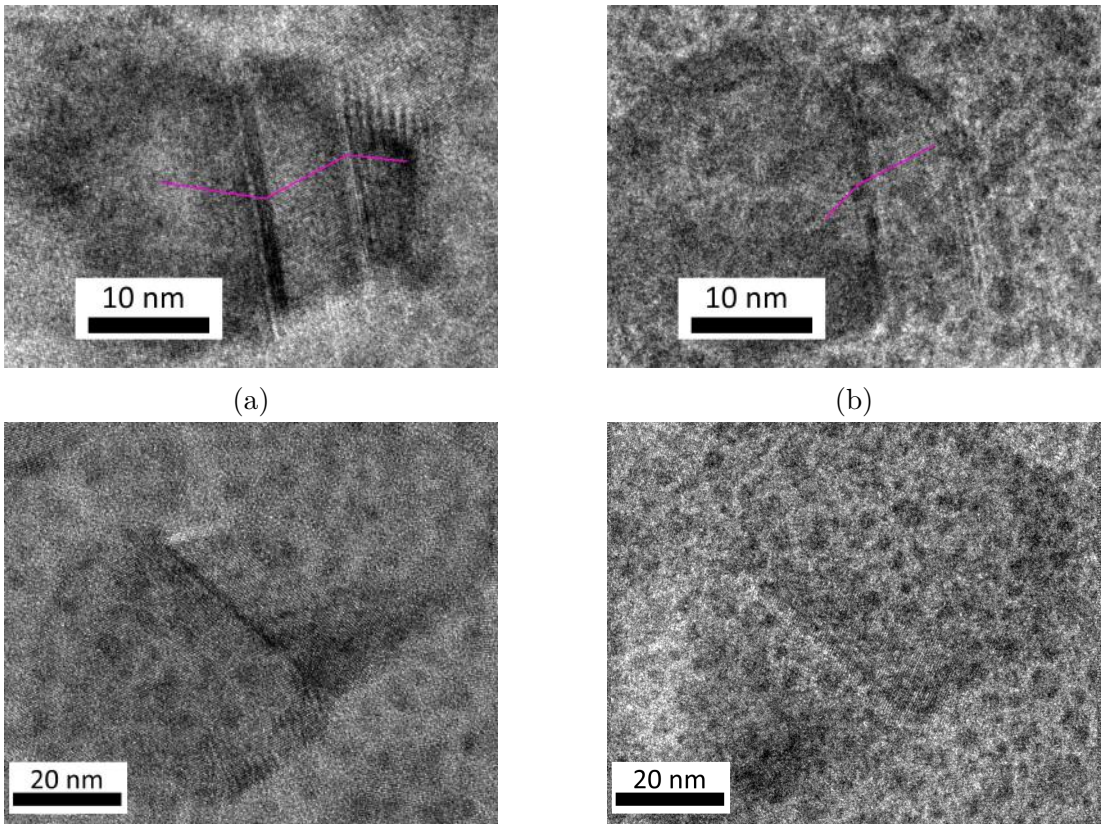

(a) (b)

(c) (d)

Figure 4.14: HRTEM images of twinned grains (a,b) and two adjacent grains (b,c) in 50 nm thick film before (a,c) and after the failure (b,d).

The change of orientation was observed in several other grains where the orientation whole surroundings changed out of low index orientation so it is not apparent whether the change occurred locally for individual grains or rather globally due to the specimen or MEMS tilting (fig. 4.14c, 4.14d).
ASTAR orientation maps of the same area before the start of the deformation and after the failure (fig. 4.15) were taken. Slight changes of the color shades and full changes of color could be recognised between the two stages. The observed features confirm individual grain rotations rather than global area tilting indicating bending of the specimen. To confirm this observation, changes in misorientation angles of neighboring grains were inspected. Graphs of misorientation angles along a line are shown in fig. 4.16a, 4.16d. The misorientations with regards to the orientation of the first pixel in the line are shown and one point in the graph matches one pixel in the image. The corresponding lines are drawn on orientation

maps (left side of fig. 4.16b, 4.16c, 4.16e, 4.16f), in the reliability maps of the corresponding area (right side of fig. 4.16b, 4.16c, 4.16e, 4.16f), grains with high reliability are marked by letters which are matched with the grains in the graph recognisable as consecutive distances of constant misorientation angle. Misorientation changes among individual grains range between 0.5 °and 3 °and fluctuate along the length of the line. These values are above the ASTAR orientation resolution limit, which makes 1 °or less [118]. for This statistical approach confirms that individual grains indeed changed their orientations during deformation via grain rotation. Large orientation fluctuations on pixel scale correspond to areas with low reliability and thus can be omitted, more continuous changes withing larger areas of the same color mark the presence of smaller subgrains.

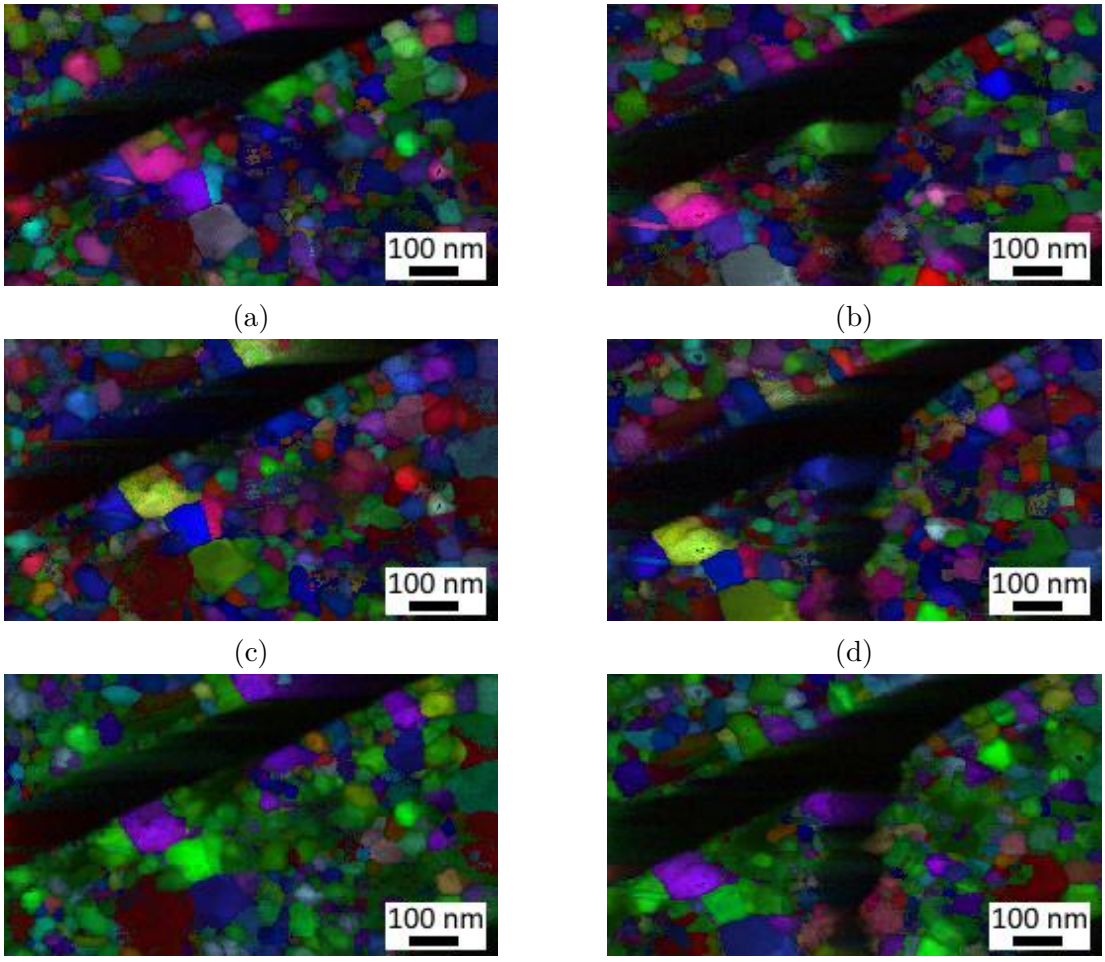

Figure 4.15: ASTAR orientation maps of the sample a,c,e) before and b,d,f) after cracking in a,b) x direction, c,d) y direction, e,f) z direction.

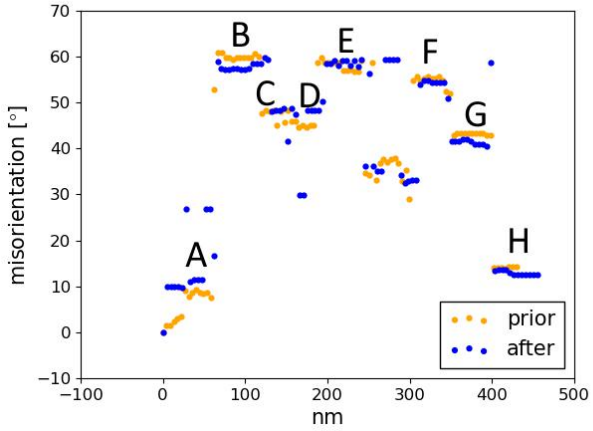

(a)

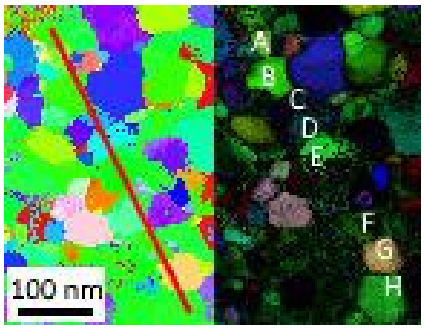

(b)

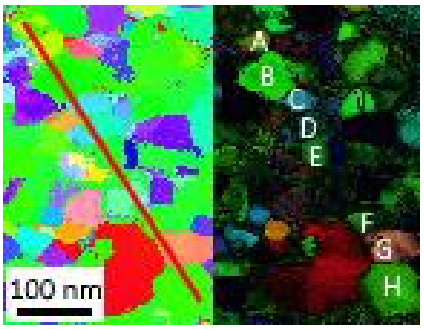

(c)

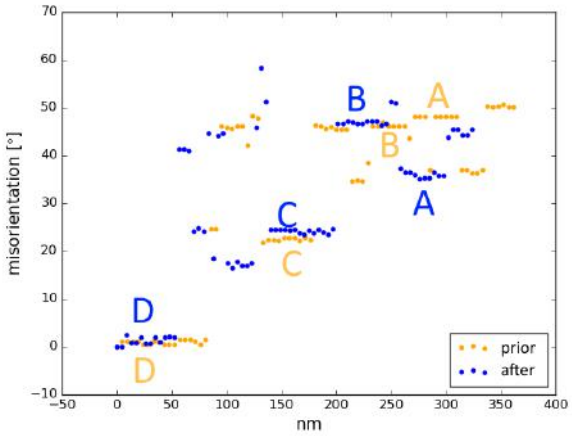

(d)

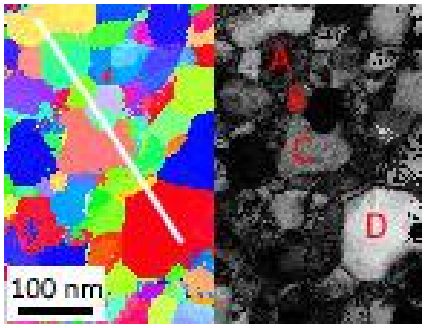

(e)

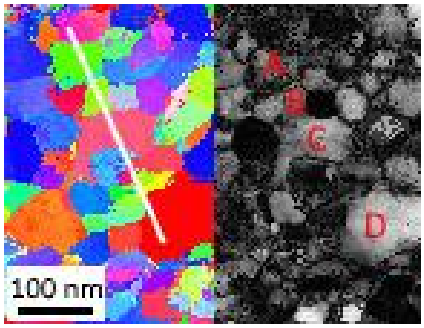

(f)

Figure 4.16: Misorientation along the line with regards to the orientaion of the first pixel: a,d) graph, b,e) initial state, c,f) final state after the failure (150 nm film).

5. Results B

5.1 Potentials

A choice of interatomic potential may influence the course of the simulations and their outcomes. Modified atom potentials MEAM, widely used in MD simulations and suitable both for metallic structures and structures with directional bonding were used in all simulations. While some potentials are derived solely for pure elements, other include multi-element interactions. A presence of Mg in experimental alloy necessitates the use of multi-element potential, however in case of such a potential, interactions between two compliant atoms may deviate from interaction predictions when using potential derived for single element interactions. Since for alloys with low content of additives (as the one used in the experiment), most pair interactions remain A-A (between the same atoms), a question of how much impact does the change of potential from single element to multi-element have on the simulation results arises.
Three different potentials Al-Si-Mg-Cu-Fe MEAM [126] and Al-Mg MEAM [127] for the multi-element computations and Al MEAM [128] for single element simulations were chosen for the execution of following simulations. Basic properties obtained from implementations of the potentials [129] are shown in fig. 5.1 and 5.2.
Fig. 5.1 shows differences of the diatom energy as a function of interatomic distances with fig. 5.1b zooming in the curve for interval of the distances corresponding to common values of interatomic distances in FCC Al. Differences between Al-Al interactions of potentials for atomic spacing in [110] direction, which makes 2.8 Å, seem to be minor.

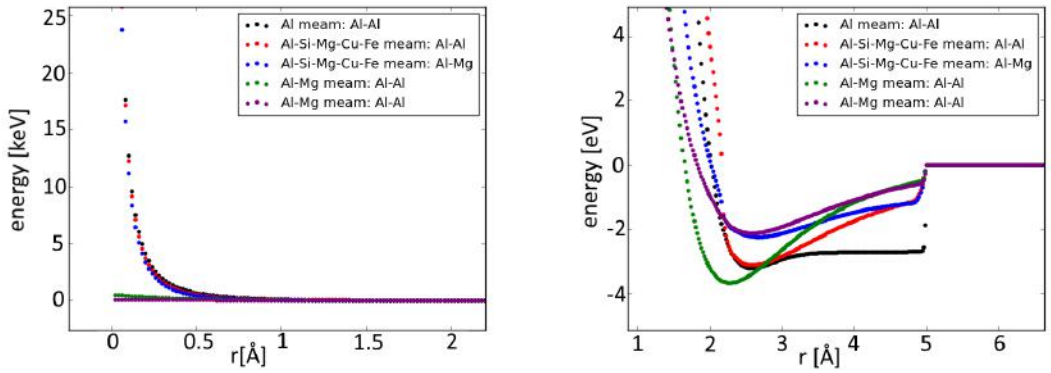

(a) (b)

Figure 5.1: Comparison of diatom energy as a function of MEAM potentials for pure Al (Al-Al interaction), Al-Mg and Al-Si-Mg-Cu-Fe (Al-Al and Al-Mg interaction): (a) 0 to 2 Å, (b) 1 to 6 Å[129].

Different definition of potentials leads among other variances in properties to different values of the stacking fault energy. Predictions of generalised stacking fault energies in FCC structure for pure Al and Al-Si-Mg-Cu-Fe and (111) atomic planes in different directions are plotted in fig. 5.2.

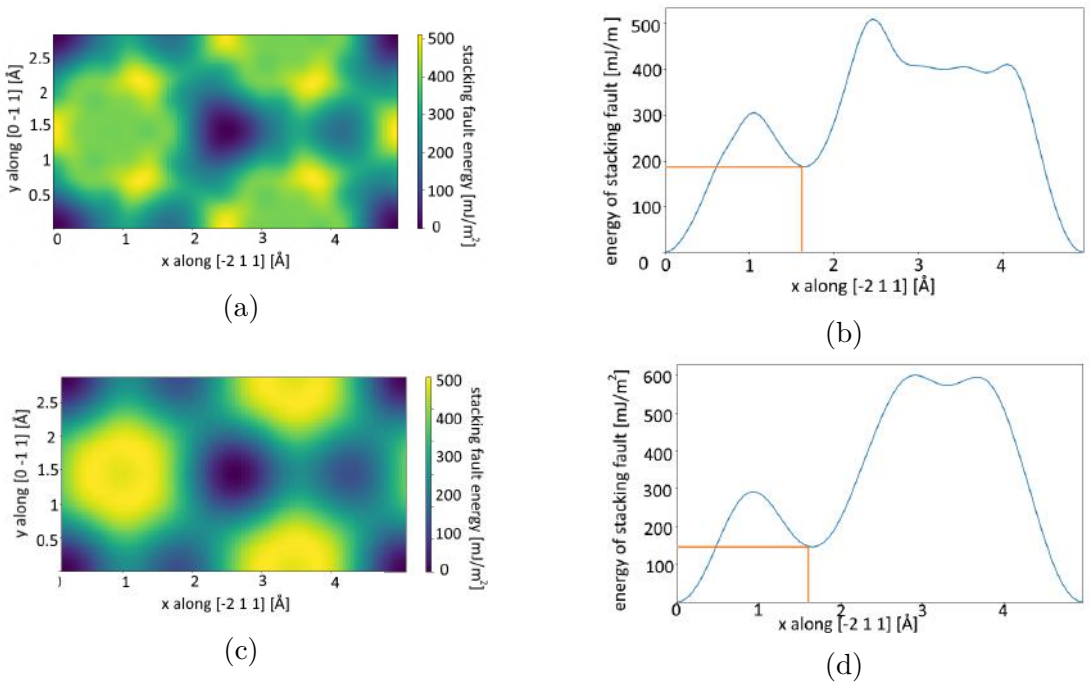

Figure 5.2: Comparison of predictions for stacking fault energy for MEAM potentials for (a), (b) pure Al and (c),(d) Al-Si-Mg-Cu-Fe. (a), (c) (111) plane, (b), (d) (111) plane in $[\bar{2}11]$ direction [129]

In FCC Al, the easiest glide plane is of type {111} and the stacking fault (SF) is formed by shifting one plane in the [112] direction by 1/6 of the vector length, which makes 1.6 Åfor Al lattice parameter. Stacking fault energy for this shift can be seen in fig. 5.2d and fig. 5.2b and makes 150 mJ/m^2 for Al-Si-Mg-Cu-Fe MEAM and 180 mJ/m^2 for Al MEAM. Experimental values reported for stacking fault energy in Al vary from 160 to 250 mJ/m^2 [130, 131].
The above listed values serve as guidelines for comparing potentials, however they can change for variations in calculation methods or simulation software. To obtain generalised stacking fault energies of the Al-Mg MEAM and to check the values taken from the potential implementations, a following simulation for computation of stacking fault was performed.
A box of 13.8x14x11.4 nm^3 was created and filled with Al atoms with FCC structure. The box was divided into two parts along {111} plane and one part was gradually shifted along [112] direction (fig. 5.3) in steps of fraction 1/120 of [112] unit lattice vector. The SF energies were computed by computing a total energy of the atoms in the system for each step, subtracting it from the energy of the unperturbed system and dividing the result of subtraction by an area of the fault plane.
The simulation was run for all three potentials and the results are plotted in fig. 5.4. The general shape of the curves remains as shown in fig. 5.2, the values of the energy for pure Al potential are significantly higher than the ones for both multielement potentials, while the values for Al-Mg MEAM are even slightly lower than the ones for Al-Si-Mg-Cu-Fe MEAM. The energies at local minimum are respectively 149, 139 and 187 mJ/m^2 for Al-Si-Mg-Cu-Fe, Al-Mg and Al MEAM respectively.

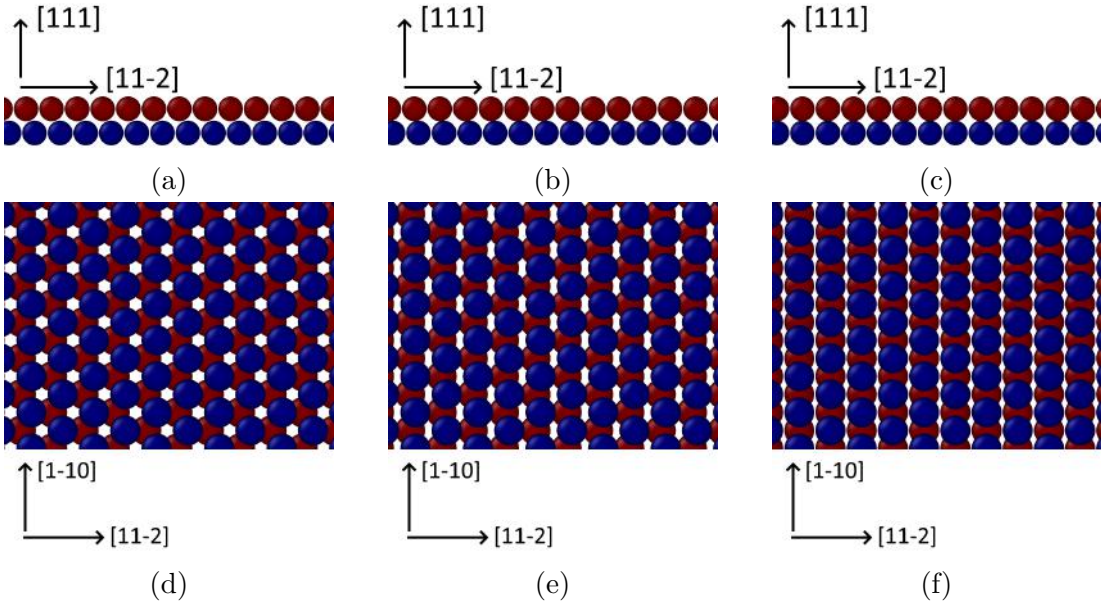

Figure 5.3: Visualization of motion of atoms in (111) plane [112] direction used in the calculation of generalised stacking fault energy. Different planes are distinguished by color.

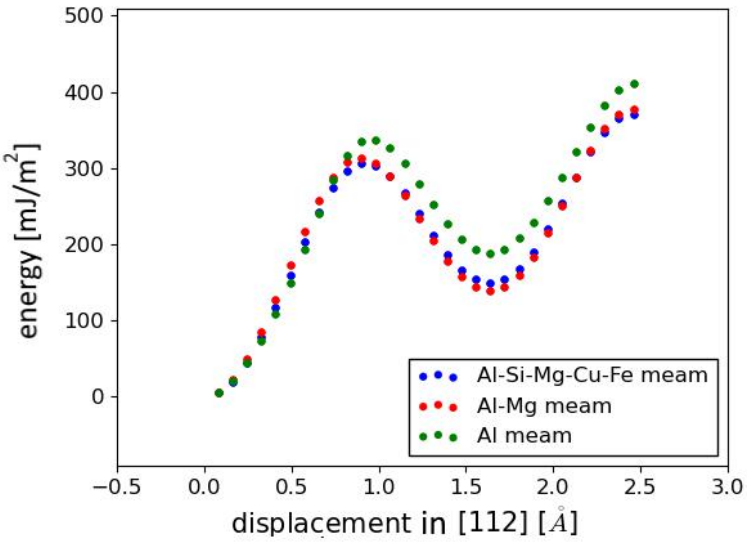

Figure 5.4: Generalised stacking fault energy for displacement in (111) plane in [112] direction.

5.2 Effect of potentials on simulated results

To study the role of the potential selection, a block of 20x20x20 nm^3 with orientation [110] in z, [100] in x and [112] in y direction with periodic boundary conditions along x and y axis and free surface perpendicular to z axis was created and filed with Al atoms with FCC structure. The block was deformed with respective use of all potentials in tension with tensile direction in y axis up to 20% strain with a strain rate of 2.10^9 s^{-1}.

The computed positions of atoms are visualised using Ovito software [123] along with their properties - crystal structure obtained from common neighbor analysis and presence of dislocations detected by dislocation analysis. Color coding used in all following visualisations is listed in fig. 5.5.

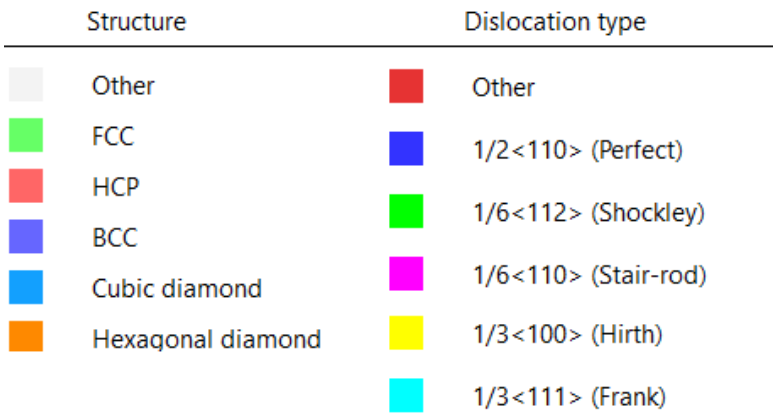

Figure 5.5: Color coding for representation of structure and dislocation types for images created by Open visualisation tool Ovito

The stress-strain curves (fig. 5.6) were obtained from the simulation by computing the stress tensor of individual atoms, summing the component in y direction and dividing it by initial sample volume and current strain (current y-length of the deformed box over the initial value). Several features are evident from the image.

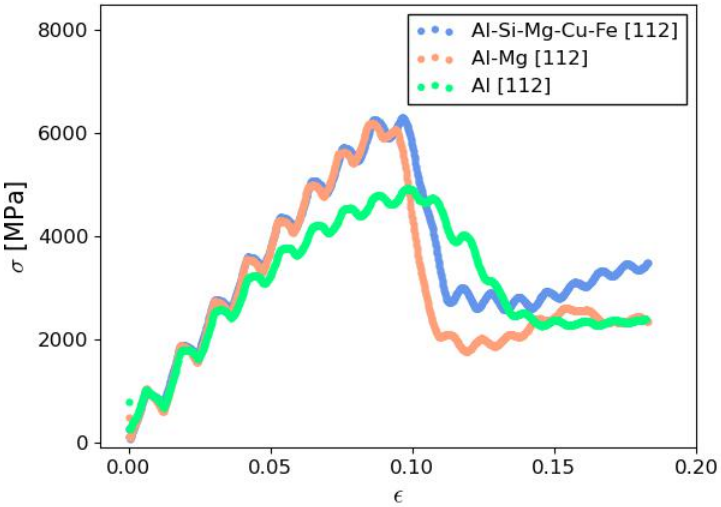

Figure 5.6: Comparison of stress-strain curves for MD of tensile deformation of Al single crystal using three different potentials

Repeated oscillations of stress as well as sudden drop in stress at around 10 % strain are common for all plotted functions. Rather compliant shape of the curves for both multi-element potentials is noticeable, whereby the stress drop in Al potential occurs slightly later and is considerably less steep than in other cases. When using a single element potential, the strength of the sample is considerably

lower than for multi-element ones. Disregarding oscillations, the slope of the curve gradually decreases before the drop in contrast to the unchanging slope character in the latter case.

Visualisations of the atom positions with application of common neighbor analysis and dislocation analysis were done to uncover the mechanisms under the computed stress-strain characteristics. Fig. 5.7 shows the results of the simulation with Al-Si-Mg-Cu-Fe MEAM at different strain values.

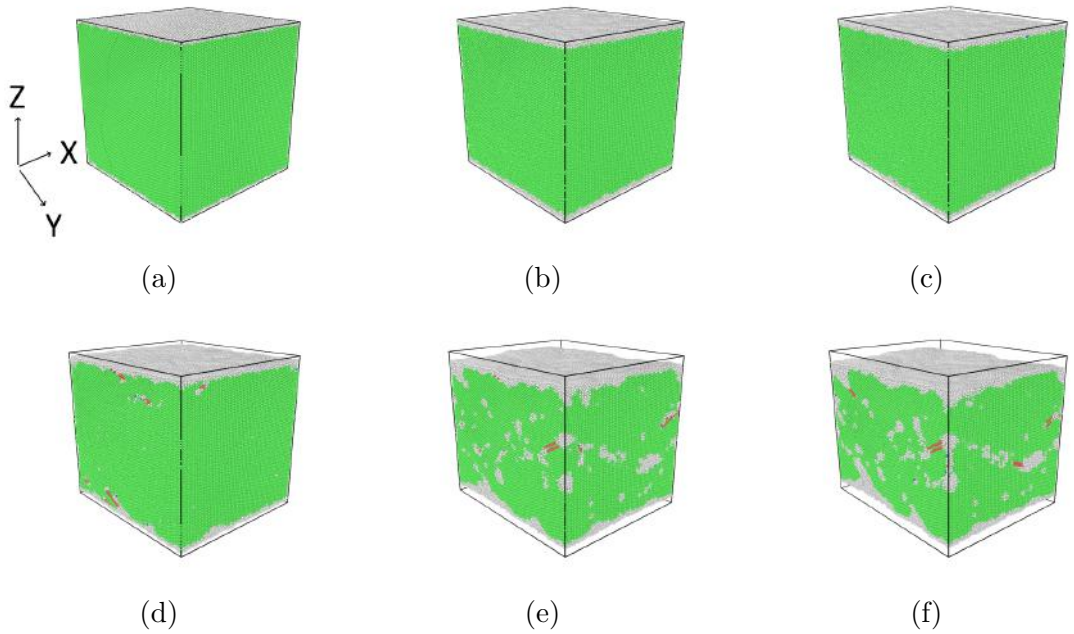

Figure 5.7: Tensile deformation of Al box, visualization with centrosymmetry parameter, color coding as in fig 5.5 a) 0%, b) 3.6%, c) 7.3%, d) 9.2%, e) 14.6%, f) 18.3%

The FCC structure becomes distorted at about 9% strain and regions of anomalous structure along with HCP stacking faults lying in {111} planes appear and gradually grow with increasing deformation. The already mentioned distortions originate at the free surface. The initially flat surface of the sample also becomes irregular making the thickness in different x,y positions uneven.
To pinpoint the stress value of the first dislocation nucleation, the dislocation analysis was performed and results with particles removed from the image are shown in fig. 5.8.
From this representation, it is evident that the dislocations indeed originate at both free surfaces and propagate to the center of the sample where they meet and interact. At lower strains, Shockley partial dislocations prevail (fig. 5.11a, 5.11b - green), at higher strain values they combine into perfect 1/2[110] ones (fig. 5.8e, 5.8f - blue). First dislocations appear at strains above 8%. They duplicate at 10% where the drop in the stress occurs in the stress-strain curve (fig. 5.6) and appear in the whole sample volume.
Removal of all but atoms with HCP surroundings creates images with clear presentation of SF. Comparison with the identical images of dislocation analysis (fig. 5.9) clearly shows that the areas of stacking fault are bound by the Shockley partial dislocations and move with their propagation, which is a common mechanism

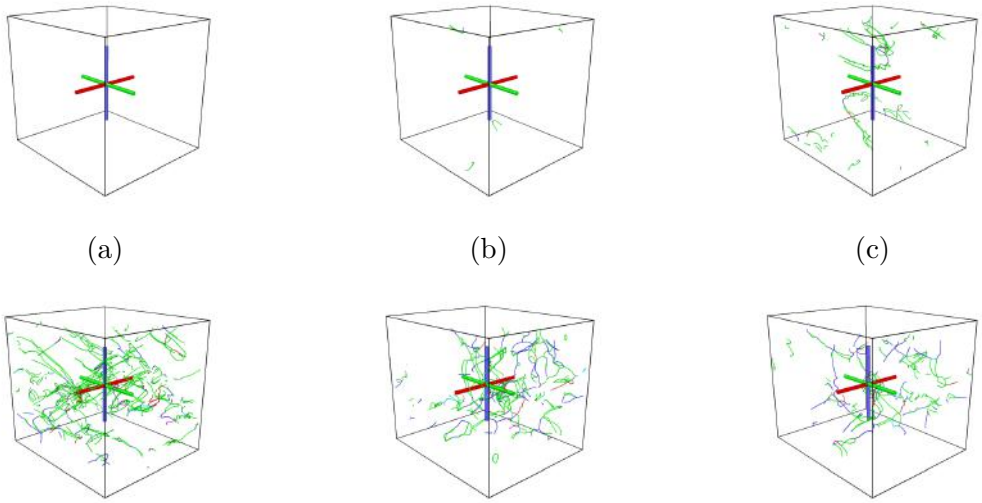

(a) (b) (c)

(d) (e) (f)

Figure 5.8: Tensile deformation of Al box for Al-Si-Mg-Cu-Fe MEAM, dislocation analysis, color coding as in fig 5.5 a) 5%, b) 8.2%, c) 9.2%, d) 10.1%, e) 14.6%, f) 18.3%

for the SF formation.

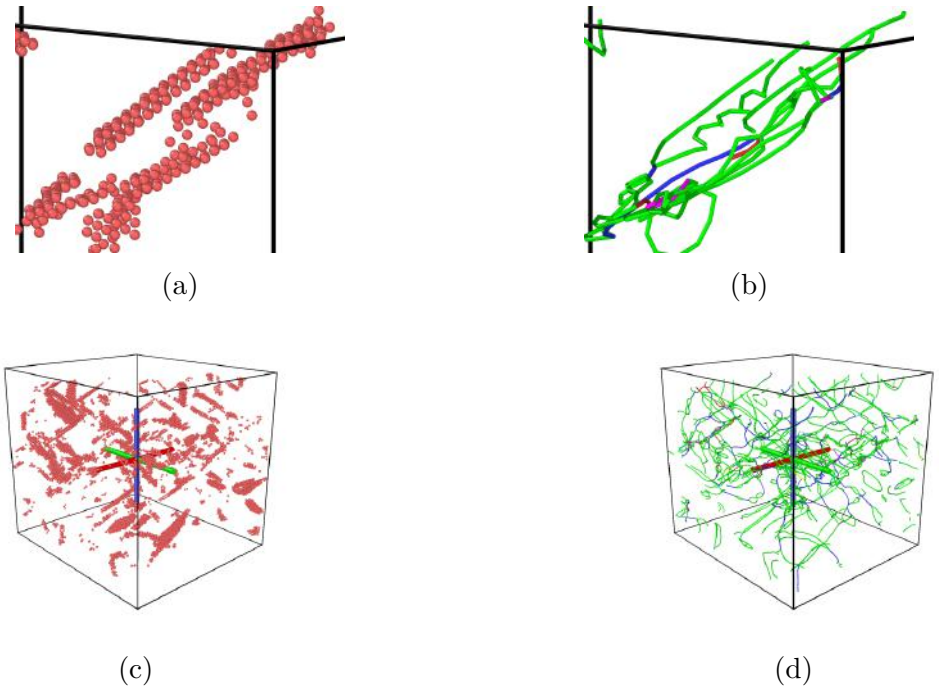

(a) (b)

(c) (d)

Figure 5.9: Comparison of dislocation analysis images with corresponding images of HCP planes a,b) detail 9.2% strain, b) 10.1% strain

Creation of stacking faults and distortion of sample surface were observed for all three used potentials dislocation motion. The HCP atom view for all potentials at three chosen strains between the beginning of SF formation and end of the deformation is shown in the fig. 5.10. The first appearance of HCP planes occurs in the case of Al MEAM at strains larger (above 9%) than for other two potentials,

that already have multiple continuous areas growing in the direction to the centre of the sample. However, by the strain value of 11% they (fig. 5.10h) start growing into large continuous planes with sizes reaching almost the dimension of the whole sample. Almost unchanged, they remain in their place and size until the end of the deformation (fig. 5.10i). On the other hand, the SF simulated with multi-element potentials form much smaller mobile areas which reach their maximum volume fraction at strains around 10% and gradually decrease towards the end of the simulation as partial dislocations annihilate at the opposite surfaces.
The delayed nucleation of first dislocations and HCP planes with use of pure Al potential is compliant with the delay of stress drop in stress-strain curves (fig. 5.6). However, the lower strength of the material in regard to other two potentials and the larger size of stacking faults in the case of Al potential seem contradictory to higher value of energy of stacking fault formation for this potential. For this reason, the SF planes were explored in detail.

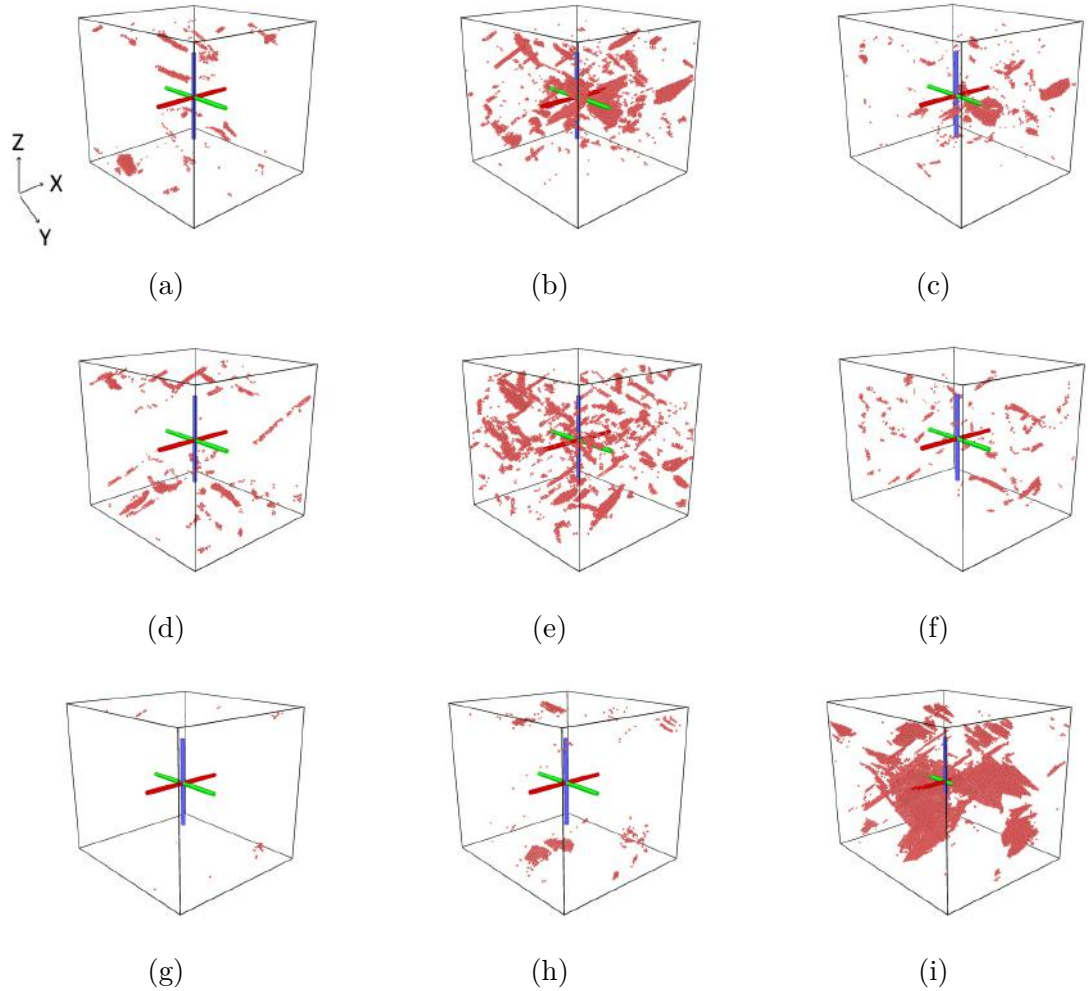

Figure 5.10: The comparison of deformation for different potentials, only the atoms in HCP positions are shown: a-c) Al-Si-Mg-Cu-Fe MEAM, d-f) Al-Mg MEAM, g-i) Al MEAM, strains: a,d,g) 9.2%, b,e,h) 11%, c,f,i) 18.3%.

A detail of HCP planes for Al-Si-Mg-Cu-Fe MEAM and Al MEAM is shown in fig. 5.8. Two adjacent planes of HCP marking the presence of a standard

intrinsic or extrinsic stacking fault form the plane for the former, whereas in the latter only a single HCP plane cuts through the FCC lattice. Such an occurrence typically indicates a micro-twin boundary and may be produced by a consecutive propagation of the Shockley partials in the neighboring planes.
In this manner, two HCP planes are created, receding by one atomic plane with propagation of each dislocation. However, no such process was observed in the simulation course and no pairs of HCP planes were visible either. Rather a single plane sprouted from the free surface and extended through the sample. This rather curious behaviour can be explained by visualisation of not only HCP, but also the particles in unidentified lattice structures. Such images for potentials Al-Mg MEAM and Al MEAM at different strains are shown in fig. 5.12.

(a) (b)

Figure 5.11: Comparison of HCP atom planes in a) Al-Si-Mg-Cu-Fe MEAM, b) Al MEAM.

The images show a different behaviour of atoms in no particular structure (grey) for both potentials. In the first case, the small SF areas bounded by the Shockley partial dislocations are surrounded by grey atoms. Aside from that, only random single atoms in the whole volume and a layer of grey atoms at the free surface appear in the first stages of SF formation and propagation. These areas extend With increasing strain, yet no separate extensive volumes of grey atoms are formed (fig. 5.12a, 5.12b, 5.12c). In the second case, a large humps of distorted lattice structure form at the free surfaces and extend in the direction parallel to the sample height. HCP single layer planes adjacent to these areas are formed when these areas take up a relatively large fraction of the sample volume (fig. 5.12d, 5.12e, 5.12f). Therefore, the lower strength corresponding to pure potential results from a different deformation mechanism. Rather hardly explainable single planes of atoms in HCP lattice surrounded by FCC structure (twin boundaries) are not formed nor is it a standard stacking fault with high formation energy.
The origin of multiple small steps appearing in both curves before they reach yielding point could not be unambiguously assigned to any process observed in the visualisation and is most likely related either to dislocation processes on the free surface where the periodicity of crystal structure is violated and cannot be detected by dislocation analysis or to formation of point lattice defects and other lattice irregularities in the volume of the sample.

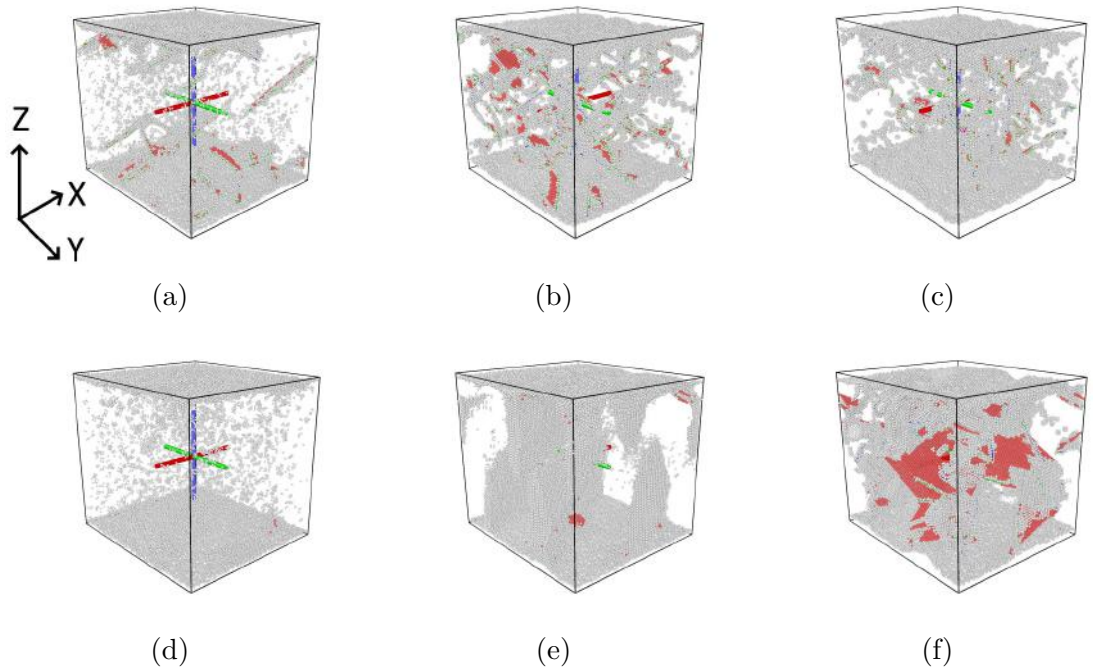

Figure 5.12: Visualisation of all but FCC atoms in the deformation for two different potentials: a-c) Al-Mg MEAM, d-f) Al MEAM, strains: a,d) 9.2%, b,e) 11%, c,f) 14.6%

5.3 Effect of crystal orientation

With all other simulation parameters unchanged, the lattice inside the simulation box was rotated around z axis so that respectively [100], [110] and [111] directions become parallel to the axis of deformation. The stress-strain curves for multi and single element potentials are shown in fig. 5.13. The comparison of potentials for different axis directions is shown in fig. 5.14 since the results quite vary depending on the used potential.

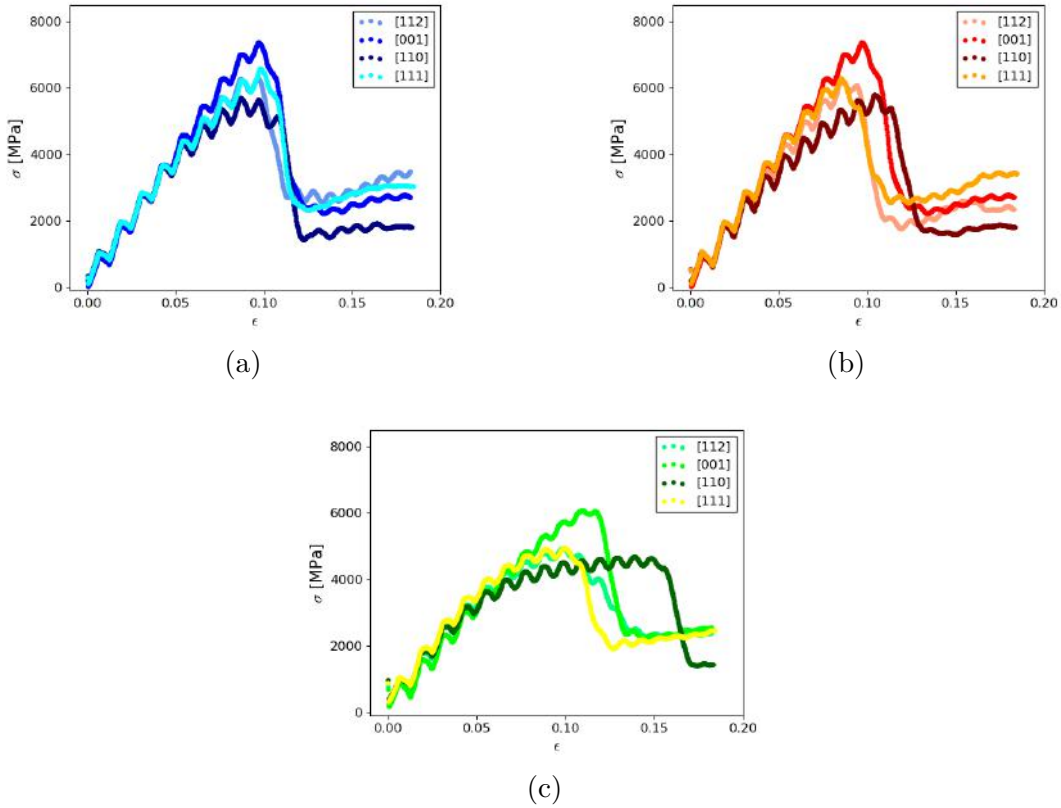

(a) (b)

(c)

Figure 5.13: Stress-strain curves for deformation of Al single crystal at different orientations: a) Al-Si-Mg-Cu-Fe MEAM, b) Al-Mg MEAM, c) Al MEAM.

Generally, the strength of Al-Si-Mg-Cu-Fe MEAM is the highest for all simulated orientations while the strength of Al MEAM is the lowest. This effect in [112] direction was already addressed in the previous section (fig. 5.6) and seems to root from major distortion of a lattice structure in contrast to simple propagation of dislocations and formation of stacking fault. Direction [110] has the lowest strength for all potentials, [001] the highest, strength of [111] and [112] is about the same. For Al MEAM, the slope of the curve decreases before the stress drop in all orientations. All the material strengths range between 4 and 8 GPa.
A visualisation of computed atom locations during the deformation was once again performed to correlate the structural changes to the changes in the shape of stress-strain curves. Images of HCP atoms for Al-Si-Mg-Cu-Fe MEAM and different lattice orientations parallel to tensile axis at strain 14.5% are shown in fig. 5.15. Similar results were observed in Al-Mg MEAM and Al MEAM, yet in the latter, formation of all HCP atom planes was preceded by a formation

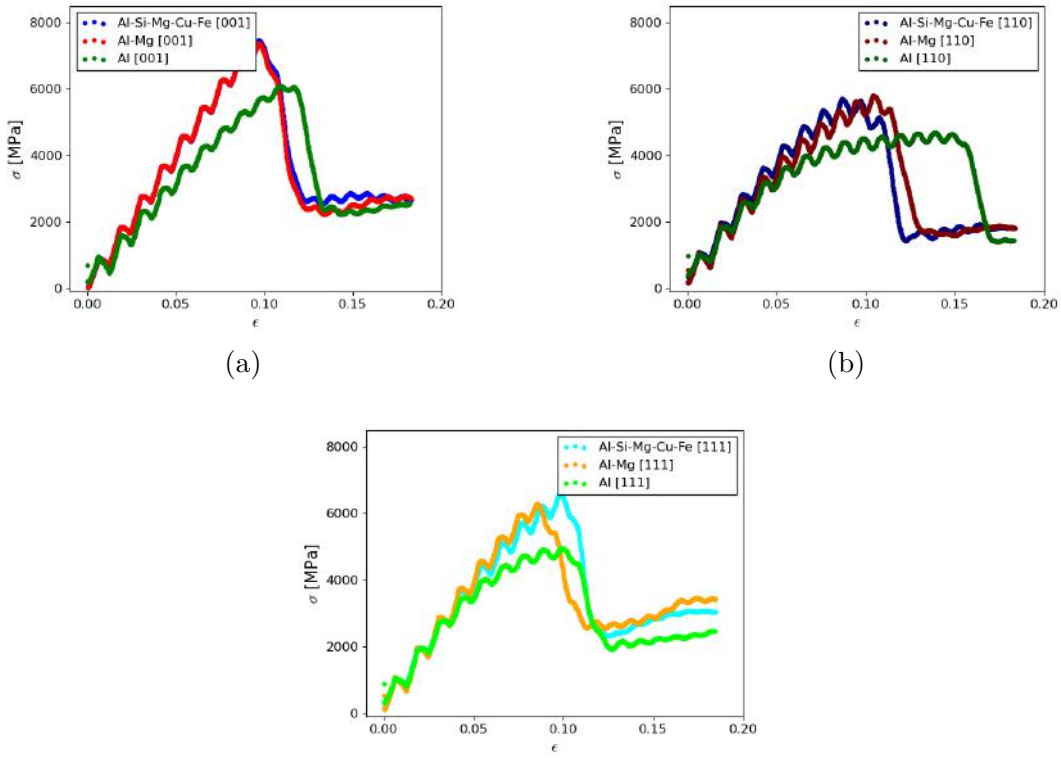

Figure 5.14: Comparison of stress strain curves for different potentials, tension axis parallel to a) [001], b) [110], c) [111].

of thick volumes of atoms in undefined lattice structure: in the areas where the HCP atom planes appeared at higher strains.
For tensile axis in [110] orientation, large areas of SF crossing the entire dimension of the deformation box were formed in two different directions and as the deformation proceeded, the HCP planes separated and created boundaries for microtwins. In [111] orientation, less extensive SF planes formed in three different directions, while in [001] four different directions of even smaller areas of h.c.p. planes were observed.

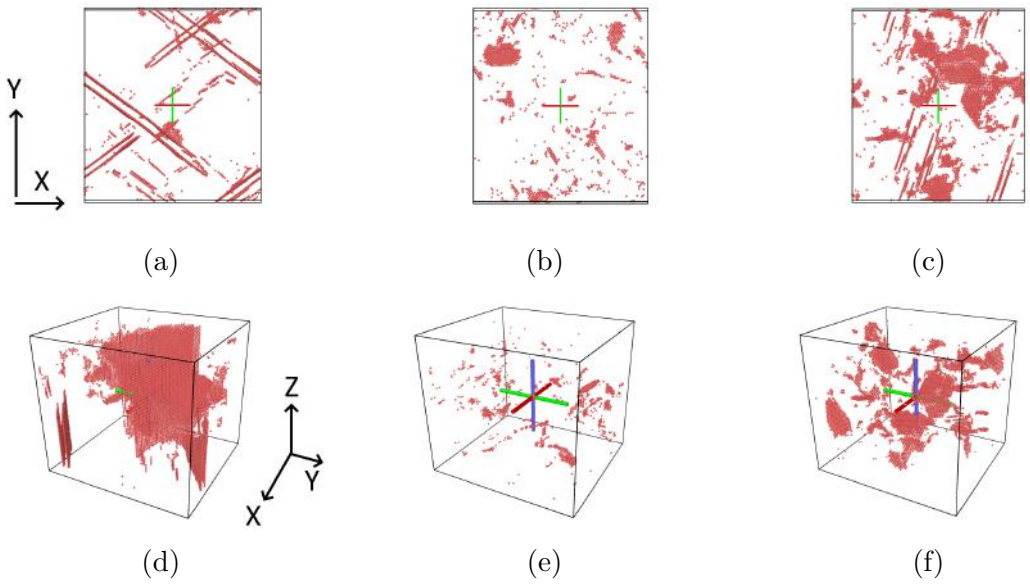

Figure 5.15: Images of HCP atomic planes at 14.5% strain for Al-Si-Mg-Cu-Fe MEAM, orientation of tensile axis: a,d) [110] b,e) [001] c,f) [111].

5.4 Effect of film thickness

Another parameter crucial in the investigation of thin films is, unsurprisingly, their thickness. Markedly in MD simulations, thickness is an important part in overall volume of the sample which has again correlation to the total computation time. The adequate thickness is frequently impossible to reach at reasonable computation time and strain rate. Therefore, studies of thin films are regularly restricted to a scale of nm [132]. To observe the relationship between the film thickness and its deformation mechanisms, samples of thicknesses between 5 and 50 nm were deformed using pure Al MEAM. Four blocks of dimensions 20x20xZ nm^3 with Z equal respectively 5, 10, 20 and 50 nm with orientation [110] parallel to z and [112] parallel to x were simulated and deformed with the parameters identical with the simulations described above. Stress-strain curves for all thicknesses are shown in fig. 5.16. The first trend arising from the plot is a gradual increase of the material strength and elasticity proportional to the sample thickness.

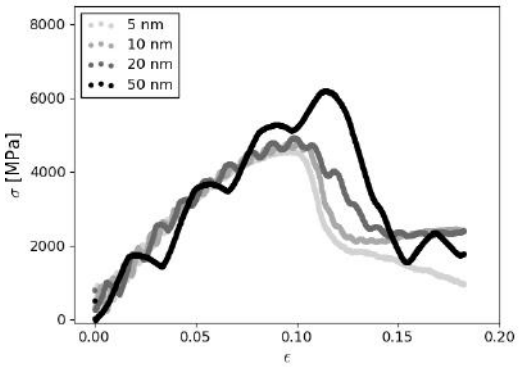

Figure 5.16: Stress strain curves of films with different thickness.

In the thinnest 5 nm sample, a hole forms (fig. 5.17) at the end of the deformation. The phenomenon is also reflected in the stress-strain curve, because the stress gradually decreases after the rapid drop in the contrary to thicker samples. Thicker samples remained compact, even thought considerably rumpled with irregular thickness and surface (fig. 5.18).

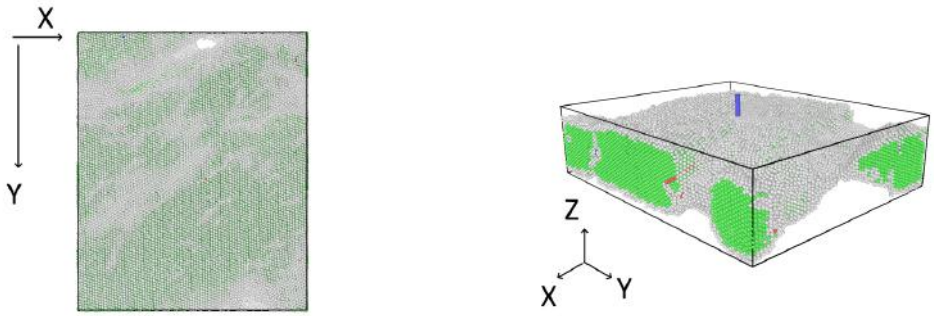

(a) (b)

Figure 5.17: Formation of a hole in 5 nm thick sample at 18.4% strain.

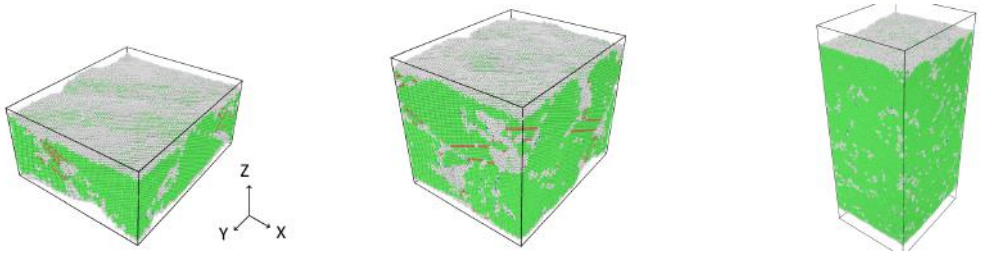

(a) (b) (c)

Figure 5.18: Irregular surface in a) 10 nm, b) 20 nm, c) 50 nm thick sample at 18.4% strain.

Similarly to previous results, the sudden drop in the stress values at around 15% strain corresponds to the onset of the formation of dislocations and adjacent stacking faults. The dislocations originate from free surfaces and gradually advance to the central area of the sample, which is notably evident from the 50 nm thick sample, where a longer time (larger strain) is necessary for dislocations formed at opposite free surfaces to meet in the center of the crystal. The images of only HCP atoms are shown in fig 5.19a, 5.19b, 5.19c, 5.19d). An increase of the area of coherent HCP planes can be observed as the thickness decreases. However, as showed in paragraph 5.4, not all HCP planes represent real SF but rather a single layer of HCP atoms surrounded by a volume of grey atoms of ambiguous lattice structure (fig. 5.19e, 5.19f, 5.19g, 5.19h).

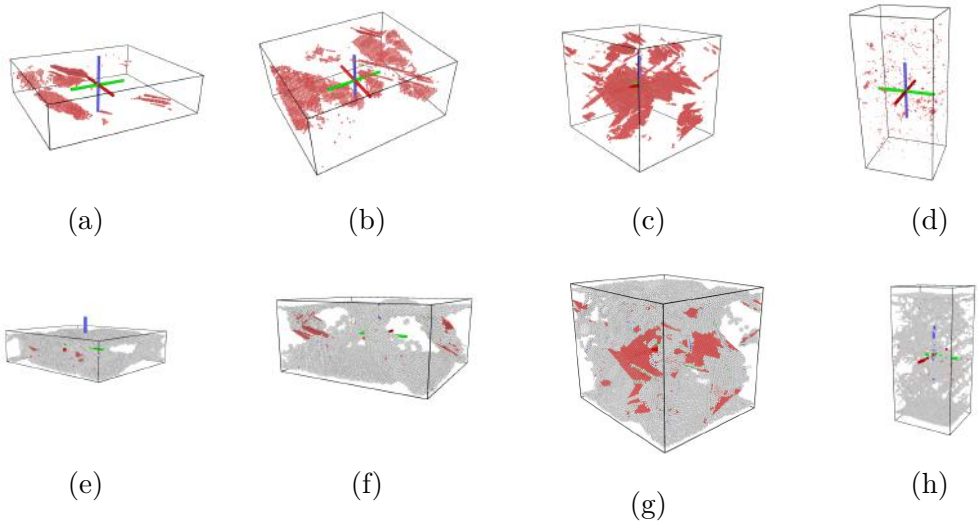

(a) (b) (c) (d)

(e) (f) (g) (h)

Figure 5.19: Visualisation of atoms in a-d) HCP, e-h) HCP and other unidentified structure for film thickness a,e) 5 nm, b,f) 10 nm, c,g) 20 nm, d,h) 50 nm at strain 14.4%.

5.5 Effect of strain rate

In order to explore the effects of strain rate on computation results, 18x12x8 nm^3 large block of Al was created with periodic boundary condition in z direction. The block was deformed in both tension and compression with deformation axis

parallel to z direction, The stress-strain curves obtained from deformation simulations at different strain rates are shown in fig. 5.20. Increase of the yield stress occurs for both compression and tensile deformations with increasing strain rate. The slope of the curve and deformation mechanisms remains unchanged for strain rates below 10^{10} s^{-1}. At strain rate of 4.10^{10} s^{-1}, a substantial degradation of original lattice structure was observed during the deformation with FCC structure reorganizing into BCC one in the case of compression experiment, and entirely losing its order in the case of tension. With the distortion of periodic structure, dislocation activity was no longer detected during the tensile deformation. A much larger block of the single crystal with dimensions 63x44x51 nm^3 with periodic boundary conditions in x,y and orientation [110] parallel with z direction was deformed at strain rate 4.10^{10} s^{-1} for both potentials. Even thought the majority of simulation parameters were different, a distortion of periodic structure with lack of dislocation activity was also observed. Stress-strain function for this simulation is shown in fig. 5.21. For this reason, all the following simulations were performed at strain rates lower than 10^{10} s^{-1}.

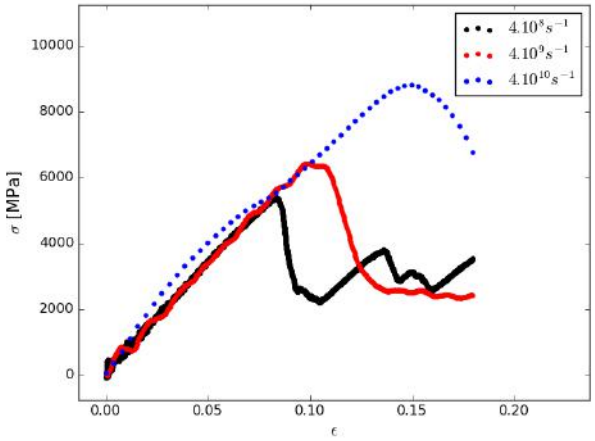

(a)

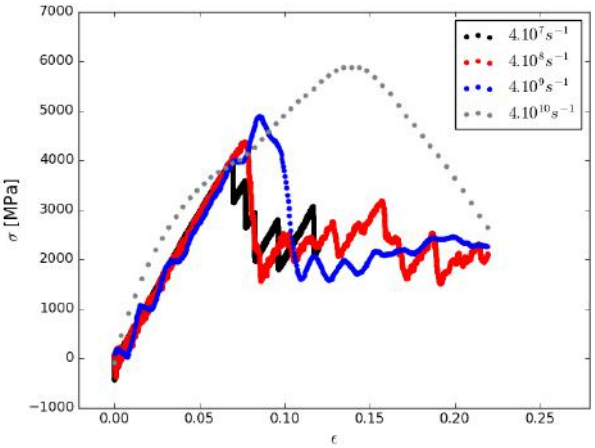

(b)

Figure 5.20: Stress-strain curves of Al single crystal deformed with different strain rates (a) tension, (b) compression.

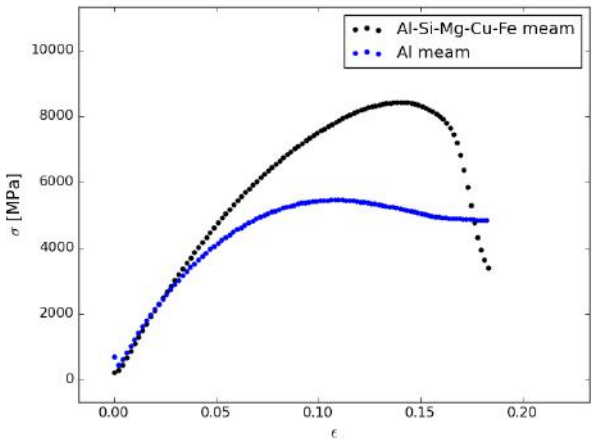

Figure 5.21: Stress-strain curves of a 50 nm thick Al single crystal deformed at strain rate 2.10^{10} s^{-1} oriented with [110] parallel to z axis simuated with two different potentials.

5.6 Polycrystal tensile deformation

In order to further approach the experimental conditions, a textured polycrystal film was created. Block 20x20x20 nm^3 large with 4 hexagonal grains (fig. 5.22) was created in Atomsk. A lattice nucleus oriented [110] in z direction, [001] in y and [110] in x was rotated around z axis by following angles: A: 54°, B: -77°, C: 130°, D: 126° (fig. 5.22c). Therefore, in grain A, the orientation [111] is close to the direction of tensile axis, grain B is rotated 13° from the direction [110], grains C and D have very close orientations with a high index direction parallel to y. Periodic boundary conditions were applied in x and y direction and the sample was deformed in tension along y axis with strain rate $2{\cdot}10^9$ s^{-1}. The deformation was carried out using multielement Al-Si-Mg-Cu-Fe MEAM and single Al MEAM potentials. Fig. 5.23 and 5.24 show examples of the microstructure evolution simulated with both potentials. Results of a dislocation analysis of Al MEAM potential are shown if fig. 5.25 and 5.26.
Simulation using of Al-Si-Mg-Cu-Fe MEAM resulted in an expansion of grain boundaries perpendicular to the deformation axis (fig. 5.23d, 5.23e, 5.23f). The expansion started at strain values around 7% and gradually proceeds so that at strains above 10%, the grain structure became distorted. A small hole was formed at the boundary between grains marked D and A, but it did not expand or propagate. Stacking faults form in corners of the grain marked as B. With increasing deformation, they disappear in the expanding area of the adjacent grain boundary.

Rather than a grain boundary expansion, a rupture of the material along the same grain boundaries was observed in the case of the Al MEAM potential (fig. 5.24d, 5.24e, 5.24f). A volume of grey atoms in undefined structure in a form of a thin bent line, indicating a presence of a dislocation, was ejected from a grain boundary in the grain D at around 3% strain (fig. 5.24a - red circle, marked as 1), crossed the grain and disappeared in the opposite boundary (fig. 5.24b, 5.24c). The first signs of the material rupture were observed at strain values above 10%

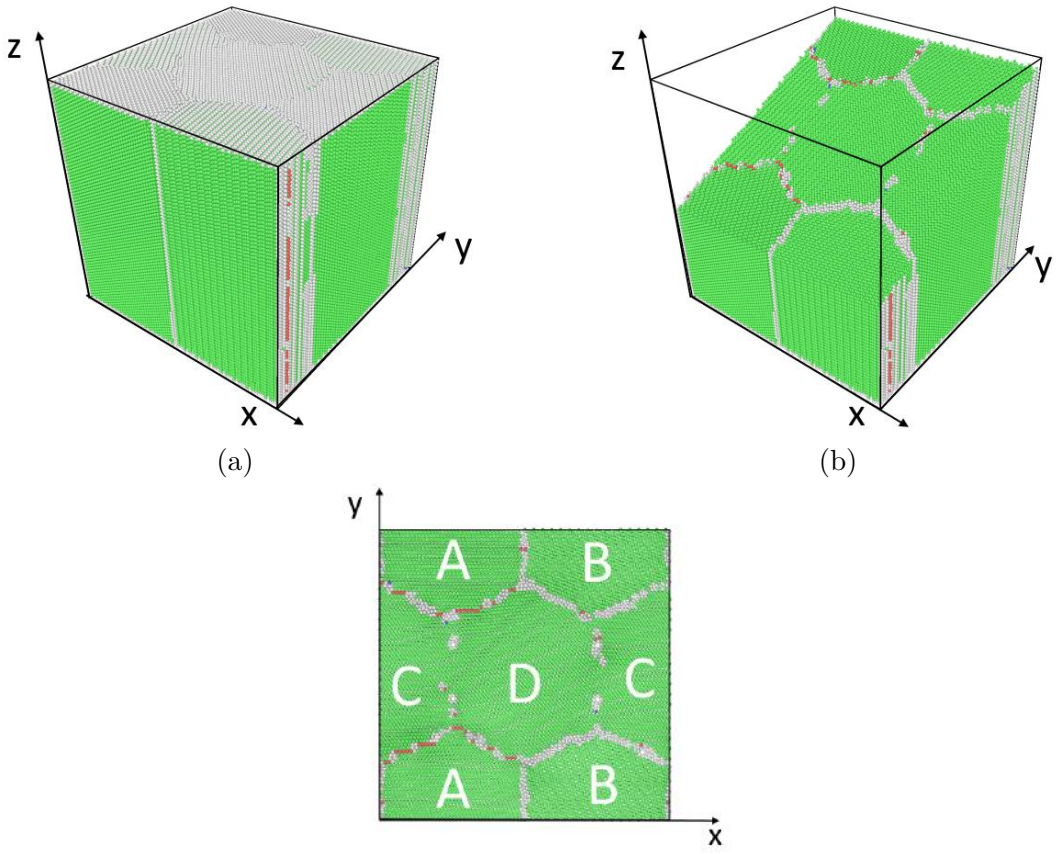

Figure 5.22: A block of Al polycrystal created in Atomsk before deformation: (a) full block, (b) block sliced in y/z direction so that GB are visible, (c) constant z slice with labeled grains.

(fig. 5.24e). Two single atomic layers of HCP planes marking the boundaries of a microtwin were formed right after the first signs of separation of the grains B and C (fig. 5.24e - blue circle, marked as 4) and they gradually propagate in the direction of the grain boundary while approaching each other and disappear at higher strains (fig. 5.24f). Similarly to the deformations of a single crystal with this potential, a distortion of a large volume of atoms from their lattice structure preceded the formation of microtwins in grain B. No significant lattice distortion appeared in remaining grains. After the formation of the hole, two thin long lines of SF surrounded by a layer of undefined lattice structure parallel to the z direction formed in grain C (fig. 5.24e - red circle, marked as 2 and 3). With increasing strain, one of them slowly moved (fig. 5.24f) across the grain and disappeared at the grain boundary with grain D.
Dislocation analysis of the computed results showed constant motion of dislocations inside the grain boundaries for both potentials. No dislocations were observed in simulation using Al-Si-Mg-Cu-Fe MEAM potential. A single perfect [110] dislocation emitted from a grain boundary at a strain $\approx 3\%$ (fig. 5.25 - marked by pink arrows) observed when the Al MEAM potential was used corresponds to the distorted lattice line observed in common neighbor analysis visualisation (fig. 5.24a, 5.24b, 5.24c). The dislocation crosses grain D and annihilates

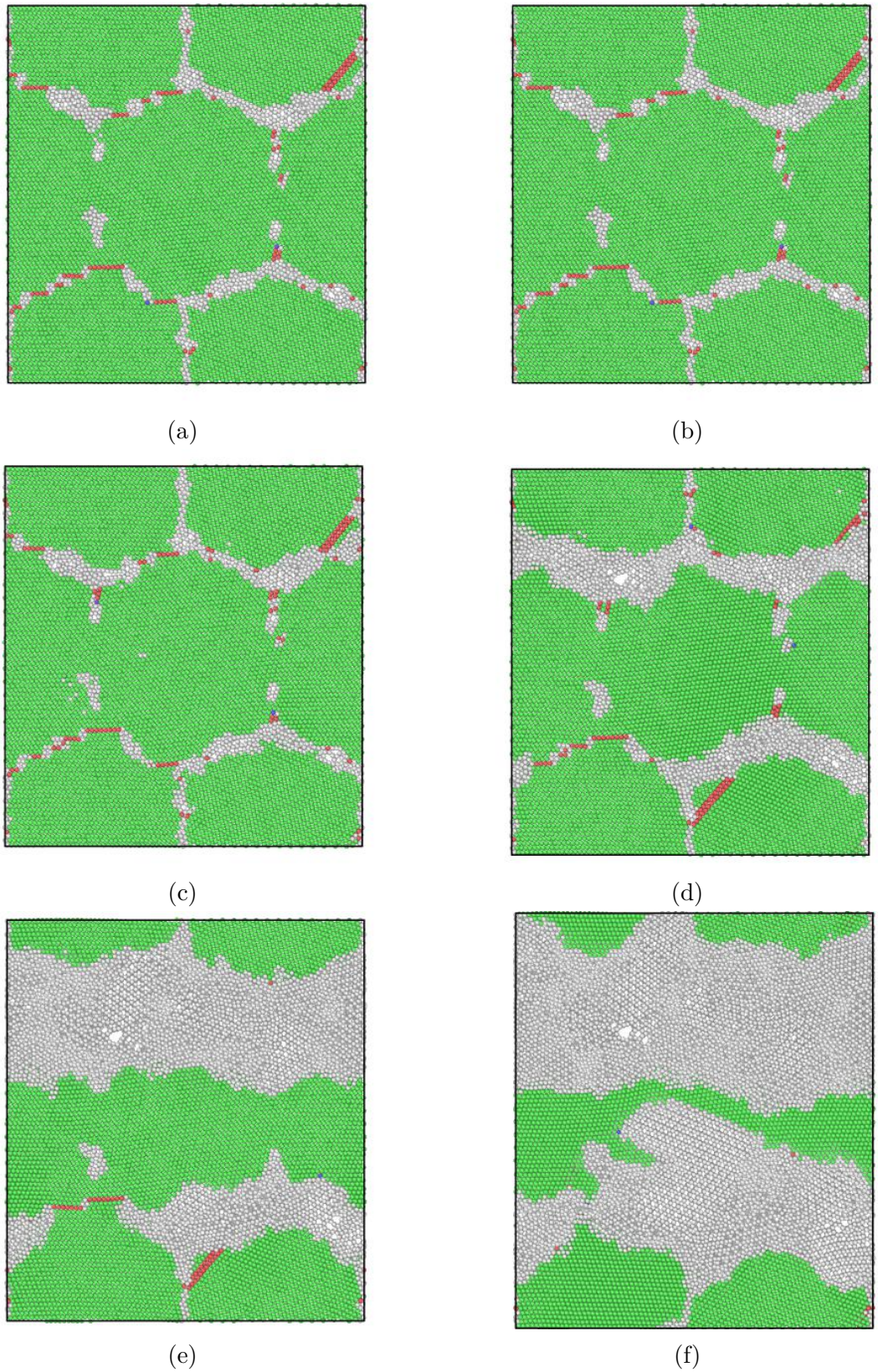

Figure 5.23: Deformation of Al polycrystal using Al-Si-Mg-Cu-Fe MEAM, strain: a) 3.6%, b) 5%, c) 5.7%, (d) 7.2%, (e) 10.8%, (f) 14.4%. Color coding of atoms and dislocations as listed in 5.5.

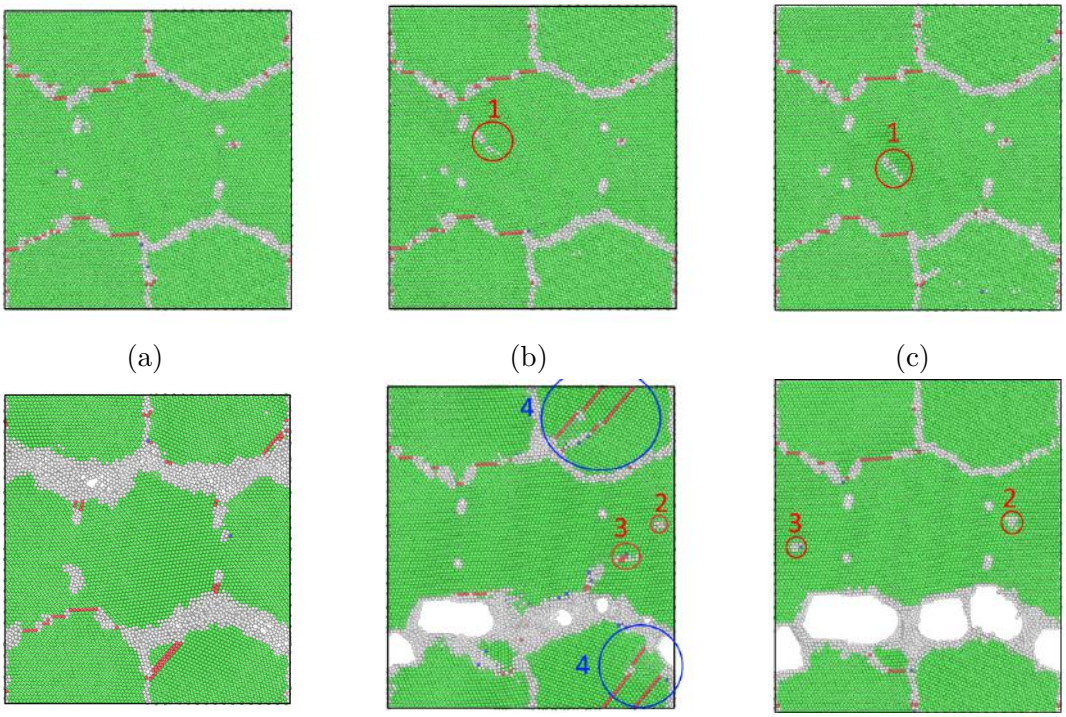

Figure 5.24: Deformation of Al polycrystal using Al MEAM, strain: a) 3.6%, b) 5%, c) 5.7%, (d) 7.2%, (e) 10.8%, (f) 14.4%. Color coding of atoms and dislocations as listed in 5.5.

in the opposite grain boundary.
Fig. 5.27 shows the corresponding stress-strain curves. The rapid decrease of stress matches the strain values at which the grain boundary expansion started in the case of Al-Si-Mg-Cu-Fe MEAM and analogously the beginning of film rupture for Al MEAM is linked to drop of stress to zero. Similarly to the deformation of single crystals (fig. 5.6), no visible origin of oscillations on stress-strain curves was observed.

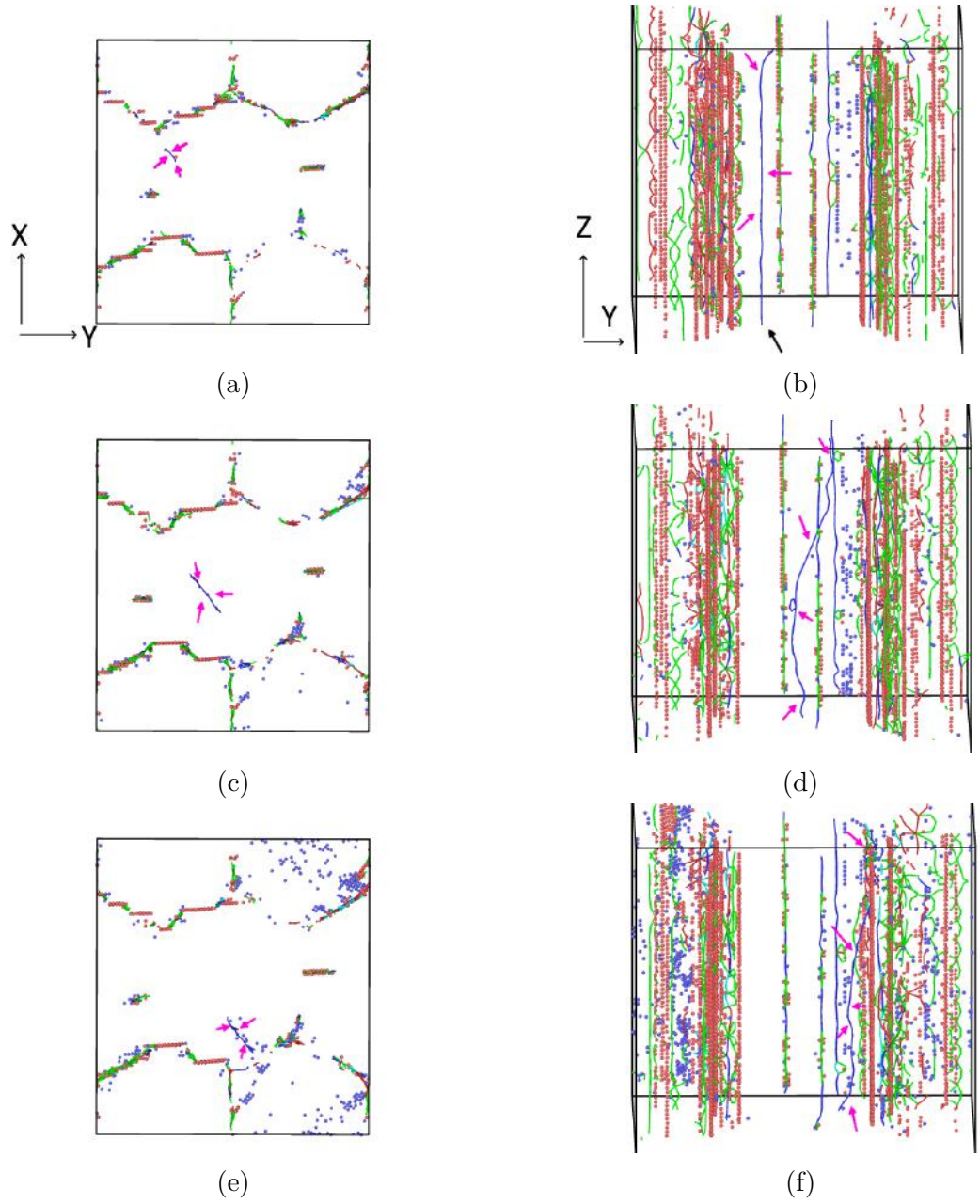

(a) (b)

(c) (d)

(e) (f)

Figure 5.25: Dislocation analysis of deformed Al polycrystal (a), (c), (e) - constant z view, (b), (d), (f) - constant x view. (a), (b) $\epsilon = 3.4\%$, (c), (d) $\epsilon = 5.9\%$, (e), (f) $\epsilon = 7.2\%$, Color coding of dislocations as listed in 5.5.

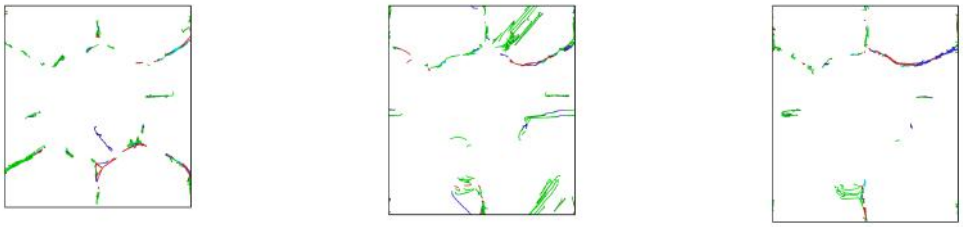

(a) (b) (c)

Figure 5.26: Dislocation analysis of deformed Al polycrystal for higher strains: (a) 7.2%, (b) 10.8%, (c) 14.4%.

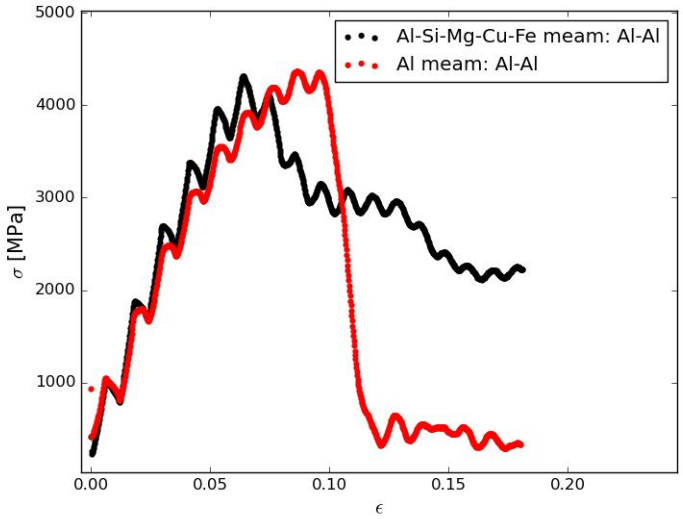

Figure 5.27: Stress-strain curves for MD of tensile deformation of Al polycrystal simulated with two different potentials.

5.7 Effect of dimensions

A susceptibility of the simulation to the dimensions of the sample was tested by changing the thickness of the simulated film and by increasing the grain size. The [110] textured polycrystal from fig. 5.22 with a thickness increased to 50 nm in the z direction was generated and deformed under the same conditions as the sample in paragraph 5.6. The comparison of strain-stress curves is shown in fig. 5.28. A minor shift of the maximum to higher values of stress and strain appears, otherwise no significant changes in material properties and deformation mechanisms were formed and the whole process could be described by the same visualisations as in the case of the thinner film presented in the previous paragraph.

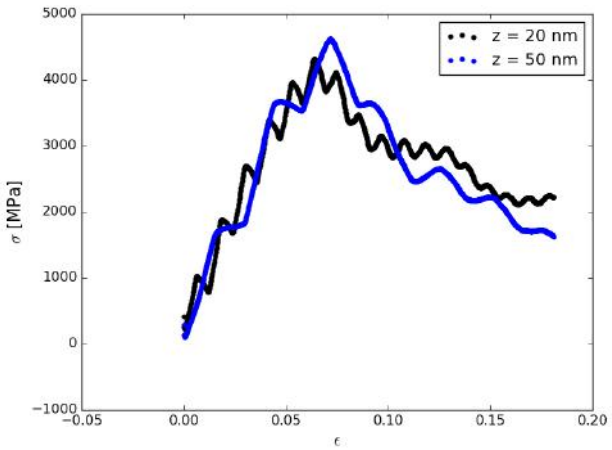

Figure 5.28: Influence of thickness on stress-strain curves of Al polycrystal.

The original 20x20x20 nm^3 block was taken and this time, the x and y dimensions were increased to 40 nm, without any change of the geometry and orientation of grains. Only the grain diameter was increased to 20 nm. The sample was again deformed under the same conditions. Fig. 5.29 shows stress-strain curves

calculated with two potentials. They show that increase of grain size to 20 nm does not change the properties of the simulated polycrystal regardless of the used potential. Visualisation of the simulation shows several dislocations crossing the interior of grains, but they were immediately annihilated in the opposite grain boundary and did not interact with each other.

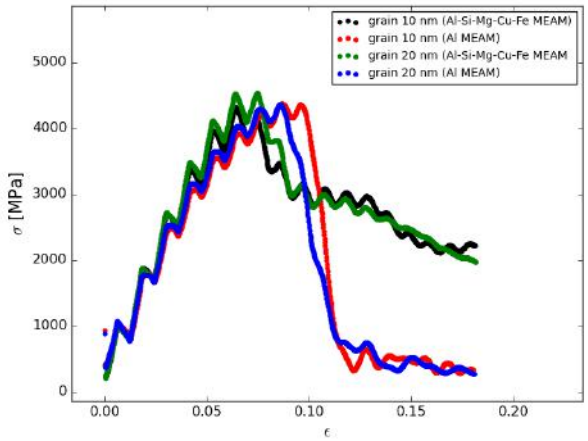

Figure 5.29: Influence of grain size on stress-strain curves of a 20 nm thick polycrystal deformed in tension.

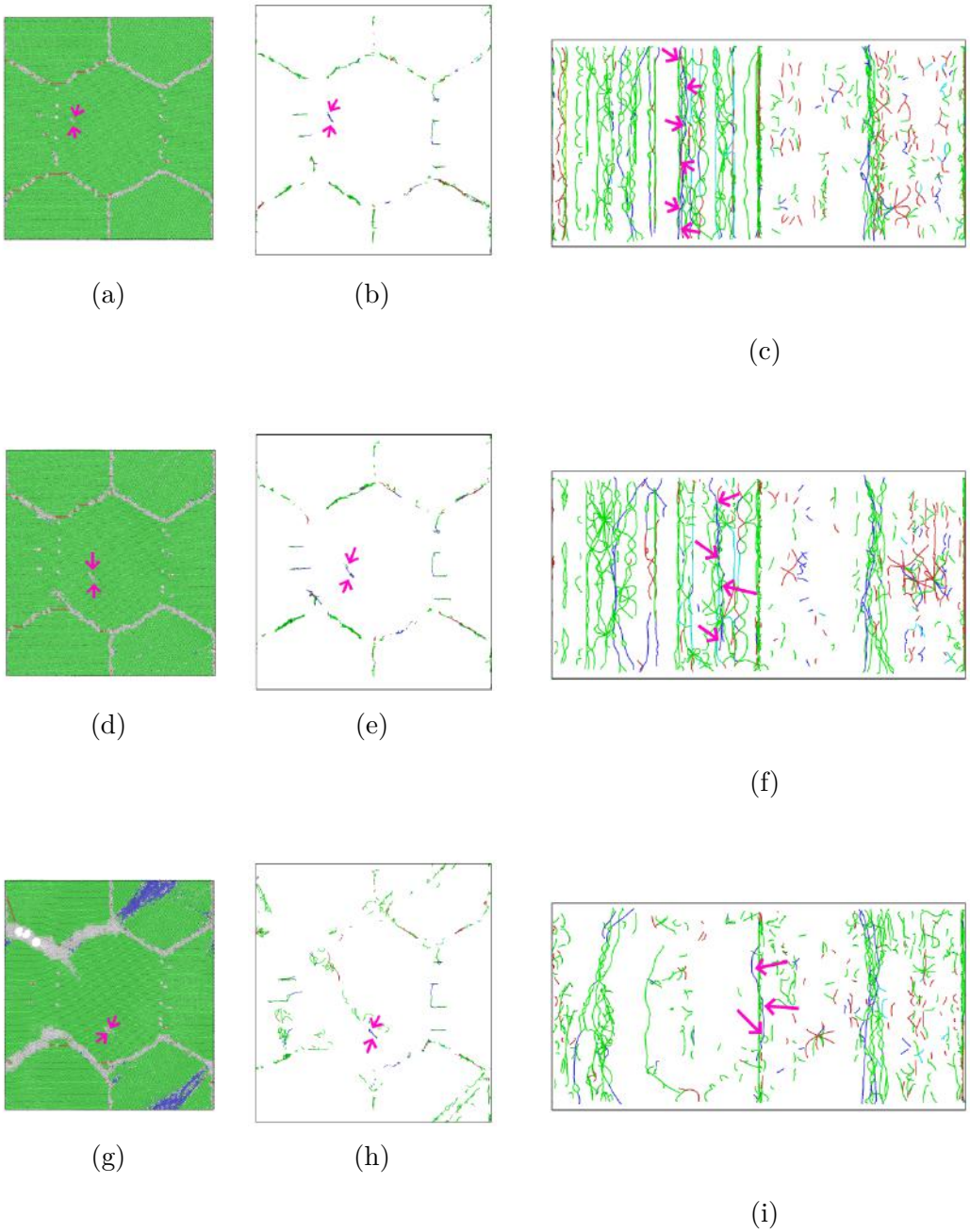

Figure 5.30: Deformation of the polycrystal with a grain size of 20 nm: a,d,g) common neighbor analysis b,e,h) dislocation analysis, constant z view c,f,i) dislocation analysis, constant y view a,b,c) 5.4%, d,e,f) 7.2%, g,h,i) 9.2%.

5.8 Addition of Mg

Finally, the effect of addition of Mg to the polycrystal structure was examined. A 10.7x93x15 nm^3 large block with regular hexagonal grains of random orientation was generated in Atomsk (fig. 5.31a). Again, periodic boundary conditions were applied in x and y directions and the polycrystal was deformed in tension with axis parallel to the y direction. The same block of grains was adjusted by substituting 3 wt.% of randomly distributed Al atoms for Mg (fig. 5.31b). Finally, instead of the random distribution, only atoms in the vicinity of grain boundaries were selected, and part of them randomly changed to Mg (fig. 5.31c) so that the average weight concentration of the whole block remains 3%. These configurations were chosen to document the effect of grain boundary segregation on the polycrystal sample of reduced size. All the blocks were deformed in the same manner as samples in the previous two sections and the resulting stress-strain curves are shown in fig. 5.32. An addition of 3wt.%Mg into the Al polycrystal, whether randomly distributed or segregated on grain boundaries, does not seemingly change mechanical properties of the sample. Higher values of stress observed above $\epsilon \approx 10\%$ in the sample with Mg atoms segregated at grain boundaries indicate a positive role of Mg on their stability. This hypothesis is also supported by visualisations (Fig. 5.33) showing disturbed zones near grain boundaries at different strain levels. The width of the disturbed zone increases with increasing strain independently on the distribution and concentration of Mg. However, higher concentration of Mg atoms on grain boundaries significantly reduces their width, so that at the same strain level the resulting stress is superior in the material with Mg grain-boundary segregation (Fig. 5.32).

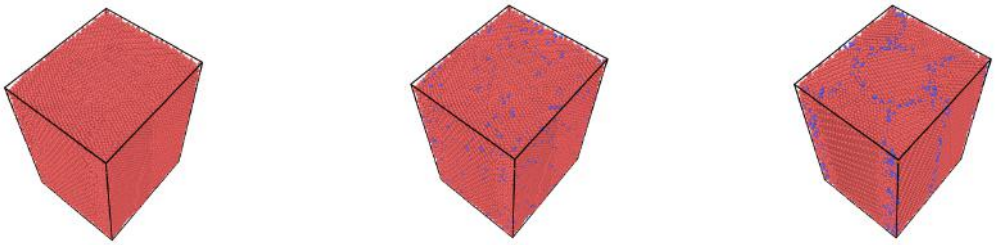

(a) (b) (c)

Figure 5.31: Polycrystal FCC block with randomly oriented hexagonal grains (a) pure Al, (b) Al 3wt.%Mg evenly distributed, (c) Al 3wt.%Mg with Mg around grain boundaries (Al atoms red, Mg atoms blue).

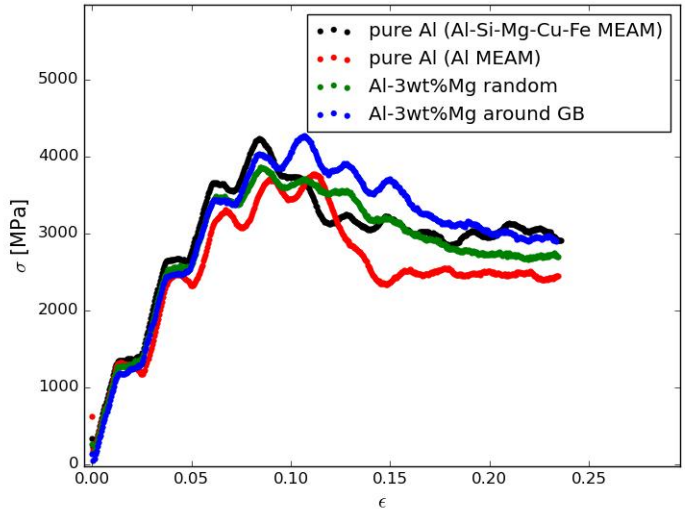

Figure 5.32: Stress-strain curves for MD of tensile deformation of Al-Mg polycrystal with different composition.

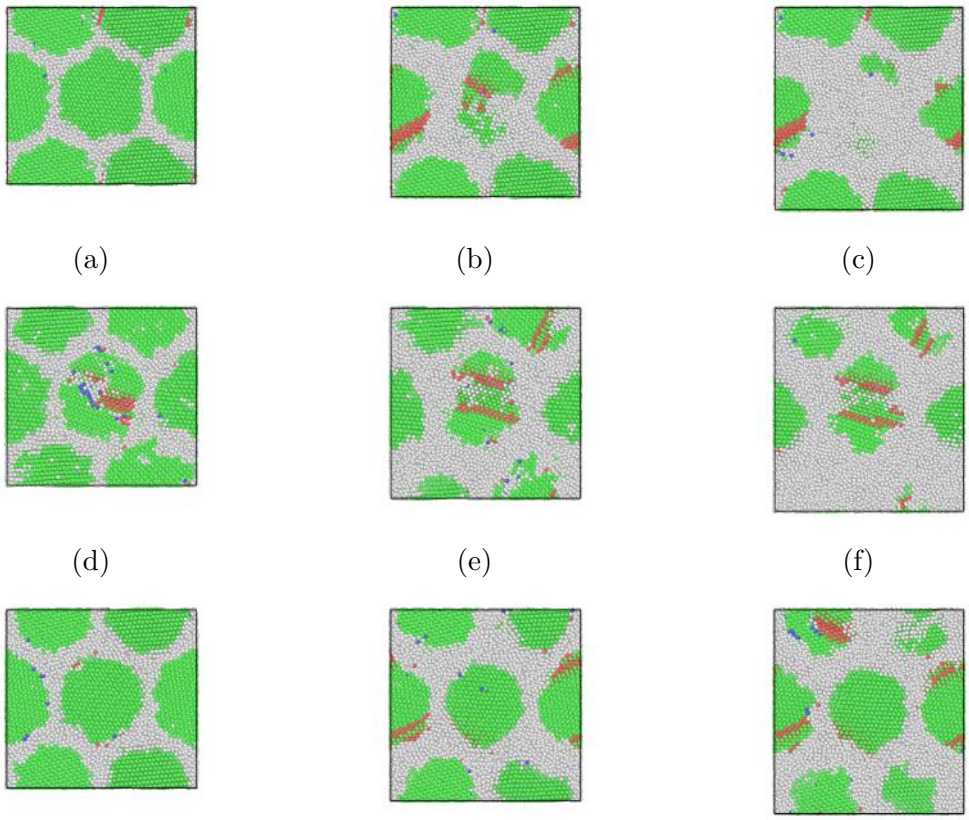

Figure 5.33: Polycrystal FCC block with randomly oriented grains at different strains. a,b,c) pure Al, d,e,f) Al 3wt.%Mg evenly distributed, g,h,i) Al 3wt.%Mg with Mg around grain boundaries, strains: a,d,g) 5.4%, b,e,h) 10.8%, c,f,i) 16.2%.

6. Discussion

6.1 Experimental results

The analysis of experimental data received during in situ tensile testing of 50 nm and 150 nm thin Al3wt.%Mg films clearly confirms that a decreasing thickness of polycrystalline Al-based films results in a decrease of the yield strength. This finding coupled with direct TEM observations of the microstructure during the test could provide additional information clarifying several issues concerning deformation mechanisms and rapture in metallic structures with confined length scales. Although the intrinsic (grain size ≈100 nm) and extrinsic (film thickness) dimensions do not represent a truly extreme nanoscale features, yielding of the films exhibit significant differences in comparison with the behavior of standard bulk materials.

The observed yield strength values (100 – 700 MPa) are in a good agreement with the ones reported for Al thin films in the recent literature. Values between 200 - 400 MPa were reported for 60 - 480 nm thick film [25] where a method of a deformation of substrates was used to deform the films. Bulge testing of free standing pure aluminum films (0.5 – 4.4 µm thick) or films prepared by DC sputtering from Al-Zn-Mg-Cu alloy yield values between 70 and 125 MPa for pure aluminum and 600 MPa for the alloy [133, 134].

The first conspicuous feature is the lack of any intensive dislocation activity in the grain interiors, which is generally responsible for the formation of dislocation pile-ups in bulk materials and so-called Hall-Petch-type relationship [4, 5]. Nevertheless, scarce dislocations emitted from grain boundaries, traversing the grain and annihilating in the grain boundary on the opposite site of the grain, confirm that the dislocation activity does not entirely cease in our thin films, but common dislocation mechanisms do not play a controlling role in the deformation of nanograins. It is necessary to note now, that the yield stress values reported for pure Al film by Cieslar et al. [133] were clearly associated with conventional dislocation mechanisms imposed by the size of grains (flat grains 6 to 100 micrometers in diameter) in the studied films exhibiting standard Hall-Petch relation. Therefore the conformity of yield stress values with our results is rather coincidental and further supports the governing role of grain boundaries in the yielding of our Al-Mg films.

Recent analyses [67, 111] report 15 – 70 nm grain size as limiting dimensions for the dislocation activity suppression in Al nanostrucutres and appearance of new yield controlling processes associated with grain boundaries and diffusion creep. The values of grain size are well below the grain size observed in our study. Nevertheless, grain rotations confirmed by TEM analyses (fig. 4.14, 4.16) support the statements of McFaden et al. [135], that rotation of grains always associated with grain boundary sliding indeed occurs. On the other hand, grain elongation in the tensile direction and their transversal contraction after straining without any significant dislocation activity (fig. 4.9) supports the statements of Shu et al. [136] about the presence of Nabarro-Herring creep in Al nanocrystalline materials, which could occur even at room temperature thanks to a high imposed stress.

The almost pure intergranular fraction of films (fig. 4.13) may indicate the presence of grain boundary dislocation activity and unaccommodated grain boundary sliding and nucleation of voids at boundaries as proposed by Kumar et al. [10]. Nevertheless, a negative role of impurity (or oxides) segregation on grain boundaries and incomplete densification and a presence of pre-existing flaws also could not be neglected in the material prepared by physical vapor deposition [137]. Therefore further careful analysis of the grain boundary microstructure, composition and fracture surfaces are necessary to plausibly explain the fracture mechanism.

6.2 Simulation results

The main features of performed simulations of tensile deformation of single crystal films such as the observed deformation mechanisms, orientation influence or strain rate effects are generally compliant with results reported by various authors for nanopillar compression of FCC structures. Deformation by both full and partial dislocations bordering the stacking faults and rearranging of atoms in lattice was observed during tension or compression of Al [99], Cu [14] and Ni [97] pillars.
The yield strength of single crystals ranges between 6 and 8 GPa according to the orientation and used potential, which is about twice higher than the strength of compressed Al nanopillars [99], which is probably a combination of effect of different interatomic potential and generally higher stress values for the tension over compression experiments and the lower area of surfaces in films compared to pillars, which means less opportunities for dislocation annihilation and associated size effects.
Our orientation studies confirmed activation of different slip systems. Similar result was reported for orientation studies of deformed Al nanopillars by Xu et al. [99], which revealed prevalence of partial dislocations in [001] direction and, on the contrary, crucial role of full dislocations in less symmetrical directions [111], [112] and $[\bar{2}\bar{6}5]$. Quite different result is observed in our study, because a [110] tension direction shows preference in partial dislocations, while in the other directions ([111], [112], [001]) a combination of partial and full dislocations contributes to the deformation. Depending on the orientation, {111} stacking faults of different extent and directions were formed. The directions of activated {111} were analyzed (fig. 6.1) in more detail with regards to the values of the Schmid Factor.
The lowest strength for all materials was observed at deformation in [110] direction parallel to the tensile axis (fig. 6.1a). Large crossing areas of HCP planes in the planes parallel to the z direction were observed. When the tensile direction is denoted as [110], the formed HCP atoms lie in planes (111) and $(11\bar{1})$. The results with [111] parallel to the deformation axis are shown in fig. 6.1b. HCP planes parallel to the z direction were formed, in this case less extensive and not spread through the whole volume of the deformation box. Apart from that, small HCP planes in two directions non parallel to z also form. Their orientation corresponds to $(\bar{1}11)$, $(1\bar{1}1)$, $(11\bar{1})$ planes. Again, relatively extensive SF in two different directions were formed during the deformation in [112] direction parallel to the loading axis (fig. 6.1c). Since none of the planes is perpendicular to the z direction, they are $(\bar{1}11)$ and $(1\bar{1}1)$ planes. Finally, four different directions of SF

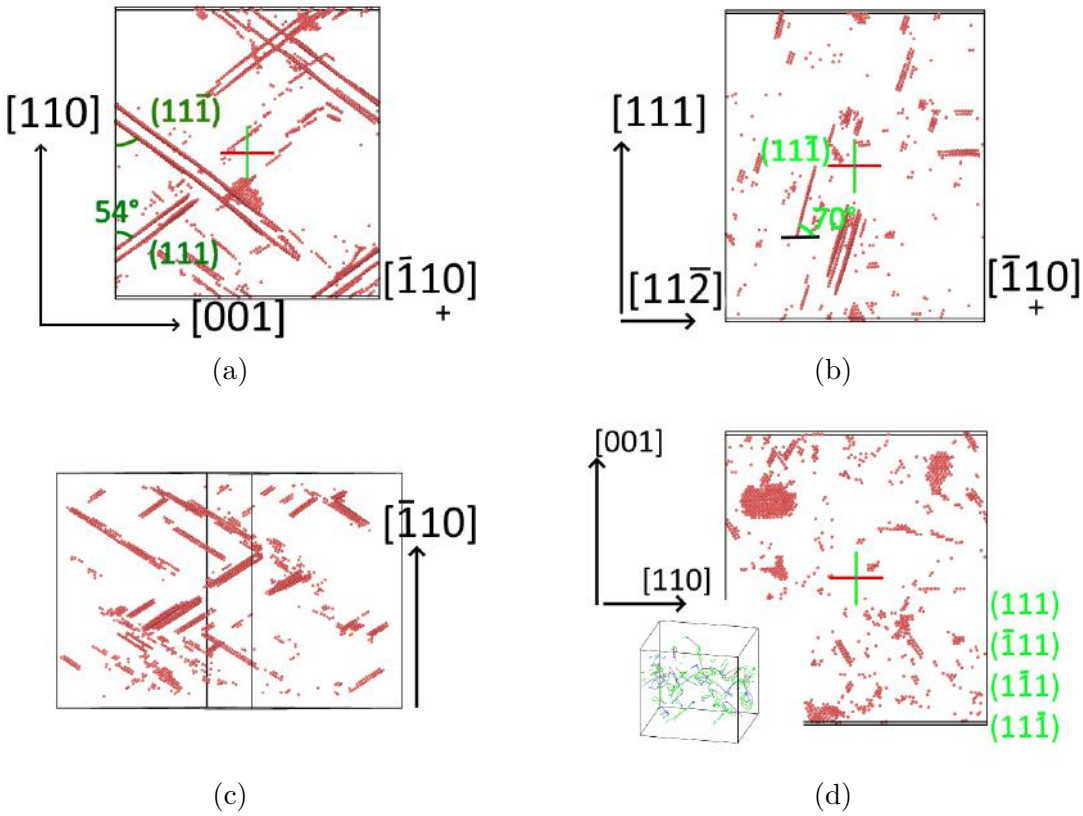

Figure 6.1: Visualisation of planes of h.c.p. atoms formed during tensile deformation of a single crystal at different orientations. Directions parallel to the axis of deformation: a) [110], b) [111], c) [112], d) [001].

are observed during the deformation parallel to [001] direction (fig. 6.1d). The areas of SF planes are smaller than in all previous directions, as well as the length of partial dislocations. The largest part of deformation was carried through ordinary <110> dislocations. Table 6.1 shows computed values of the Schmid factor for perfect <110> dislocations in {111} planes. By comparing the values for individual directions with slip systems activated for individual directions, it follows that all the systems with the highest values of Schmid factor were activated. The prevalence of either partial or full dislocations seems to be linked to the orientation of the activated systems and the free surface. In systems perpendicular to the surface, large areas of SF forms and partial dislocations generated at the free surface quickly propagate to the opposite side. On the contrary, in systems inclined by a large angle from the surface, most of the deformation is carried by full dislocations, with only small fractions of SF bordered by Shockley partials confirming the role of free surfaces as a factor influencing the mechanisms of deformation.

The formation of SF in aluminum is quite common and frequently reported in MD simulations of nano-scale volumes in spite of a high value of stacking fault energy, which prevents SF formation in bulk materials. A question regarding a credibility of MD result arises, however no SF was reported in MD simulations of bulk Al, using periodic boundary conditions in all dimensions. Moreover, some experimental studies of tensile deformation of nanocrystalline Al films report a

110	(111)	($\bar{1}$11)	(1 $\bar{1}$1)	(11$\bar{1}$)	111	(111)	($\bar{1}$11)	(1 $\bar{1}$1)	(11$\bar{1}$)
[110]	-	0	0	-	[110]	-	0.27	0.27	-
[1$\bar{1}$0]	0	-	-	0	[1$\bar{1}$0]	0	-	-	0
[101]	-	0	-	0.41	[101]	-	0.27	-	0.27
[10$\bar{1}$]	0.41	-	0	-	[10$\bar{1}$]	0	-	0	-
[011]	-	-	0	0.41	[011]	-	-	0.27	0.27
[01$\bar{1}$]	0.41	0	-	-	[01$\bar{1}$]	0	0	-	-
100	(111)	($\bar{1}$11)	(1 $\bar{1}$1)	(11$\bar{1}$)	112	(111)	($\bar{1}$11)	(1 $\bar{1}$1)	(11$\bar{1}$)
[110]	-	0.41	0.41	-	[110]	-	0.27	0.27	-
[1$\bar{1}$0]	0.41	-	-	0.41	[1$\bar{1}$0]	0	-	-	0
[101]	-	0.41	-	0.41	[101]	-	0.41	-	0
[10$\bar{1}$]	0.41	-	0.41	-	[10$\bar{1}$]	0.27	-	0.14	-
[011]	-	-	0	0	[011]	-	-	0.41	0
[01$\bar{1}$]	0	0	-	-	[01$\bar{1}$]	0.27	0.14	-	-

Table 6.1: Schmid factor values for {111} slip planes, [110] slip directions and [110], [111], [100], [112] directions of tensile axis.

formation of deformation microtwins congruent with the results of MD [71].
The strain rate studies revealed an increase of yield strength with the increasing strain rate. The result is compliant with the study of yield strength of copper single crystals under different orientations [14] when strain rates between 10^8 and 10^{11} s^{-1} were used. A formation of amorphous regions instead of dislocation activity was also reported for these nanopillars above certain strain rate limit.
The effects of grain boundaries on the deformation mechanisms, namely their role as dislocation sources and sinks and therefore their contribution to the size effects inside the grains were also well documented by various authors for grains with diameters between 6 and 50 nm [102, 105, 113]. Propagation of only leading partial dislocation nucleated at GB without trailing partial which occurred for orientation [110] (fig. 5.15a, 5.15d) agrees with observations of Swygenhoven et al. [107, 110] in 2D grains. The presence of full dislocations in our structure originates from the activation of more slip systems and therefore different accomodation mechanisms in comparison with 2D grains. Better aignment can be found with simulations of 2D columnar films by Yamakov et al. [132] with [110] orientation in z direction predicting a formation of microtwins by continuous propagation of partial dislocations. Even though their films were only under 2 nm, the mechanisms remained congruent with our observations.

6.3 Comparison of experimental and simulation results

Although the conditions of the experiment and the simulation were not identical, some of the basic features of both approaches turned out to be comparable. Firstly, a lack of dislocation activity observed during TEM in situ tensile straining of the both 50 nm and 150 nm thin films corresponds to the limited dislocations motion in the simulation of deformation of polycrystalline films, where only a

few isolated dislocation lines stretched from one free surface to the opposite one crossed the grains before the beginning of the sample fracture. Even though annealing twins were present in the experimental sample, no vast twin formation and twin boundary motion were observed during the deformation. A majority annealing twins remained unmodified in size within the resolution limits of TEM. For this reason, the motion of Shockley partial dislocations connected with the motion of twin boundaries does not represent a substantial contribution to the deformation of thin films. Experimentally observed grain rotations are in direct correlation with MD simulations of the deformation of the polycrystalline sample. Even a very close inspection of simulated lattices exhibits no signs of grains rotation (fig. 6.2). Instead, the main deformation mechanism following from MD simulations is the motion of dislocations. However this dislocation motion in grain boundaries could not be excluded by the TEM experiment.

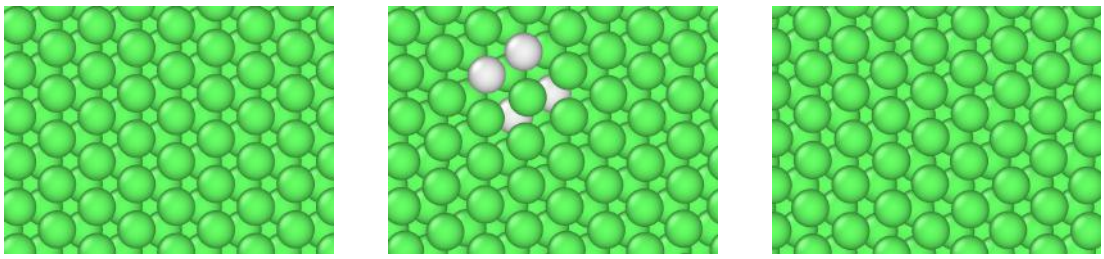

(a) (b) (c)

Figure 6.2: Detail of atomic structures during MD simulation of deformed polycrystal: a) 0%, b) 9%, c) 18% strain.

The largest difference between the TEM experiment and MD simulations was found in absolute values of the material strength. While the experimental studies yielded strength of 100 MPa for the 50 nm thick and 700 MPa for the 150 nm thick films, the strength obtained from MD calculations was by an order of magnitude higher (4 - 5 GPa) with only a small effect of the film thickness and grain size. This discrepancy has its origin most probably in size restrictions pf MD simulations limiting the grain size to $\approx$ 20 nm. Another, probably more important reason for the presence of very high strength values in MD is linked to the excessively high strain rates of MD simulations, where a decrease of strength was observed for strain rates in the range 10^7 - 10^{10} s^{-1} (fig. 5.20).

6.4 Oscillations of stress-strain functions

Periodic oscillations of stress were observed in all simulated stress-strain curves. The amplitude of these oscillations depends on the thickness of the sample. However, no structural changes reflecting this effect were found in simulated structures. Closer inspection of results shows, that oscillations are indeed very regular and that their period is the same as the period of the system temperature oscillations (amplitude $\approx$ 5 K) (fig. 6.3) and oscillations of the sample thickness (due to the limited numbers of atoms in the box).
Therefore, it can be concluded that oscillations appear as a consequence of temperature and volume oscillations caused by implementing Nose-Hover thermostat for the regulation of the simulation temperature. These oscillations could be

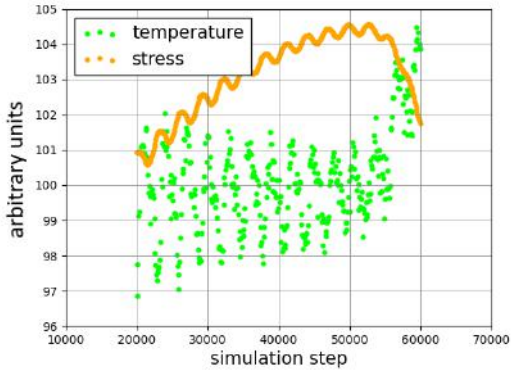

Figure 6.3: Oscillations of the system temperature and stress in 10 nm thick sample.

partially suppressed by an averaging of results through a larger number of simulation steps. Nevertheless, similar oscillations are generally observed in all MD simulations reported in the literature [138, 139].

Conclusion

Nanocrystalline thin films from Al3wt.%Mg alloy were successfully manufactured by a DC magnetron deposition on a glass substrate covered with a polymer. Dissolution of the polymer in organic solvents was used for their release from the substrate, and 50 and 150 nm thick free-standing films were thus prepared and further characterized by enhanced transmission electron microscopy. A significant texture associated with a preferential (110) orientation of columnar grains observed in as-prepared films resists to a large extent further necessary annealing at 400 °C. This annealing results in a partial release of internal stresses and a significant grain growth from ≈ 30 nm to 100-200 nm.

In situ tensile tests at room temperature were performed in TEM with a push-to-pull MEMS equipped deformation holder at $\approx 10^{-4}$ s^{-1} strain rate. Force-displacement curves were recorded and transformed into stress-strain ones. Direct monitoring of the structure evolution during straining was done using BF and HRTEM modes, and ACOM-TEM. Inverse Hall-Petch-type yielding associated with a lower strength of the material with smaller grains was observed. Grain rotation and diffusion induced creep of particular grains with only a scarce dislocation activity in the grain interiors were identified.

Extensive molecular dynamics simulations of deformation processes in thin Al-based films were carried out and the influence of selected parameters on the microstructure evolution and mechanical behavior during tensile deformation was tested. A remarkable susceptibility of results to subtle variations of interatomic potentials was confirmed due to the indispensable high number of integrating steps. Nevertheless, despite of some quantitative discrepancies a majority of qualitative outcomes was approved independently on the selection of the potential. The deformation of single crystal samples showed a predictable orientation influence on the activation of slip systems and consequential strength of the material. Both, orientation with regards to the deformation axis and free surface of the film showed as influential. An increase of the material strength with strain rate was confirmed along with a destruction of the lattice structure at strain rates above the limit 10^{10} s^{-1}. During the deformation of columnar polycrystals, a motion of dislocations inside grain boundaries was confirmed as the main deformation mechanism. Only a scarce dislocation activity consisting of both full and partial dislocations was detected in the grain interior. All the dislocations nucleated either at grain boundaries or at free surfaces.

Results of molecular dynamics simulations comply with main experimental results including the suppression of dislocation activity in the grain interiors and predominant role of grain boundaries. Nevertheless, some effects predicted by MD and missing in the experiment still exist (deformation microtwins, Shockley partials and stacking faults in aluminum, lack of crystal rotations and Nabarro-Herring creep). Most probably they are induced by constraints of MD simulations that arise from the necessity to use confined volumes and extremely high strain rates that are far from real experimental conditions.

Bibliography

[1] RM Keller, SP Baker, and E Arzt. Quantitative analysis of strengthening mechanisms in thin cu films: Effects of film thickness, grain size, and passivation. *Journal of Materials Research*, 13(5):1307–1317, 1998.

[2] Warren Carl Oliver and George Mathews Pharr. An improved technique for determining hardness and elastic modulus using load and displacement sensing indentation experiments. *Journal of Materials Research*, 7(6):1564–1583, 1992.

[3] Junying Min, Thomas B Stoughton, John E Carsley, Blair E Carlson, Jianping Lin, and Xueli Gao. Accurate characterization of biaxial stress-strain response of sheet metal from bulge testing. *International Journal of Plasticity*, 94:192–213, 2017.

[4] EO Hall. The deformation and ageing of mild steel: Iii discussion of results. *Proceedings of the Physical Society. Section B*, 64(9):747, 1951.

[5] NJ Petch. The cleavage strength of polycrystals. *Journal of the Iron and Steel Institute*, 174:25–28, 1953.

[6] J R Weertman and PG Sanders. Plastic deformation of nanocrystalline metals. In *Solid State Phenomena*, volume 35, pages 249–262. Trans Tech Publ, 1993.

[7] Simon C Pun, Wenbo Wang, Amirhossein Khalajhedayati, Jennifer D Schuler, Jason R Trelewicz, and Timothy J Rupert. Nanocrystalline al-mg with extreme strength due to grain boundary doping. *Materials Science and Engineering: A*, 696:400–406, 2017.

[8] Andrew M Minor, SA Syed Asif, Zhiwei Shan, Eric A Stach, Edward Cyrankowski, Thomas J Wyrobek, and Oden L Warren. A new view of the onset of plasticity during the nanoindentation of aluminium. *Nature Materials*, 5(9):697–702, 2006.

[9] M Jin, AM Minor, D Ge, and JW Morris. Study of deformation behavior of ultrafine-grained materials through in situ nanoindentation in a transmission electron microscope. *Journal of materials research*, 20(7):1735–1740, 2005.

[10] KS Kumar, Subra Suresh, Matthew F Chisholm, JA Horton, and P1 Wang. Deformation of electrodeposited nanocrystalline nickel. *Acta Materialia*, 51(2):387–405, 2003.

[11] Martin T Dove. An introduction to atomistic simulation methods. *Seminarios de la SEM*, 4:7–37, 2008.

[12] James M Haile, Ian Johnston, A John Mallinckrodt, and Susan McKay. Molecular dynamics simulation: elementary methods. *Computers in Physics*, 7(6):625–625, 1993.

[13] Jiankuai Diao, Ken Gall, Martin L Dunn, and Jonathan A Zimmerman. Atomistic simulations of the yielding of gold nanowires. *Acta Materialia*, 54(3):643–653, 2006.

[14] Virginie Dupont and Timothy C Germann. Strain rate and orientation dependencies of the strength of single crystalline copper under compression. *Physical Review B*, 86(13):134111, 2012.

[15] Daniel S Gianola, Diana Farkas, Martin Gamarra, and Mo-rigen He. The role of confinement on stress-driven grain boundary motion in nanocrystalline aluminum thin films. *Journal of Applied Physics*, 112(12):124313, 2012.

[16] ZT Trautt and Y Mishin. Grain boundary migration and grain rotation studied by molecular dynamics. *Acta Materialia*, 60(5):2407–2424, 2012.

[17] WD Nix. Metallic thin films: stresses and mechanical properties. In *Metallic Films for Electronic, Optical and Magnetic Applications*, pages 353–421. Elsevier, 2014.

[18] King-Ning Tu, James W Mayer, and Leonard Feldman. *Electronic thin film science for electrical engineers and materials scientists*. Macmillan, 1992.

[19] O Kraft. Thin films: mechanical testing. In *Encyclopedia of Materials: Science and Technology. Vol. 10*, pages 9257–9262. Elsevier Science Ltd., 2001.

[20] FR Brotzen. Mechanical testing of thin films. *International Materials Reviews*, 39(1):24–45, 1994.

[21] David T Read and James W Dally. A new method for measuring the strength and ductility of thin films. *Journal of Materials Research*, 8(7):1542–1549, 1993.

[22] Arash Tajik and Hamid Jahed. Standalone tensile testing of thin film materials for mems/nems applications. *Microelectromechanical Systems and Devices*, page 435, 2012.

[23] JA Ruud, D Josell, F Spaepen, and AL Greer. A new method for tensile testing of thin films. *Journal of Materials Research*, 8(1):112–117, 1993.

[24] RD Emery and GL Povirk. Tensile behavior of free-standing gold films. part i. coarse-grained films. *Acta Materialia*, 51(7):2067–2078, 2003.

[25] Young-Seok Kang and Paul S Ho. Thickness dependent mechanical behavior of submicron aluminum films. *Journal of Electronic Materials*, 26(7):805–813, 1997.

[26] James E Steinwall and HH Johnson. Mechanical properties of thin film aluminum fibers: Grain size effects. *MRS Online Proceedings Library Archive*, 188, 1990.

[27] Alfred J Griffin Jr, Franz R Brotzen, and Clyde Dunn. Hall-petch relation in thin film metallizations. *Scripta metallurgica*, 20(9):1271–1272, 1986.

[28] Jaroslav Menčík. Uncertainties and errors in nanoindentation. *Nanoindentation in Materials Science*, 54:53–86, 2012.

[29] MF Doerner, DS Gardner, and WD Nix. Plastic properties of thin films on substrates as measured by submicron indentation hardness and substrate curvature techniques. *Journal of Materials Research*, 1:845–851, 1986.

[30] D Heinen, HG Bohn, and W Schilling. On the mechanical strength of free-standing and substrate-bonded al thin films. *Journal of Applied Physics*, 77:3742–3745, 1995.

[31] Michael D Uchic, Dennis M Dimiduk, Jeffrey N Florando, and William D Nix. Exploring specimen size effects in plastic deformation of ni 3 (al, ta). *MRS Online Proceedings Library*, 753:1–6, 2002.

[32] Michael D Uchic, Dennis M Dimiduk, Jeffrey N Florando, and William D Nix. Sample dimensions influence strength and crystal plasticity. *Science*, 305(5686):986–989, 2004.

[33] Michael D Uchic, Paul A Shade, and Dennis M Dimiduk. Plasticity of micrometer-scale single crystals in compression. *Annual Review of Materials Research*, 39:361–386, 2009.

[34] Oliver Kraft, Patric A Gruber, Reiner Mönig, and Daniel Weygand. Plasticity in confined dimensions. *Annual review of Materials Research*, 40:293–317, 2010.

[35] Julia R Greer and Jeff Th M De Hosson. Plasticity in small-sized metallic systems: Intrinsic versus extrinsic size effect. *Progress in Materials Science*, 56(6):654–724, 2011.

[36] DM Dimiduk, MD Uchic, and TA Parthasarathy. Size-affected single-slip behavior of pure nickel microcrystals. *Acta Materialia*, 53(15):4065–4077, 2005.

[37] ZW Shan, Raja K Mishra, SA Syed Asif, Oden L Warren, and Andrew M Minor. Mechanical annealing and source-limited deformation in submicrometre-diameter ni crystals. *Nature Materials*, 7(2):115–119, 2008.

[38] Julia R Greer and William D Nix. Nanoscale gold pillars strengthened through dislocation starvation. *Physical Review B*, 73(24):245410, 2006.

[39] KS Ng and AHW Ngan. Stochastic nature of plasticity of aluminum micropillars. *Acta Materialia*, 56(8):1712–1720, 2008.

[40] Oliver Kraft and CA Volkert. Size effects on deformation and fatigue of thin films and small structures. *CAMTEC, Cambridge University*, 2006.

[41] CP Frick, BG Clark, S Orso, AS Schneider, and E Arzt. Size effect on strength and strain hardening of small-scale [1 1 1] nickel compression pillars. *Materials Science and Engineering: A*, 489(1-2):319–329, 2008.

[42] Sharif Shahbeyk, George Z Voyiadjis, Vahid Habibi, Sarah Hashemi Astaneh, and Mohammadreza Yaghoobi. Review of size effects during micropillar compression test: Experiments and atomistic simulations. *Crystals*, 9(11):591, 2019.

[43] Triplicane A Parthasarathy, Satish I Rao, Dennis M Dimiduk, Michael D Uchic, and Dallas R Trinkle. Contribution to size effect of yield strength from the stochastics of dislocation source lengths in finite samples. *Scripta Materialia*, 56(4):313–316, 2007.

[44] Satish I Rao, DM Dimiduk, Triplicane A Parthasarathy, MD Uchic, Meijie Tang, and Chris Woodward. Athermal mechanisms of size-dependent crystal flow gleaned from three-dimensional discrete dislocation simulations. *Acta Materialia*, 56(13):3245–3259, 2008.

[45] Julia R Greer, Warren C Oliver, and William D Nix. Size dependence of mechanical properties of gold at the micron scale in the absence of strain gradients. *Acta Materialia*, 53(6):1821–1830, 2005.

[46] DM Norfleet, DM Dimiduk, SJ Polasik, MD Uchic, and MJ Mills. Dislocation structures and their relationship to strength in deformed nickel microcrystals. *Acta Materialia*, 56(13):2988–3001, 2008.

[47] Marc A Meyers, A Mishra, and David J Benson. Mechanical properties of nanocrystalline materials. *Progress in Materials Science*, 51(4):427–556, 2006.

[48] TG Nieh and J Wadsworth. Hall-petch relation in nanocrystalline solids. *Scripta Metallurgica et Materialia*, 25(4):955–958, 1991.

[49] GW Nieman, JR Weertman, and RW Siegel. Mechanical behavior of nanocrystalline cu and pd. *Journal of Materials Research*, 6(5):1012–1027, 1991.

[50] CA Schuh, TG Nieh, and T Yamasaki. Hall-petch breakdown manifested in abrasive wear resistance of nanocrystalline nickel. *Scripta Materialia*, 46(10):735–740, 2002.

[51] Ning Wang, Zhirui Wang, KT Aust, and U Erb. Room temperature creep behavior of nanocrystalline nickel produced by an electrodeposition technique. *Materials Science and Engineering: A*, 237(2):150–158, 1997.

[52] RO Scattergood and CC Koch. A modified model for hall-petch behavior in nanocrystalline materials. *Scripta metallurgica et materialia*, 27(9):1195–1200, 1992.

[53] J Lian, B Baudelet, and AA Nazarov. Model for the prediction of the mechanical behaviour of nanocrystalline materials. *Materials Science and Engineering: A*, 172(1-2):23–29, 1993.

[54] RA Masumura, PM Hazzledine, and CS Pande. Yield stress of fine grained materials. *Acta Materialia*, 46(13):4527–4534, 1998.

[55] Hans Conrad and Jagdish Narayan. On the grain size softening in nanocrystalline materials. *Scripta materialia*, 42(11):1025–1030, 2000.

[56] S Takeuchi. The mechanism of the inverse hall-petch relation of nanocrystals. *Scripta materialia*, 44(8-9):1483–1487, 2001.

[57] V Yamakov, D Wolf, SR Phillpot, AK Mukherjee, and H Gleiter. Deformation-mechanism map for nanocrystalline metals by molecular-dynamics simulation. *Nature materials*, 3(1):43–47, 2004.

[58] HW Song, SR Guo, and ZQ Hu. A coherent polycrystal model for the inverse hall-petch relation in nanocrystalline materials. *Nanostructured Materials*, 11(2):203–210, 1999.

[59] DA Konstantinidis and EC Aifantis. On the "anomalous" hardness of nanocrystalline materials. *Nanostructured materials*, 10(7):1111–1118, 1998.

[60] CE Carlton and PJ Ferreira. What is behind the inverse hall-petch effect in nanocrystalline materials? *Acta Materialia*, 55(11):3749–3756, 2007.

[61] Terence G Langdon. The mechanical properties of superplastic materials. *Metallurgical Transactions A*, 13(5):689–701, 1982.

[62] ET Lilleodden, JA Zimmerman, SM Foiles, and WD Nix. Atomistic simulations of elastic deformation and dislocation nucleation during nanoindentation. *Journal of the Mechanics and Physics of Solids*, 51(5):901–920, 2003.

[63] Eric A Stach, Tony Freeman, Andrew M Minor, Doug K Owen, John Cumings, Mark A Wall, Tomas Chraska, Robert Hull, JW Morris Jr, A Zettl, et al. Development of a nanoindenter for in-situ transmission electron microscopy. *Microscopy and Microanalysis*, 7(LBNL-47402), 2001.

[64] Hussein Nili, Kourosh Kalantar-zadeh, Madhu Bhaskaran, and Sharath Sriram. In situ nanoindentation: Probing nanoscale multifunctionality. *Progress in Materials Science*, 58(1):1–29, 2013.

[65] AM Minor, ET Lilleodden, EA Stach, and JW Morris. Direct observations of incipient plasticity during nanoindentation of al. *Journal of Materials research*, 19(1):176–182, 2004.

[66] M Winning, G Gottstein, and LS Shvindlerman. Migration of grain boundaries under the influence of an external shear stress. *Materials Science and Engineering: A*, 317(1-2):17–20, 2001.

[67] M Jin, AM Minor, EA Stach, and JW Morris Jr. Direct observation of deformation-induced grain growth during the nanoindentation of ultrafine-grained al at room temperature. *Acta Materialia*, 52(18):5381–5387, 2004.

[68] WA Soer, J Th M De Hosson, AM Minor, JW Morris Jr, and EA Stach. Effects of solute mg on grain boundary and dislocation dynamics during nanoindentation of al-mg thin films. *Acta materialia*, 52(20):5783–5790, 2004.

[69] RC Hugo, H Kung, JR Weertman, R Mitra, JA Knapp, and DM Follstaedt. In-situ tem tensile testing of dc magnetron sputtered and pulsed laser deposited ni thin films. *Acta Materialia*, 51(7):1937–1943, 2003.

[70] Md Amanul Haque and MTA Saif. In situ tensile testing of nanoscale freestanding thin films inside a transmission electron microscope. *Journal of Materials Research*, 20(7):1769–1777, 2005.

[71] K Hattar, J Han, MTA Saif, and Ian M Robertson. In situ transmission electron microscopy observations of toughening mechanisms in ultrafine grained columnar aluminum thin films. *Journal of materials research*, 20(7):1869–1877, 2005.

[72] Frederic Mompiou, Marc Legros, A Boe, Michael Coulombier, J-P Raskin, and Thomas Pardoen. Inter-and intragranular plasticity mechanisms in ultrafine-grained al thin films: An in situ tem study. *Acta materialia*, 61(1):205–216, 2013.

[73] F Mompiou, D Caillard, and M Legros. Grain boundary shear-migration coupling—i. in situ tem straining experiments in al polycrystals. *Acta Materialia*, 57(7):2198–2209, 2009.

[74] Hosni Idrissi, Aaron Kobler, Behnam Amin-Ahmadi, Michael Coulombier, Montserrat Galceran, Jean-Pierre Raskin, Stéphane Godet, Christian Kübel, Thomas Pardoen, and Dominique Schryvers. Plasticity mechanisms in ultrafine grained freestanding aluminum thin films revealed by in-situ transmission electron microscopy nanomechanical testing. *Applied Physics Letters*, 104(10):101903, 2014.

[75] A Kobler, A Kashiwar, H Hahn, and C Kübel. Combination of in situ straining and acom tem: A novel method for analysis of plastic deformation of nanocrystalline metals. *Ultramicroscopy*, 128:68–81, 2013.

[76] Frédéric Mompiou and Marc Legros. Quantitative grain growth and rotation probed by in-situ tem straining and orientation mapping in small grained al thin films. *Scripta Materialia*, 99:5–8, 2015.

[77] Dennis C Rapaport. *The art of molecular dynamics simulation*. Cambridge university press, 2004.

[78] Berni Julian Alder and Thomas Everett Wainwright. Phase transition for a hard sphere system. *The Journal of Chemical Physics*, 27:1208–1209, 1957.

[79] Yuji Sugita and Yuko Okamoto. Replica-exchange molecular dynamics method for protein folding. *Chemical Physics Letters*, 314(1-2):141–151, 1999.

[80] Abdollah Esmaeili. Applications of nanotechnology in oil and gas industry. In *AIP conference proceedings*, volume 1414, pages 133–136. American Institute of Physics, 2011.

[81] Farid F Abraham. Computational statistical mechanics methodology, applications and supercomputing. *Advances in Physics*, 35(1):1–111, 1986.

[82] Thomas J Lenosky, Babak Sadigh, Eduardo Alonso, Vasily V Bulatov, Tomas Diaz de la Rubia, Jeongnim Kim, Arthur F Voter, and Joel D Kress. Highly optimized empirical potential model of silicon. *Modelling and Simulation in Materials Science and Engineering*, 8(6):825, 2000.

[83] Lammps molecular dynamics simulator.

[84] Steve Plimpton. Fast parallel algorithms for short-range molecular dynamics. *Journal of Computational Physics*, 117(1):1–19, 1995.

[85] Adarsh Balasubramanian. *Discovery and Implementation of fast, accurate and transferable Many-body Interatomic Potentials*. PhD thesis, Johns Hopkins University, 2019.

[86] Murray S Daw and Michael I Baskes. Semiempirical, quantum mechanical calculation of hydrogen embrittlement in metals. *Physical Review Letters*, 50(17):1285, 1983.

[87] Murray S Daw and Michael I Baskes. Embedded-atom method: Derivation and application to impurities, surfaces, and other defects in metals. *Physical Review B*, 29(12):6443, 1984.

[88] Murray S Daw, Stephen M Foiles, and Michael I Baskes. The embedded-atom method: a review of theory and applications. *Materials Science Reports*, 9(7-8):251–310, 1993.

[89] Murray S Daw and RD Hatcher. Application of the embedded atom method to phonons in transition metals. *Solid State Communications*, 56(8):697–699, 1985.

[90] SM Foiles. Application of the embedded-atom method to liquid transition metals. *Physical Review B*, 32(6):3409, 1985.

[91] SM Foiles. Calculation of the atomic structure of the= 13 (θ= 22.6)[001] twist boundary in gold. *Acta Metallurgica*, 37(10):2815–2821, 1989.

[92] MI Baskes. Application of the embedded-atom method to covalent materials: a semiempirical potential for silicon. *Physical Review Letters*, 59(23):2666, 1987.

[93] Michael I Baskes. Modified embedded-atom potentials for cubic materials and impurities. *Physical Review B*, 46(5):2727, 1992.

[94] Wataru Shinoda, Motoyuki Shiga, and Masuhiro Mikami. Rapid estimation of elastic constants by molecular dynamics simulation under constant stress. *Physical Review B*, 69(13):134103, 2004.

[95] Mark E Tuckerman, José Alejandre, Roberto López-Rendón, Andrea L Jochim, and Glenn J Martyna. A liouville-operator derived measure-preserving integrator for molecular dynamics simulations in the isothermal–isobaric ensemble. *Journal of Physics A: Mathematical and General*, 39(19):5629, 2006.

[96] Frederic Sansoz. Atomistic processes controlling flow stress scaling during compression of nanoscale face-centered-cubic crystals. *Acta Materialia*, 59(9):3364–3372, 2011.

[97] Mohammadreza Yaghoobi and George Z Voyiadjis. Size effects in fcc crystals during the high rate compression test. *Acta Materialia*, 121:190–201, 2016.

[98] George Z Voyiadjis and Mohammadreza Yaghoobi. Size and strain rate effects in metallic samples of confined volumes: Dislocation length distribution. *Scripta Materialia*, 130:182–186, 2017.

[99] S Xu, YF Guo, and AHW Ngan. A molecular dynamics study on the orientation, size, and dislocation confinement effects on the plastic deformation of al nanopillars. *International Journal of Plasticity*, 43:116–127, 2013.

[100] Mohammadreza Yaghoobi and George Z Voyiadjis. Effect of boundary conditions on the md simulation of nanoindentation. *Computational Materials Science*, 95:626–636, 2014.

[101] George Z Voyiadjis and Mohammadreza Yaghoobi. Role of grain boundary on the sources of size effects. *Computational Materials Science*, 117:315–329, 2016.

[102] H Van Swygenhoven, M Spaczer, and A Caro. Microscopic description of plasticity in computer generated metallic nanophase samples: a comparison between cu and ni. *Acta Materialia*, 47(10):3117–3126, 1999.

[103] V Yamakov, D Wolf, SR Phillpot, and H Gleiter. Deformation twinning in nanocrystalline al by molecular-dynamics simulation. *Acta Materialia*, 50(20):5005–5020, 2002.

[104] D Wolf, V Yamakov, SR Phillpot, A Mukherjee, and H Gleiter. Deformation of nanocrystalline materials by molecular-dynamics simulation: relationship to experiments? *Acta Materialia*, 53(1):1–40, 2005.

[105] D Feichtinger, PM Derlet, and H Van Swygenhoven. Atomistic simulations of spherical indentations in nanocrystalline gold. *Physical Review B*, 67(2):024113, 2003.

[106] Adrian P Sutton. Interfaces in crystalline materials. *Monographs on the Physice and Chemistry of Materials*, pages 414–423, 1995.

[107] H Van Swygenhoven, PM Derlet, and A Hasnaoui. Atomic mechanism for dislocation emission from nanosized grain boundaries. *Physical Review B*, 66(2):024101, 2002.

[108] A Hasnaoui, H Van Swygenhoven, and PM Derlet. Cooperative processes during plastic deformation in nanocrystalline fcc metals: A molecular dynamics simulation. *Physical Review B*, 66(18):184112, 2002.

[109] MA Xiling and Yang Wei. Md simulation for nanocrystals. *Acta Mechanica Sinica*, 19(6):485–507, 2003.

[110] H Van Swygenhoven, Diana Farkas, and Alfredo Caro. Grain-boundary structures in polycrystalline metals at the nanoscale. *Physical Review B*, 62(2):831, 2000.

[111] V Yamakov, D Wolf, M Salazar, SR Phillpot, and H Gleiter. Length-scale effects in the nucleation of extended dislocations in nanocrystalline al by molecular-dynamics simulation. *Acta Materialia*, 49(14):2713–2722, 2001.

[112] Jang Hyuk Yoon, Seong Jin Kim, and Ho Jang. Molecular dynamics simulation of stress induced grain boundary migration during nanoindentation experiments. In *Materials Science Forum*, volume 449, pages 89–92. Trans Tech Publ, 2004.

[113] A Hasnaoui, PM Derlet, and H Van Swygenhoven. Interaction between dislocations and grain boundaries under an indenter–a molecular dynamics simulation. *Acta Materialia*, 52(8):2251–2258, 2004.

[114] Yashashree Kulkarni, Robert J Asaro, and Diana Farkas. Are nanotwinned structures in fcc metals optimal for strength, ductility and grain stability? *Scripta Materialia*, 60(7):532–535, 2009.

[115] Ho Jang and Diana Farkas. Interaction of lattice dislocations with a grain boundary during nanoindentation simulation. *Materials Letters*, 61(3):868–871, 2007.

[116] JA Zimmerman, CL Kelchner, PA Klein, JC Hamilton, and SM Foiles. Surface step effects on nanoindentation. *Physical Review Letters*, 87(16):165507, 2001.

[117] Push-to-Pull Device (PTP), howpublished = `https://www.bruker.com/en/products-and-solutions/test-and-measurement/nanomechanical-instruments-for-sem-tem/push-to-pull-device.html`, note = Accessed: 2021-05-29.

[118] astar, howpublished = `https://www.ads-img.co.jp/wp-content/uploads/nanom_astarwebpresentation1.pdf`, note = Accessed: 2021-07-1.

[119] Edgar F. Rauch, Joaquin Portillo, Stavros Nicolopoulos, Daniel Bultreys, Sergei Rouvimov, and Peter Moeck. Automated nanocrystal orientation and phase mapping in the transmission electron microscope on the basis of precession electron diffraction. *Zeitschrift für Kristallographie*, 225(2-3):103–109, 2010.

[120] Hysitron PI 95 TEM PicoIndenter, howpublished = `https://www.bruker.com/en/products-and-solutions/test-and-measurement/nanomechanical-instruments-for-sem-tem/hysitron-pi-95-tem-picoindenter.html`, note = Accessed: 2021-05-30.

[121] LAMMPS Molecular Dynamics Simulator, howpublished = `http://lammps.sandia.gov/`, note = Accessed: 2021-05-15.

[122] Pierre Hirel. Atomsk: A tool for manipulating and converting atomic data files. *Computer Physics Communications*, 197:212–219, 2015.

[123] Alexander Stukowski. Visualization and analysis of atomistic simulation data with OVITO-the Open Visualization Tool. *MODELLING AND SIMULATION IN MATERIALS SCIENCE AND ENGINEERING*, 18(1), JAN 2010.

[124] A-L Barabasi, Harry Eugene Stanley, et al. *Fractal concepts in surface growth*. Cambridge University Press, 1995.

[125] Yasushi Nakajima, Koichi Kusuyama, Hidenobu Yamaguchi, and Yoshinori Murakami. Growth of single-crystal aluminum films on silicon substrates by dc magnetron sputtering. *Japanese Journal of Applied Physics*, 31(6R):1860, 1992.

[126] Bohumir Jelinek, Sebastien Groh, Mark F Horstemeyer, Jeffery Houze, Seong-Gon Kim, Gregory J Wagner, Amitava Moitra, and Michael I Baskes. Modified embedded atom method potential for al, si, mg, cu, and fe alloys. *Physical Review B*, 85(24):245102, 2012.

[127] Y M Kim et al. Atomistic modeling of pure mg and mg-al systems. *Calphad*, 33:650–657, 2009.

[128] MI Pascuet and Julian Roberto Fernández. Atomic interaction of the meam type for the study of intermetallics in the al-u alloy. *Journal of Nuclear Materials*, 467:229–239, 2015.

[129] List of interatomic potential entries, howpublished = `https://www.ctcms.nist.gov/potentials/entry/`, note = Accessed: 2021-06-29.

[130] Richard W Hertzberg, Richard P Vinci, and Jason L Hertzberg. *Deformation and fracture mechanics of engineering materials*. John Wiley & Sons, 2020.

[131] Lawrence Eugene Murr. Interfacial phenomena in metals and alloys. 1975.

[132] V Yamakov et al. Dislocation processes in the deformation of nanocrystalline aluminium by molecular-dynamics simulation. *Nature Materials*, 1:45–49, 2002.

[133] M Cieslar et al. Plasticity of thin al films as a function of temperature. *Materials Science and Engineering: A*, 387:734–737, 2004.

[134] M Cieslar et al. The influence of temperature on plastic deformation of free standing thin al-zn-mg-cu films. *Journal of Alloys and Compounds*, 378(1-2):312–315, 2004.

[135] S X McFadden et al. Superplasticity in nanocrystalline ni3al and ti alloys. *MRS Online Proceedings Library (OPL)*, 634, 2000.

[136] X Shu et al. Size effect on the deformation mechanisms of nanocrystalline platinum thin films. *Scientific Reports*, 7:1–11, 2017.

[137] H Van Swygenhoven F T Dalla and M Victoria. Nanocrystalline electrodeposited ni: microstructure and tensile properties. *Acta Materialia*, 50:3957–3970, 2002.

[138] Xu Zhang, Shuyan Liu, Han Liu, Jinwen Zhang, and Xiaoning Yang. Molecular dynamics simulation of the mechanical properties of multilayer graphene oxide nanosheets. *RSC Advances*, 7:55005–55011, 2017.

[139] Yudi Rosandi, Hoang-Thien Luu, Herbert M Urbassek, and Nina Gunkelmann. Molecular dynamics simulations of the mechanical behavior of alumina coated aluminum nanowires under tension and compression. *RSC Advances*, 10:14353–14359, 2020.

List of Figures

List of Tables

Nomenclature

ACOM-TEM	Automated crystallographic orientation mapping in transmission electron microscope
ASTAR	Automated crystal orientation mapping
BCC	Body centered cubic
BF	Bright field
DF	Dark field
EAM	Embedded atom method
FCC	Face centered cubic
FIB	Focused ion beam
GB	Grain boundary
HCP	Hexagonal close packed
HRTEM	Hight resolution electron microscopy
LAMMPS	Large-scale Atomic/Molecular Massively Parallel Simulator
MD	Molecular dynamics
MEAM	Modified embedded atom method
MEMS	Micro-electro-mechanical systems
OVITO	Open visualization tool
PTP	Push-to-pull
SEM	Scanning electron microscopy
SF	Stacking fault
STEM	Scanning transmission electron microscopy
TEM	Transmission electron microscopy